Cosmologically Varying Kinetic Mixing

Xucheng Gan[1, *] and Di Liu[2, 3, †]

[1]*Center for Cosmology and Particle Physics, Department of Physics,*
New York University, New York, NY 10003, USA
[2]*Deutsches Elektronen-Synchrotron DESY, Notkestr. 85, 22607 Hamburg, Germany*
[3]*Laboratoire d'Annecy-le-Vieux de Physique Théorique,*
CNRS – USMB, BP 110 Annecy-le-Vieux, F-74941 Annecy, France

The portal connecting the invisible and visible sectors is one of the most natural explanations of the dark world. However, the early-time dark matter production via the portal faces extremely stringent late-time constraints. To solve such tension, we construct the scalar-controlled kinetic mixing varying with the ultralight CP-even scalar's cosmological evolution. To realize this and eliminate the constant mixing, we couple the ultralight scalar within the mass range $10^{-33}\text{eV} \lesssim m_0 \ll \text{eV}$ with the heavy doubly charged messengers and impose the $\mathbb{Z}_2$ symmetry under the dark charge conjugation. Via the varying mixing, the $\text{keV} - \text{MeV}$ dark photon dark matter is produced through the early-time freeze-in when the scalar is misaligned from the origin and free from the late-time exclusions when the scalar does the damped oscillation and dynamically sets the kinetic mixing. We also find that the scalar-photon coupling emerges from the underlying physics, which changes the cosmological history and provides the experimental targets based on the fine-structure constant variation and the equivalence principle violation. To protect the scalar naturalness, we discretely re-establish the broken shift symmetry by embedding the minimal model into the $\mathbb{Z}_N$-protected model. When $N \sim 10$, the scalar's mass quantum correction can be suppressed much below 10^{-33}eV. Moreover, utilizing two different methods, we precisely calculate the $\mathbb{Z}_N$-invariant Coleman-Weinberg potential to arbitrary orders. Finally, we explore the varying kinetic mixing in the Dirac gaugino model and the dark matter models via other varying portals.

CONTENTS

* xg767@nyu.edu
† di.liu@lapth.cnrs.fr

I. INTRODUCTION

We know that dark matter exists, but we do not know the dark matter's particle nature. Even so, we can naturally imagine that the dark matter stays in the invisible sector, and the invisible and visible sectors are connected by the portal. Through the portal, the energy flow from the visible sector to the invisible sector, which is known as freeze-in [1], or vice versa, which is known as freeze-out. Hence, the dark matter reaches $\Omega_{\rm DM}h^2 \simeq 0.12$, being compatible with the CMB anisotropy [2, 3]. The kinetic mixing [2], one of the three major portals [2, 4–13], connects the photon and the dark photon as $\mathcal{L} \supset \epsilon F_{\mu\nu} F'^{\mu\nu}/2$. In the last few decades, the research on the time-independent kinetic mixing has boosted on both the experimental and theoretical sides [14–26], with only a few discussions on the spacetime-varying scenarios [27–30]. In the meantime, other varying constants are extensively discussed [31–57]. Moreover, extremely strong tensions exist between the early-time dark matter production through the portal and the late-time constraints on the portal, such as the freeze-in of the dark matter as the dark photon [58–60] or the sterile neutrino [61, 62], and the freeze-out of the dark matter as the dark Higgs [63]. To solve such tension in the simplest way, we allow the portal evolves during the universe's expansion. However, there is no free lunch to evade the constraints without consequences. To be more specific, controlling the portal leaves significant imprints in our universe, which changes the early cosmological history and can be detected by experiments designed for general relativity testing and ultralight dark matter detection.

In this work, we study the scalar-controlled kinetic mixing by meticulously exploring the top-down and bottom-up theories, cosmological history, $\mathrm{keV} - \mathrm{MeV}$ dark photon dark matter production, and experimental signals from both the dark photon dark matter and the nonrelativistic ultralight scalar relic. To vary the kinetic mixing, we couple the ultralight scalar ϕ, the CP-even degree of freedom predicted by the string theory [64–70], to the heavy fermionic messengers doubly charged under the standard model $U(1)$ and dark $U(1)$. Here, the constant kinetic mixing is eliminated when the $\mathbb{Z}_2$ symmetry under the dark charge conjugation is imposed. Given this, in the low energy limit, the varying-mixing operator $\phi F F'$ emerges, along with the scalar-photon coupling, such as ϕF^2 or $\phi^2 F^2$ [1]. Initially, ϕ has the early misalignment opening the portal for the dark photon dark matter production with the kinetic mixing $\epsilon_{\rm FI} \sim 10^{-12}$, which stems from the early-time $\mathbb{Z}_2$-breaking of the system. Afterward, ϕ's damped oscillation gradually and partially closes the portal, which stems from the late-time $\mathbb{Z}_2$-restoration. Through the evolution during the cosmological expansion, ϕ sets the benchmark kinetic mixing of the dark photon dark matter, which is free from stringent late-time constraints, such as stellar energy loss [71–74], direct detection [60, 75–80], and late-time decay bounds [58, 59, 81, 82]. At the same time, via the scalar-photon coupling, the ultralight scalar as the nonrelativistic

---

[1] When $\phi \sim f$, ϕ is replaced by $f\sin(\phi/f)$ according to the discussions in Sec. II. However, since the perturbative form is already enough for the late-time experiments where $\phi \ll f$, we use it in the whole text to simplify the notation.
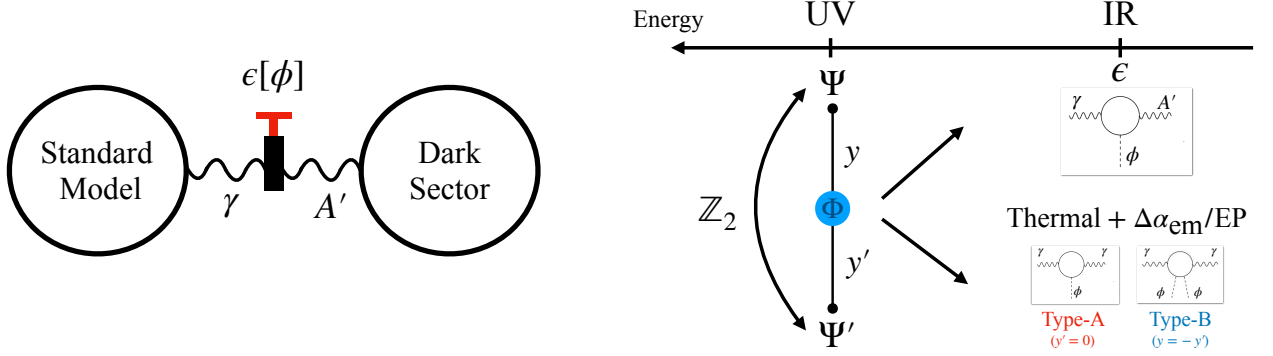
Figure 1. **Left**: The schematic diagram of the cosmologically varying kinetic mixing. The dark and standard model sectors are connected through the kinetic mixing controlled by the CP-even scalar ϕ, the subcomponent of the dark matter in the late universe. Based on this model, the energy flows from the dark sector to the standard model sector in the early universe for the dark matter production with the portal opened. In the late universe, with the portal partially closed, the dark matter is safe from stringent constraints. **Right**: The cosmologically varying kinetic mixing in the UV and IR theories. In the UV theory, there are heavy messengers Ψ and Ψ', both charged under $U(1)_Y$ and $U(1)_d$. Here, Ψ and Ψ' carry the same electromagnetic charge but the opposite dark charge. To generate the varying kinetic mixing, Ψ and Ψ' are coupled with the scalar Φ via the Yukawa interactions y and y'. To eliminate the constant kinetic mixing, the mass degeneracy between Ψ and Ψ' is imposed, which is protected by the $\mathbb{Z}_2$ symmetry. In the IR theory, the nondynamical heavy messengers are integrated out, which induces the varying kinetic mixing ($\phi F F'$) and the scalar-photon coupling (ϕF^2 or $\phi^2 F^2$). In the nonperturbative region, ϕ should be replaced by $f \sin(\phi/f)$ according to Eq. (7) and Eq. (13) because it is the angular part of Φ. Based on whether the $\mathbb{Z}_2$ symmetry is slightly broken by the Yukawas or not, we classify the theory into two types with totally different phenomenologies: The type-A model with the linear scalar-photon coupling ($y \neq 0, y' = 0$) and the type-B model with the quadratic scalar-photon coupling ($y' = -y$). These scalar-photon interactions lead to nontrivial cosmological history caused by the thermal effect and the signals from the $\alpha_{\rm em}$ variation and the equivalence principle violation.

relic in the mass range 10^{-33}eV $\lesssim m_0 \ll$ eV changes the fine-structure constant, and the scalar as the mediator contributes to the extra forces between two objects. Based on these facts, the experiments such as the equivalence principle (EP) violation test [83–85], clock comparison [86–90], resonant-mass detector [91], PTA [92], CMB [93, 94], and BBN [93, 95, 96] can be used to test the scalar-controlled kinetic mixing, and the experimental targets are set by the dark photon freeze-in. In the meantime, the experimental targets for keV − MeV dark photon dark matter detections are set by the ultralight scalar mass. If the signals from the dark photon dark matter and the ultralight scalar experiments appear consistently, we can confidently declare the verification of our model. In addition, given the scalar-photon coupling in the strong region, the scalar's high-temperature evolution is affected by the standard model plasma, which sets the early displacement, modifies the start of oscillation, and even enhances the scalar's signal. To understand the whole setup classified under the exactness of the $\mathbb{Z}_2$ symmetry, one can refer to Fig. 1.

To protect the CP-even scalar's naturalness caused by the heavy messengers and inspired by the former works on the discrete symmetries [97–104], we embed the varying kinetic mixing into N copies of the universes, where the $\mathbb{Z}_N$ symmetry rebuilds the global $U(1)$ shift symmetry in the discrete form. In such $\mathbb{Z}_N$-protected model, the scalar's lowest order mass term becomes Φ^N/Λ^{N-4}, which reveals the exponential suppression of the quantum correction. For example, we only need $N \sim 10$ to suppress the scalar mass correction all the way down to 10^{-33}eV. Furthermore, to understand the additional cancellation from the exact $\mathbb{Z}_2$ symmetry and gain an accurate analytical result, we expand the $\mathbb{Z}_N$ Coleman-Weinberg formally calculated to the leading order in [98, 102] to the arbitrary orders with two entirely different methods, i.e., the Fourier transformation and the cosine sum rules. Other topics of the varying kinetic mixing from the supersymmetric Dirac gaugino model and the dark matter models via other cosmologically varying portals are preliminarily discussed in our work.

The remainder of this paper is organized as follows. In Sec. II, we build the minimal model for the scalar-controlled kinetic mixing and show that the scalar-photon coupling appears simultaneously. Based on whether the scalar-messenger couplings are $\mathbb{Z}_2$-invariant, we categorize the theory into the type-A model with the linear scalar-photon coupling and the type-B model with the quadratic scalar-photon coupling. In Sec. III, for the type-A and the type-B models, we do the systematic classification of the scalar evolution jointly affected by the thermal effect, bare potential

effect, and cosmological expansion. In Sec. IV, we discuss the dark photon dark matter freeze-in via the varying kinetic mixing. We also discuss the detection of the dark photon dark matter with the experimental targets set by the scalar mass and the experiments of the non-relativistic ultralight scalar relic with targets set by the dark photon dark matter freeze-in. In Sec. V, we build the $\mathbb{Z}_N$ model to protect the scalar's naturalness from the heavy messengers, discuss the extra cancellation from the exact $\mathbb{Z}_2$, and calculate the $\mathbb{Z}_N$-invariant Coleman-Weinberg potential utilizing the Fourier transformation and the cosine sum rules. In Sec. VI, we generate the varying kinetic mixing and the dark axion portal simultaneously from the Dirac gaugino model. In Sec. VII, we preliminarily explore the dark matter models via other cosmologically varying portals and their experimental signals. Finally, in Sec. VIII we summarize our results. We also provide a series of appendices containing the calculational details, such as the analytical solutions of the high-temperature scalar evolution in Appendix. A, the freeze-in of the dark photon dark matter in Appendix. B, and the exact expansion of the $\mathbb{Z}_N$ Coleman-Weinberg potential using the Fourier transformation and cosine sum rules in Appendix. C.

II. MINIMAL MODEL

In the beginning, let us recall the well-known constant kinetic mixing of the field strengths of the standard model $U(1)_Y$ and the dark $U(1)$, which can be written as

$$\frac{\epsilon}{2} F^{\mu\nu} F'_{\mu\nu}. \tag{1}$$

Here, the kinetic mixing can be generated at the one-loop level by a pair of vector-like fermions Ψ and Ψ' charged as (e, e') and $(e, -e')$ under $U(1)_Y \times U(1)_d$ [2]. In the low energy limit, the value of the constant kinetic mixing is

$$\epsilon = \frac{ee'}{6\pi^2} \log \frac{M}{M'}, \tag{2}$$

where M and M' are the masses of Ψ and Ψ', respectively. To build the varying kinetic mixing, we eliminate the constant kinetic by imposing the mass degeneracy $M = M'$ and promote ϵ to a dynamical variable $\epsilon(x)$ by imposing the $\mathbb{Z}_2$ symmetry under the dark charge conjugation, i.e.,

$$\mathcal{C}_d : A'(x) \to -A'(x), \quad \epsilon(x) \to -\epsilon(x). \tag{3}$$

By doing so, the constant kinetic mixing is forbidden because FF' is odd under $\mathcal{C}_d$, whereas the varying kinetic mixing $\epsilon(x)FF'$ is permitted.

To realize this from the top-down theory, we introduce the Lagrangian

$$\mathcal{L}_{\mathrm{UV}} \supset y\Phi\bar{\Psi}\Psi + y'\Phi\bar{\Psi}'\Psi' + \mathrm{h.c.} - M(\bar{\Psi}\Psi + \bar{\Psi}'\Psi') - \lambda\left(|\Phi|^2 - \frac{f^2}{2}\right)^2, \tag{4}$$

where Φ is a neutral complex scalar and $y^{(\prime)}$, M, λ, f are chosen to be real parameters for simplicity. In the ground state, the approximate global $U(1)$ symmetry of the potential is spontaneously broken by $\Phi = \frac{f}{\sqrt{2}}e^{i(\phi/f+c)}$ whose angular components include a CP-even pseudo-Goldstone boson ϕ and an arbitrary phase c. Knowing that the transformation on the real scalar $\phi \to -\phi - (2c - \pi) f$ is equivalent to $\Phi \to -\Phi^\dagger$, under which the Yukawa interactions in Eq. (4) flip signs, we choose $c = \pi/2$ to fix the phase factor throughout the paper. Given this, we define the dark charge conjugation of the UV theory as

$$\mathcal{C}_d : A \to A, \ A' \to -A', \ \phi \to -\phi, \ \Psi \leftrightarrow \Psi'. \tag{5}$$

If $y' = -y$ and $M' = M$, the Lagrangian is invariant under $\mathcal{C}_d$. We will see from the later discussion that as long as ϕ has a nonzero vacuum expectation value (VEV), the dynamical kinetic mixing can be generated. This is because,

in this case, $\Psi^{(\prime)}$'s effective masses become

$$M^{(\prime)}(\phi) = M \left[1 + r^{(\prime)} \sin \frac{\phi}{f} \right], \quad \text{where } r^{(\prime)} = \frac{\sqrt{2}\, y^{(\prime)} f}{M}, \tag{6}$$

From Eq. (6), we know that the degeneracy of the effective masses is broken by ϕ when $y \neq y'$. In Eq. (6) and the rest part of this paper, we use "$(\prime)$" to denote the physical quantities in the SM sector (without "$\prime$") and the dark sector (with "$\prime$"). After integrating out $\Psi^{(\prime)}$, the Lagrangian of the effective kinetic mixing becomes

$$\mathcal{L}_{\mathrm{IR}} \supset \frac{\epsilon}{2} F_{\mu\nu} F'^{\mu\nu}, \quad \text{where } \epsilon = \frac{\sqrt{2}\, ee'\,(y - y')}{6\pi^2 M} f \sin \frac{\phi}{f}. \tag{7}$$

When $\phi \ll f$, the kinetic mixing in Eq. (7) can be linearized as

$$\epsilon \simeq \frac{\phi}{\Lambda_{\mathrm{KM}}}, \quad \text{where } \Lambda_{\mathrm{KM}} = \frac{6\pi^2 M}{\sqrt{2}\, ee'(y - y')}. \tag{8}$$

Therefore, in our model, the kinetic mixing varies with ϕ's cosmological evolution. Since the crucial point of this model is that the kinetic mixing vanishes when ϕ relaxes to the minimum, we should align the potential's minimum with the kinetic mixing's zero. To realize this, we introduce the $\mathcal{C}_d$-even tadpole term

$$\mathcal{L}_{\mathrm{UV}} \supset -\frac{im_0^2 f}{\sqrt{2}} \Phi + \text{h.c.}, \tag{9}$$

which arises as the potential

$$V_0 = m_0^2 f^2 \left[1 - \cos\left(\frac{\phi}{f}\right) \right] \tag{10}$$

when the phase factor is $c = \pi/2$. Conversely, because the system is invariant under $\mathcal{C}_d$ listed in Eq. (5), V_0 has to be the even function of ϕ, while ϵ is the odd function of ϕ. In this case, the phase difference between ϵ and V_0 is $(n + 1/2)\pi$, where $n = 0, \pm 1, \pm 2 \cdots$. Therefore, under the protection of $\mathbb{Z}_2$ symmetry of the dark charge conjugation $\mathcal{C}_d$, the potential's minima are necessarily aligned with the zeros of the kinetic mixing. During the cosmological evolution, ϕ initially stays at the nonzero displacement, so the portal is opened. As the universe expands, the pseudo-Goldstone boson ϕ begins the damped oscillation around zero, so the portal is partially closed. In today's universe, ϕ consists of the nonrelativistic ultralight relic in the mass range $10^{-33}\mathrm{eV} \lesssim m_0 \ll \mathrm{eV}$, so the kinetic mixing has the nonzero residual. More fundamentally, we can interpret the time-varying kinetic mixing from the perspective of symmetry, since the nonzero kinetic mixing results from the $\mathbb{Z}_2$ violation. In the early universe, the $\mathbb{Z}_2$ symmetry is spontaneously broken by ϕ's nonzero displacement. In the late universe, ϕ oscillates toward zero, and the $\mathbb{Z}_2$ symmetry is restored. Such early-time breaking and late-time restoration of the global symmetry is regarded as the inverse symmetry breaking in [105–108] for other motivations.

Let us classify the theory based on whether the Lagrangian is exactly invariant under the dark charge conjugation $\mathcal{C}_d$ or not. As shown in Eq. (5), when $y' = -y$, the $\mathbb{Z}_2$ symmetry of $\mathcal{C}_d$ is strictly preserved. When $y' \neq -y$, the $\mathbb{Z}_2$ symmetry is broken, which induces the two-loop constant kinetic mixing and the one-loop tadpole of Φ. Here, the small Yukawas highly suppress the two-loop constant mixing, which is $\epsilon \sim (M/\Lambda_{\mathrm{KM}})^2/ee'$. The cancellation of Φ-tadpole needs fine-tuning, which can be entirely solved in the framework of $\mathbb{Z}_N$-protected model discussed in Sec. V. Therefore, the $y' \neq -y$ case still has the approximate $\mathbb{Z}_2$ symmetry. Based on the discussion above, we consider the following two types of the models in this work:

$$\text{Type-A: } y' = 0, \text{ Approximate } \mathbb{Z}_2. \quad \text{Type-B: } y' = -y, \text{ Exact } \mathbb{Z}_2. \tag{11}$$

Due to ϕ-$\Psi^{(\prime)}$ interaction, the scalar-photon coupling emerges from UV physics. At the one-loop level, the coupling between the CP-even scalar ϕ and the photon can be written as

$$\mathcal{L}_{\mathrm{IR}} \supset \frac{1}{4} \left(\frac{\Delta\alpha_{\mathrm{em}}}{\alpha_{\mathrm{em}}} \right) F_{\mu\nu} F^{\mu\nu}, \tag{12}$$

where

$$\frac{\Delta\alpha_{\rm em}}{\alpha_{\rm em}} = -\frac{e^2}{6\pi^2}\left[\log M(\phi) + \log M'(\phi)\right] \supset \frac{\sqrt{2}e^2}{6\pi^2}\left[-\frac{(y+y')\,f}{M}\sin\left(\frac{\phi}{f}\right) + \frac{(y^2+y'^2)\,f^2}{\sqrt{2}M^2}\sin^2\left(\frac{\phi}{f}\right)\right]. \tag{13}$$

Utilizing the classification in Eq. (11), we have

$$\text{Type-A: } y' = 0, \quad \frac{\Delta\alpha_{\rm em}}{\alpha_{\rm em}} \sim \frac{\alpha_{\rm em}y\phi}{M}, \qquad \text{Type-B: } y' = -y, \quad \frac{\Delta\alpha_{\rm em}}{\alpha_{\rm em}} \sim \frac{\alpha_{\rm em}y^2\phi^2}{M^2}, \tag{14}$$

where the type-A and type-B models have linear and quadratic scalar-photon couplings, respectively. To compare with the experiments testing the fine-structure constant variation and the equivalence principle violation, we define the dimensionless constants $d_{\gamma,i}$ $(i=1,2)$ through

$$\frac{\Delta\alpha_{\rm em}}{\alpha_{\rm em}} := \left(\frac{\sqrt{4\pi}\phi}{m_{\rm pl}}\right)^i \frac{d_{\gamma,i}}{i} \qquad (i=1,2), \tag{15}$$

where the indices "$i=1$" and "$i=2$" denote the type-A and type-B models, respectively. Comparing Eq. (15) with Eq. (14), we have

$$d_{\gamma,i} \sim \left(\frac{m_{\rm pl}}{e'\Lambda_{\rm KM}}\right)^i \quad (i=1,2). \tag{16}$$

Some other papers quantify the fine-structure constant variation through the notation $\Delta\alpha_{\rm em}/\alpha_{\rm em} = \phi^i/\Lambda^i_{\gamma,i}$ $(i=1,2)$. Combining this notation with Eq. (14), we have $\Lambda_{\gamma,i} \sim e'\Lambda_{\rm KM}$ $(i=1,2)$, which means that e' determines the hierarchy between the effective energy scale of the varying kinetic mixing and the varying fine structure constant. In the rest part of this paper, we use the first notation, i.e., $d_{\gamma,i}$ $(i=1,2)$. In Eq. (16), we find that for the fixed $\phi FF'$ operator inducing the effective kinetic mixing, smaller e' leads to larger $y^{(\prime)}$ such that the testable signals of the $\alpha_{\rm em}$ variation get stronger. Such small dark gauge coupling can be naturally generated in the large volume scenario in string compactification [18, 109, 110].

To understand the setup of our model intuitively, one can refer to Fig. 1. The left panel shows that when $\mathbb{Z}_2$ symmetry is imposed, the constant kinetic mixing is canceled, but the scalar-controlled kinetic mixing survives. In this case, as ϕ evolves during the cosmological evolution, the kinetic mixing becomes time-dependent. This provides a novel mechanism to generate a small but non-zero kinetic mixing. The right panel reveals that the scalar-photon couping is also generated as the byproduct when UV physics is considered. Based on the exactness of the $\mathbb{Z}_2$ symmetry, the theory can be classified as the type-A model with the linear scalar-photon couping and the type-B model with the quadratic scalar-photon couping. We will see from the later discussion that such scalar-photon couplings affect ϕ's evolution via the thermal effect from the SM plasma. They also change the fine-structure constant and violate the equivalence principle, which provides essential prospects for the experimental tests.

III. COSMOLOGICAL HISTORY

In this section, we jointly discuss the ultralight scalar's cosmological evolution, which is affected by the scalar bare potential, thermal effect, and cosmological expansion. According to [102, 111], the lowest order thermal contribution containing $\alpha_{\rm em}$ is at the two-loop level, and the free energy contribution coming from that can be written as

$$F_T \simeq \frac{5\pi\sum_i q_i^2}{72}\alpha_{\rm em}T^4 \times \mathcal{S}(T), \quad \text{where } \mathcal{S}(T) = \begin{cases} 1 & (T \gtrsim m_e) \\ \dfrac{18}{5\pi^3}\dfrac{m_e^2}{T^2}e^{-2m_e/T} & (T \ll m_e) \end{cases}. \tag{17}$$

In Eq. (17), the suppression factor $\mathcal{S}(T)$ is 1 when $e^\pm$ (as well as other species of heavier particles carrying the $U(1)_{\rm em}$ charges) are relativistic but decreases exponentially after $e^\pm$ becomes non-relativistic. The factor $\sum_i q_i^2$ (q_i is the

electric charge of the particle "i") quantifies the thermal contribution to the total free energy when $U(1)_{\rm em}$ charged particles are relativistic in the thermal bath. As shown in Eq. (13), when ϕ has nonzero VEV, the fine structure constant is modified, based on which ϕ's thermal potential can be obtained by replacing $\alpha_{\rm em}$ in Eq. (17) by $\alpha_{\rm em}(\phi)$. After combining Eq. (13) and Eq. (17), we have

$$
\begin{cases}
\text{Type-A:} \quad V_T \simeq -m_T^2 f^2 \sin \dfrac{\phi}{f}, \quad \text{where} \quad \dfrac{m_T}{\mathcal{S}^{1/2}} \sim \alpha_{\rm em} r^{1/2} \dfrac{T^2}{f} \\[3mm]
\text{Type-B:} \quad V_T \simeq \dfrac{1}{2} m_T^2 f^2 \sin^2 \dfrac{\phi}{f}, \quad \text{where} \quad \dfrac{m_T}{\mathcal{S}^{1/2}} \sim \alpha_{\rm em} r \dfrac{T^2}{f}
\end{cases}, \tag{18}
$$

where the definition of r can be found in Eq. (6).

Here, we choose $T_{\rm rh}$ to be much smaller than the heavy fermion mass, i.e., M, so Ψ's contribution to the thermal potential is exponentially suppressed. In addition, because we do not include the dark electrons and positrons, the thermal effect from the dark sector is also negligible. Fig. 3 shows how the potential changes as the temperature varies and how ϕ moves under different circumstances. From lighter (yellow) to darker color (dark red), the ratios of thermal mass over the bare mass are $m_T/m_0 = 5, 4, 3, 2, 1, 0$. For the bare potential, V_0 has the minimum at $\phi/f = 0$. As for the thermal potential, the local minimums of the type-A and type-B models are (Here $n = 0, \pm 1, \pm 2, \cdots$)

$$
\text{Type-A:} \quad \frac{\phi_{\min}}{f} = \arctan\left(\frac{m_T^2}{m_0^2}\right) + 2n\pi, \quad \text{Type-B:} \quad \frac{\phi_{\min}}{f} = \begin{cases} n\pi & (m_T > m_0) \\ 2n\pi & (m_T \leq m_0) \end{cases}. \tag{19}
$$

In the following discussion, we focus on the range $-2\pi f \leq \phi \leq 2\pi f$ without loss of generality. For the type-A model, since $m_T \gg m_0$ in the early epoch, the minimum is $\phi_{\min} \simeq \pi f/2$. When $m_T \ll m_0$, the potential's minimum continuously shifts to zero. For the type-B model, when $m_T > m_0$, within the $2\pi f$ periodicity there are three local minimums, i.e., $\phi_{\min} = 0, \pm \pi f$. When $m_T \leq m_0$, only $\phi_{\min} = 0$ is the minimum. We should notice that during the entire process, ϕ keeps the classical motion without the tunneling: Even though ϕ is initially located inside the false facuum $\pi f/2 \lesssim \phi_{\rm rh} \lesssim 3\pi f/2$, because f is large, the vacuum decay from πf to 0 is highly suppressed such that it is much slower than the universe's expansion [112–118].

Knowing from Eq. (18) that m_T has the same temperature power law as H when $T \gtrsim m_e$ ($\mathcal{S} \simeq 1$), we define a dimensionless quantity

$$
\eta := \frac{2m_T}{\mathcal{S}^{1/2} H} \sim \alpha_{\rm em} \frac{m_{\rm pl}}{f} \times \begin{cases} r^{1/2} & (\text{Type-A}) \\ r & (\text{Type-B}) \end{cases} \tag{20}
$$

to classify ϕ's evolution. Here, $r \sim yf/M$, which is defined in Eq. (6). The motion of ϕ is underdamped if $\eta > 1$, because the thermal effect dominates over the universe's expansion; In contrast, if $\eta < 1$, ϕ's motion is overdamped under the Hubble friction. $\eta = 1$ is the critical value separating the two moving patterns mentioned above. To relate η with experimental observables which are quantified by $d_{\gamma,i}$ ($i = 1, 2$), we write η as

$$
\text{Type-A:} \quad \eta \sim \left(\frac{\alpha_{\rm em} d_{\gamma,1} m_{\rm pl}}{f}\right)^{\frac{1}{2}}, \quad \text{Type-B:} \quad \eta \sim (\alpha_{\rm em} d_{\gamma,2})^{\frac{1}{2}}. \tag{21}
$$

In the high-T limit where m_T dominates over m_0, ϕ's thermal evolution can be solved in the linear approximation of the equation of motion, which can be found in Appendix A. Since we compare m_T and m_0 to determine whether the thermal effect dominates over the effect from the bare potential, we define the critical temperature T_* at which $m_T = m_0$. Combining Eq. (18) and Eq. (20), we have

$$
T_* \sim \max\left[0.1 m_e, \left(\frac{m_0\, m_{\rm pl}}{\eta}\right)^{1/2}\right], \tag{22}
$$

where the concrete formulas of η for the type-A and the type-B models can be found in Eq. (21). Now, let us briefly explain the meaning of Eq. (22). For m_T to be smaller than m_0, we only need one of the following two conditions
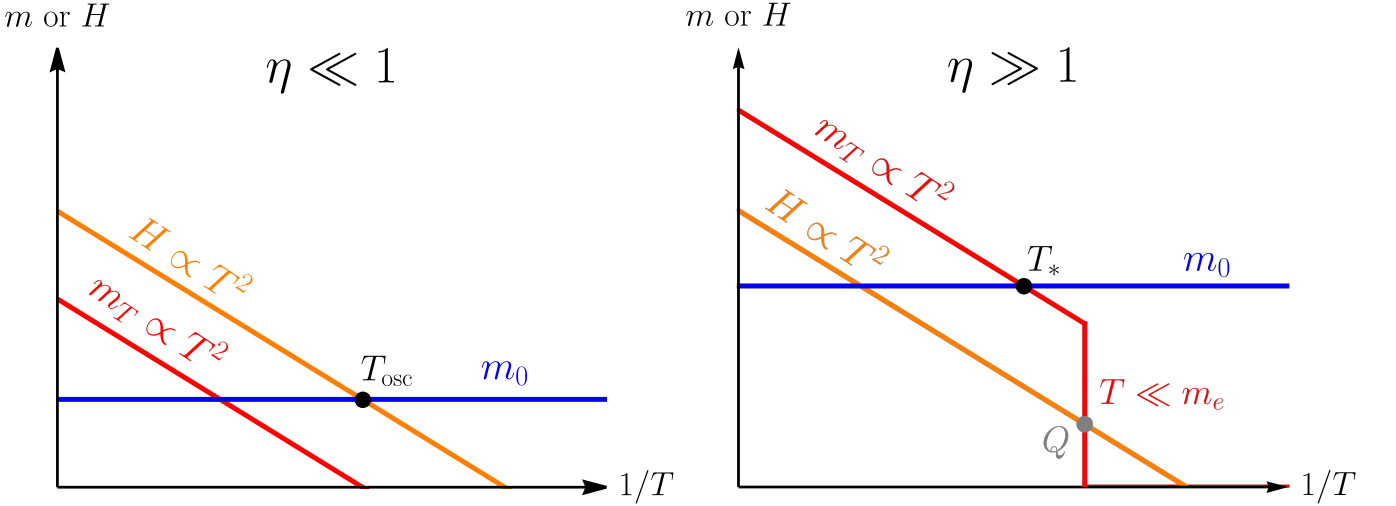
Figure 2. The evolution of m_T (red), m_0 (blue) and H (orange) as the universe expands. Because H and m_T are both proportional to T^2 when $T \gtrsim m_e$, the orange and red lines are approximately parallel with each other in the log-log diagram until $T \sim m_e$. Here, $\eta \sim m_T/H$ when $T \gtrsim m_e$, which is already defined in Eq. (22). **Left**: $\eta \ll 1$. Because the thermal effect from the SM bath is negligible, the ultralight scalar's evolution can be classified as the standard misalignment. In this case, ϕ stays constant at the early stage and begins the oscillation when $H \sim m_0$, which is labeled as $T_{\rm osc}$. **Right**: $\eta \gg 1$. The thermal effect is important for the scalar's evolution. In the plot, point T_* and point "Q" denote the moment when $m_T = m_0$ and $H \sim m_T$, respectively. Here, $H_Q \sim 10^{-16}/\log^2 \eta$ eV. When $T \gg T_*$, ϕ converges to the minimum of the thermal potential obeying the power law $|\phi - \phi_{\rm min}| \propto T^{1/2}$ where $\phi_{\rm min} = \pi f/2$ for the type-A model and $\phi_{\rm min} = \pm\pi f$ for the type-B model. We merely show the $m_0 \gtrsim H_Q$ case, because if $m_0 \lesssim H_Q$, ϕ's movement is nothing more than the late-time standard misalignment with the initial condition fixed by the early time thermal effect. For the type-A model, when $T \gtrsim m_e$, ϕ tracks the potential minimum $\phi_{\rm min} = f \arctan(m_T^2/m_0^2)$. As the temperature drops far below the electron mass, ϕ cannot track the minimum and begins to oscillate. For the type-B model, we focus on the $\pi f/2 \lesssim \phi_{\rm rh} \lesssim 3\pi f/2$ case. When $T \gg T_*$, ϕ is trapped inside the local minimum $\phi_{\rm min} = \pi f$. Thereafter, when $T \lesssim T_*$, ϕ begins oscillating around the bare minimum $\phi_{\rm min} = 0$. Here we have $T_* \ll T|_{3H=m_0}$, which means the oscillation is postponed. Therefore, the scalar is in the phase of trapped misalignment.

to be satisfied: The first condition is $T \ll m_e$ such that m_T is exponentially suppressed. The second condition is that the unsuppressed part of the scalar thermal mass, i.e., $m_T/\mathcal{S}^{1/2}$, is smaller than m_0. Since T_* is defined as the temperature when $m_T = m_0$, we use $T \lesssim T_*$ and $m_T \gtrsim m_0$ interchangeably. In Fig. 4 showing the typical numerical solutions of the ϕ evolution, we define the dimensionless temperature $\widetilde{T} := T/T|_{3H=m_0}$ with the extra "$\sim$", then we have the dimensionless critical temperature $\widetilde{T}_* \sim \max[m_e/(m_0 m_{\rm pl})^{1/2}, 1/\eta^{1/2}]$ for the moment when $m_T = m_0$.

Before discussing the scalar's evolution, let us give the following definitions:

$$\textbf{Standard Misalignment: } \eta \ll 1, \qquad \textbf{Thermal Misalignment: } \eta \gtrsim 1. \tag{23}$$

These definitions are based on the value of η, which quantifies how large the thermal effect is compared with the effect of the bare potential shown in Eq. (10). When η is much smaller than one, the thermal effect is negligible, so it can be classified as the standard misalignment in which one solely needs to compare the effects of the bare potential and the universe expansion. When η is of order unity or even larger, the thermal effect can never be omitted, and one should consider all three effects (thermal effect, bare potential, universe expansion) jointly. Now, let us discuss each situation one by one.

A. Standard Misalignment: $\eta \ll 1$

In this case, when $3H \gtrsim m_0$, ϕ obeys

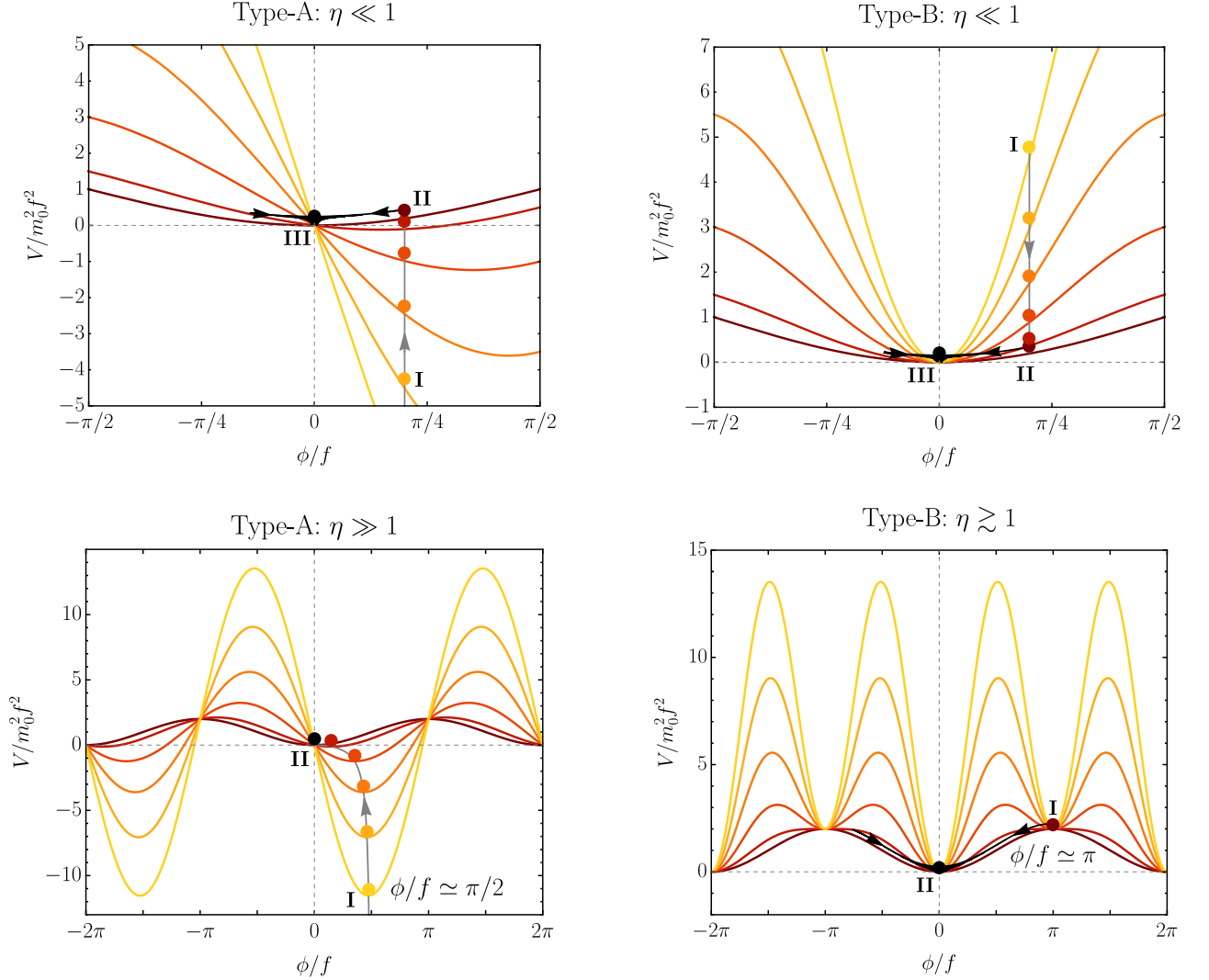$$\phi - \phi_{\rm min} \propto T^{\frac{\eta^2}{4}}, \tag{24}$$

Figure 3. The typical scalar evolution trajectories in the early universe. The lighter (darker) color in these diagrams denotes higher (lower) temperature. From the yellow line to the dark red line, $m_T/m_0 = 5, 4, 3, 2, 1, 0$. Here, η quantifies the thermal effect, whose definition can be found in Eq. (20). **Upper left and upper right**: For both type-A and type-B models, when $\eta \ll 1$, the thermal effects are negligible. Here, ϕ is nearly frozen at the early stage (gray arrowed line from point I to point II). When $3H \simeq m_0$ (point II), ϕ begins the damped oscillation with the amplitude $|\phi| \propto T^{3/2}$ (black arrowed line from point II to point III) and converges to the origin (point III). **Lower left**: For the type-A model with $\eta \gg 1$, in the high-temperature environment, ϕ converges to $\pi f/2$ (point I) following $|\phi - \pi f/2| \propto T^{1/2}$. As the temperature falls, m_T/m_0 also decreases. During the stage when $T \gtrsim m_e$, the variation of the thermal potential is adiabatic, so ϕ tracks the potential minimum $\phi_{\min} = f \arctan\left(m_T^2/m_0^2\right)$ as shown in Eq. (19) (gray arrowed line from point I to point II). When $T \ll m_e$, since the too fast variation of the thermal potential violates the adiabatic condition, ϕ can no longer stay in the minimum and starts to oscillate following $|\phi| \propto T^{3/2}$. We do not show this stage of ϕ's movement in the diagram because the amplitude is too small to visualize compared with f. **Lower right**: For the type-B model with $\eta \gtrsim 1$ and ϕ initially trapped inside the wrong vacuum, ϕ does damped oscillation $|\phi - \pi f| \propto T^{1/2}$ when $T \gg T_*$ and converges to πf. When $T \lesssim T_*$, $V''|_{\phi=\pi f} \lesssim 0$, so ϕ begins the damped oscillation with $|\phi| \propto T^{3/2}$ (black arrowed line from point I to point II).

which means ϕ is nearly frozen in the early universe. To have an overall understanding of the cosmological history, one could refer to the left panel of Fig. 2: The H-line (orange) is higher than the m_T-line (red) during the whole process, meaning that the thermal effect is negligible so one only needs to focus on the H-line (orange) and m_0-line (blue). After the crossing of H-line and m_0-line, the scalar begins the damped oscillation whose amplitude obeys the power law $|\phi| \propto T^{3/2}$. The upper left and upper right panels of Fig. 3 show how ϕ moves for the type-A and type-B models separately when $\eta \ll 1$: From point I to point II, ϕ keeps nearly the same. This means that the initial field

displacement determines ϕ's starting oscillation amplitude $|\phi|_{\mathrm{osc}}$. Here, we focus on the model with the natural initial condition, i.e., $|\phi|_{\mathrm{osc}}/f \sim \mathcal{O}(1)$. In the late time, ϕ begins to oscillate at the temperature

$$T_{\mathrm{osc}} = T|_{3H=m_0} \sim \text{few} \times 10^{-1}\mathrm{eV} \times \left(\frac{m_0}{10^{-28}\mathrm{eV}}\right)^{\beta_T}, \quad \text{where } \beta_T = \begin{cases} \dfrac{1}{2} & (m_0 \gtrsim 10^{-28}\mathrm{eV}) \\ \dfrac{2}{3} & (10^{-33}\mathrm{eV} \lesssim m_0 \lesssim 10^{-28}\mathrm{eV}) \end{cases}. \tag{25}$$

β_T in Eq. (25) and later mentioned β_ϕ in Eq. (26) are determined by H's power law of T, which is T^2 at the radiation-dominated universe, and $T^{3/2}$ at the matter-dominated universe. In Eq. (25), we choose $m_0 \simeq 10^{-28}\mathrm{eV}$ as the reference value simply because the scalar oscillation happens at the matter-radiation equality $T \sim \mathrm{eV}$ for such scalar mass. Before or after $T \sim \mathrm{eV}$, H has different power laws of T. Such oscillation is labeled as black oscillatory lines from point II to point III in Fig. 3 and is also represented as blue lines in Fig. 4. Because the inflation smears out the field anisotropy, ϕ does spatially homogeneous oscillation, which can be written as

$$\phi(t) \simeq |\phi| \cos(m_0 t), \quad \text{where } |\phi| = \frac{\sqrt{2\rho_\phi}}{m_0} \propto T^{3/2}. \tag{26}$$

From [119, 120] one knows that ϕ satisfies $\rho_\phi \propto T^3$ and $w_\phi = p_\phi/\rho_\phi \simeq 0$, so ϕ is part of the dark matter with the fraction $\mathcal{F} = \Omega_\phi/\Omega_{\mathrm{dm}}$. Without loss of generality, we choose $\mathcal{F} = 10^{-3}$ as a benchmark value, such that astrophysical and cosmological measurements like Lyman-α forest [121–126], CMB/LSS [127, 128], galaxy rotational curves [129–133], and the observations of the ultra-faint dwarf galaxies [134] do not exclude the parameter space where $m_0 \lesssim 10^{-19}\mathrm{eV}$. After substituting Eq. (25) into Eq. (26), one can easily get the starting oscillation amplitude

$$|\phi|_{\mathrm{osc}} \sim \text{few} \times 10^{16}\mathrm{GeV} \times \left(\frac{\mathcal{F}}{10^{-3}}\right)^{1/2} \left(\frac{10^{-28}\mathrm{eV}}{m_0}\right)^{\beta_\phi}, \quad \text{where } \beta_\phi = \begin{cases} \dfrac{1}{4} & (m_0 \gtrsim 10^{-28}\mathrm{eV}) \\ 0 & (10^{-33}\mathrm{eV} \lesssim m_0 \lesssim 10^{-28}\mathrm{eV}) \end{cases} \tag{27}$$

In the case where $m_0 \gg 10^{-25}\mathrm{eV}$, ϕ's de Broglie wavelength is much smaller than the scale of the Milky Way halo, so ϕ behaves like a point-like particle similar to other cold DM particles. For this reason, ϕ's local density is $\rho_{\phi,\mathrm{local}} \simeq \mathcal{F}\rho_{\mathrm{local}}$, where $\rho_{\mathrm{local}} \simeq 0.4\mathrm{GeV/cm}^3$ is DM's local density near earth. By effectively adding an enhancement factor

$$\mathcal{E} = \left(\frac{\rho_{\mathrm{local}}}{\rho_{\mathrm{average}}}\right)^{1/2} \simeq 6 \times 10^2 \tag{28}$$

where $\rho_{\mathrm{average}} = \rho_c \Omega_{\mathrm{DM}} \simeq 1.3\,\mathrm{keV/cm}^3$ on $|\phi|$ in Eq. (26), we get ϕ's amplitude today near the earth, which is $|\phi|_0 \simeq (2\mathcal{F}\rho_{\mathrm{local}})^{1/2}/m_0$. Here, $|\phi|_0$ denotes ϕ's local oscillation amplitude today. If $m_0 \ll 10^{-25}\mathrm{eV}$, oppositely, ϕ cannot be trapped inside the Milky Way halo's gravitational potential well. In this case, today's ϕ field is homogeneous, so the enhancement factor in Eq. (28) should not be included, from which we have $|\phi|_0 = (2\mathcal{F}\rho_{\mathrm{average}})^{1/2}/m_0$. ϕ's oscillation amplitude in the middle mass range needs numerical simulation, which is left for future exploration.

B. Thermal Misalignment: $\eta \gtrsim 1$

As long as η is of order unity or even larger, the thermal effect from the SM plasma plays a decisive role in ϕ's evolution in the early universe. To understand the combined effects on ϕ's movement from the thermal potential, bare potential, and the universe's expansion, one can refer to the right panel of Fig. 2: At the early stage, since m_T (red) and H (orange) are both proportional to T^2, their lines are approximately parallel in the plot with the log-log scale. Here we neglect the g_* variation, which only leads to an $\mathcal{O}(1)$ modification. In the plot, we label the cross point of m_T-line (red) and m_0-line (blue) with "T_*", which is already defined in Eq. (22). When $T \lesssim T_*$, the effect from the bare potential dominates over the effect from the thermal potential. When $T \ll m_e$, the m_T-line drops fastly
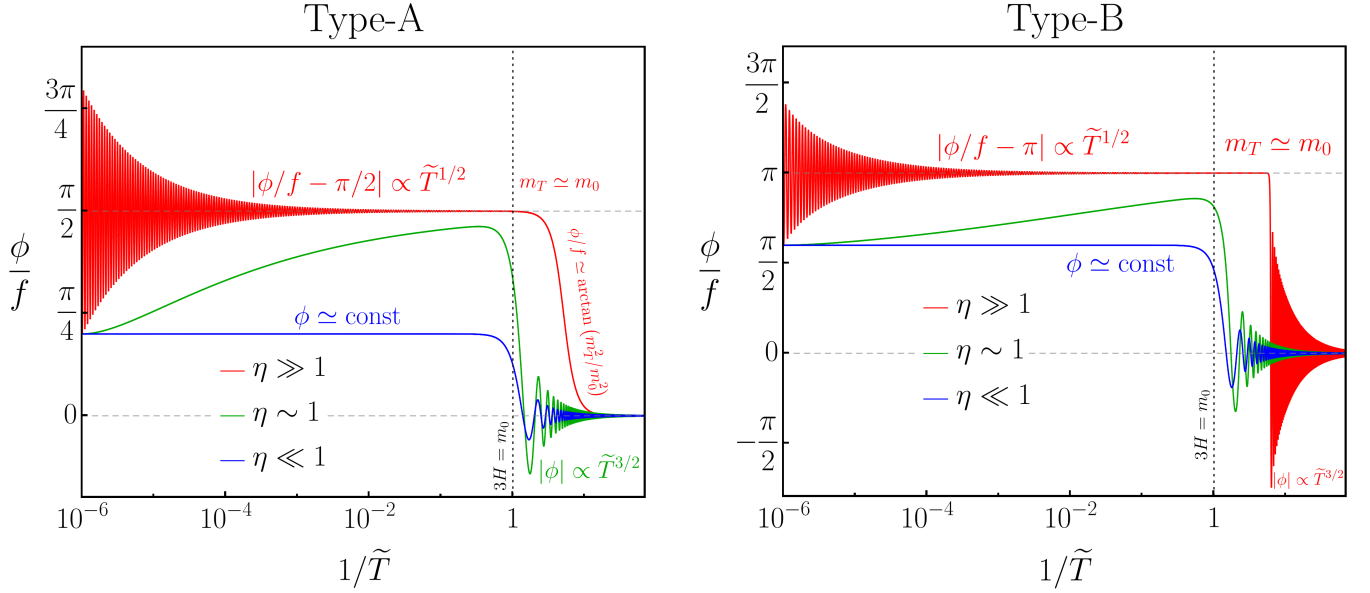
Figure 4. ϕ's typical numerical solutions. In these two plots, we define the dimensionless quantity $\widetilde{T} \coloneqq T/T|_{3H=m_0}$, so at point $\widetilde{T} = 1$ we have $3H = m_0$. The red, green, and blue lines represent the $\eta \gg 1$, $\eta \sim 1$, and $\eta \ll 1$ cases, respectively. **Left**: The type-A model ($y' = 0$). For the red line ($\eta \gg 1$), when $\widetilde{T} \gg \widetilde{T}_*$, ϕ does the damped oscillation scaled as $|\phi - \pi f/2| \propto \widetilde{T}^{1/2}$, so it converges to $\pi f/2$. Remembering the T_*'s definition in Eq. (22), we label the point where $T \simeq T_*$ as "$m_T \simeq m_0$". As the temperature decreases, ϕ tracks potential's minimum $\phi_{\min} = f \arctan(m_T^2/m_0^2)$ until the temperature drops below the electron mass. After that, ϕ cannot track the instant changing of the potential and begins the damped oscillation scaled as $|\phi| \propto \widetilde{T}^{3/2}$. In this plot, we have not shown ϕ's oscillation afterward because its amplitude is too small to be visualized. For the green line ($\eta \sim 1$), when $\widetilde{T} \gtrsim 1$, ϕ gradually slides to the thermal potential minimum $\pi f/2$ following Eq. (30). When $\widetilde{T} \sim 1$, ϕ begins the damped oscillation obeying $|\phi| \propto \widetilde{T}^{3/2}$. The blue line ($\eta \ll 1$) represents the standard misalignment where the thermal effect is negligible during the process. There, $\phi \simeq$ const until $\widetilde{T} \simeq 1$. After that, ϕ begins to oscillate following $|\phi| \propto \widetilde{T}^{3/2}$. **Right**: The type-B model ($y' = -y$). The red line represents the situation where $\eta \gg 1$ and ϕ's initial condition is $\pi f/2 \lesssim \phi_{\rm rh} \lesssim 3\pi f/2$. In this case, when $\widetilde{T} \gtrsim \widetilde{T}_*$, ϕ does the damped oscillation $|\phi - \pi f| \propto \widetilde{T}^{1/2}$ during which ϕ converges to πf. When $\widetilde{T} \lesssim \widetilde{T}_*$, or equivalently speaking, $m_T \lesssim m_0$, we have $V''|_{\phi=\pi f} \lesssim 0$, so ϕ rolls down from πf and oscillates like $|\phi| \propto \widetilde{T}^{3/2}$. We can see that the red line's oscillation is postponed compared with the standard misalignment beginning at $\widetilde{T} \simeq 1$. For this reason, the red line is in the phase of the trapped misalignment. The green line represents the situation where $\eta \sim 1$ and $\pi f/2 \lesssim \phi_{\rm rh} \lesssim 3\pi f/2$. In this case, ϕ gradually slides to the thermal potential minimum πf as shown in Eq. (30). At the point $\widetilde{T} \simeq 1$, ϕ begins the damped oscillation scaled as $|\phi| \propto \widetilde{T}^{3/2}$. The blue line represents the standard misalignment mechanism where the thermal effect is inferior to the bare potential effect, i.e., $\eta \ll 1$. Similar to the discussion of the blue line in the left panel, ϕ stays constant in the early universe and then begins the oscillation when $\widetilde{T} \simeq 1$. Even though the red lines in the left and right panels are qualitatively different, the green and blue lines are quite similar in terms of the oscillation temperature ($\widetilde{T} \simeq 1$). The main difference between the green and blue lines is that the green lines' initial displacements are thermally determined to be $|\phi|_{\rm osc} \simeq |\phi_{\min}|$, but the blue lines' oscillation amplitude depends on their initial conditions.

following $e^{-m_e/T}$ and crosses the H-line. We label the cross point of the m_T-line and the H-line as "Q", and we have

$$T_Q \sim m_e/\log\eta, \quad H_Q \sim 10^{-16}/\log^2\eta \text{ eV}. \tag{29}$$

As we will see in the rest of this section, comparing m_0 and H_Q is vital in determining the temperature at which ϕ starts the late-time oscillation.

Let us first discuss ϕ's movement in the stage $T \gg T_*$, during which the bare potential can be omitted in the high-temperature environment. In Appendix. A, we solve the scalar evolution for this situation. Because $\phi - \phi_{\min}$ is the linear combination of $T^{\frac{1\pm\sqrt{1-\eta^2}}{2}}$, to describe the thermal convergence more quantitatively, we need the specific value of η. We recall that the potential minimums are $\phi_{\min} = \pi f/2$ for the type-A model and $\phi_{\min} = 0, \pm\pi f$ for the

type-B model. Given the initial condition $\dot{\phi}_{\rm rh} \simeq 0$, we approximately have

$$\phi - \phi_{\rm min} \propto \begin{cases} T^{\frac{1-\sqrt{1-\eta^2}}{2}} & (\eta \leq 1) \\ T^{\frac{1}{2}} \cos\left[\sqrt{\eta^2-1}\log\left(T/T_{\rm rh}\right)/2\right] & (\eta > 1) \end{cases}, \tag{30}$$

where $\eta = 1$ is the critical value determining how ϕ evolves towards the local minimum.

If $\eta \leq 1$ (but not too small), ϕ gradually slides to $\phi_{\rm min}$, as shown in the green lines in the left and right panels of Fig. 4. Incidentally, in the limit $\eta \ll 1$, we come back to Eq. (24) where ϕ is nearly frozen at the early universe, which is related to the blue lines in both panels of Fig. 4. Here, the $T^{\frac{1+\sqrt{1-\eta^2}}{2}}$ term is negligible because it describes the movement with non-zero $\dot{\phi}_{\rm rh}$. If $\eta > 1$, ϕ's movement towards $\phi_{\rm min}$ is oscillating because $T^{\frac{1\pm i\sqrt{\eta^2-1}}{2}} = T^{1/2}e^{\pm i\sqrt{\eta^2-1}\log T/2}$. Obeying the power law $T^{1/2}$, ϕ's oscillation amplitude decreases as the temperature goes down. This can be explained more intuitively: When $T \gtrsim m_e$, the adiabatic condition of the WKB approximation is satisfied ($\dot{m}_T/m_T^2 \sim 1/\eta \lesssim 1$), so there is no particle creation or depletion for ϕ, or equivalently speaking, its number density is conserved. For this reason, ϕ's oscillation amplitude obeys $|\phi - \phi_{\rm min}| \simeq \sqrt{2n_\phi/m_T} \propto T^{\frac{1}{2}}$. Eq. (30) reveals an interesting phenomenon: As long as there is a hierarchy between $T_{\rm rh}$ and m_e, which is natural in most of the inflation models, ϕ converges to the local minimum of the thermal potential. For example, in $\eta \gtrsim 1$ case, given that $T_{\rm rh} \sim 1{\rm TeV}$, when the universe temperature drops to $T \sim m_e$, the field deviation from the local minimum becomes $|\phi - \phi_{\rm min}|/\phi_{\rm min} \sim 10^{-3}$. Higher $T_{\rm rh}$ leads to even smaller field displacement from the thermal minimum. Such determination of scalar's misalignment through the thermal effect is named the thermal misalignment in several recent works [102, 135, 136]. Other mechanisms setting scalar's nonzero initial displacement can be found in [137–139]. As shown in Eq. (23), in our paper, we use the term thermal misalignment for the cases satisfying $\eta \gtrsim 1$ to distinguish them from the standard misalignment in which the thermal effect does not play a role. We use such a definition because when this condition is satisfied, the thermal effect from the SM bath washes out ϕ's sensitivity of the initial condition and dynamically sets the field displacement.

When $T \lesssim T_*$, the bare potential becomes important in ϕ's evolution. In the $m_0 \lesssim H_Q$ case, the ultralight scalar's evolution is simply the combination of the early time wrong vacuum damped oscillation and the late-time true vacuum damped oscillation around zero with

$$T_{\rm osc} \simeq T|_{3H=m_0}, \quad |\phi|_{\rm osc} \simeq |\phi_{\rm min}|, \tag{31}$$

where $\phi_{\rm min} = \pi f/2$ for the type-A model and $\phi_{\rm min} = \pm\pi f$ for the type-B model with ϕ initially in the wrong vacuum. We do not put more words on that because this kind of the thermal misalignment can be treated as the standard misalignment with the thermally determined initial condition. Now, we shift our focus to the $m_0 \gtrsim H_Q$ case in the rest of this section. Since the total potentials of the type-A and type-B models have different shapes depending on exactness of the $\mathbb{Z}_2$ symmetry, and the scalar evolution depends on the numerical value of η, let us describe the scalar evolution case by case:

- **Type-A, $\eta \gg 1$.**

  When $T \gg T_*$, ϕ does the damped oscillation, which converges to $\pi f/2$. Afterward, when $T \sim T_*$, or equivalently speaking, $m_T \sim m_0$, the potential minimum begins to shift towards from $\pi f/2$ to 0, obeying $\phi = f \arctan\left(m_T^2/m_0^2\right)$ as shown in Eq. (19). When the universe temperature is much higher than m_e, the adiabatic condition is satisfied because $\dot{m}_T/m_T^2 \sim 1/\eta \ll 1$. We show the movement of ϕ in the lower left panel of Fig. 3 and the red line in the left panel of Fig. 4. However, as the temperature drops below m_e, because $\dot{m}_T/m_T^2 \sim e^{m_e/T}/\eta \gg 1$, ϕ is not able to respond to the sudden variation of the potential minimum anymore and begins the oscillation. Here, the oscillation temperature and the starting amplitude can be written as

$$T_{\rm osc} \sim T_Q, \quad |\phi|_{\rm osc} \sim f\left(T_Q/T_*\right)^4, \tag{32}$$

  where $T_Q \sim m_e/\log\eta$ as defined in Eq. (29). Given $f \ll m_{\rm pl}$, the hierarchy between T_* and T_Q strongly suppresses ϕ's late-time oscillation amplitude, leading to ϕ's minuscule relic abundance. Even though this phase does not appear in the following context of the dark photon dark matter freeze-in in Sec. IV, we still discuss

this phase in this section for completeness.

- **Type-A, $\eta \sim 1$.**

In the early time when $T \gg T|_{3H=m_0}$, ϕ slides to the thermal minimum $\pi f/2$. When $T \sim T|_{3H=m_0}$, the scalar begins the late-time damped oscillation obeying $|\phi| \propto T^{3/2}$ with the starting temperature and amplitude

$$T_{\rm osc} \sim T|_{3H=m_0}, \quad |\phi|_{\rm osc} \simeq \pi f/2. \tag{33}$$

In Fig. 3, we do not list such a case because, even though categorized as the thermal misalignment, it can be decomposed into the standard misalignment (upper left panel of Fig. 3) plus the determined initial amplitude. In the left panel of Fig. 4, the green line describes such situation: When $\widetilde{T} \gtrsim 1$, the green line gradually slides to the $\pi f/2$. When $\widetilde{T} \sim 1$, the green line begins the damped oscillation with the amplitude scaled as $|\phi| \propto \widetilde{T}^{3/2}$.

- **Type-B, $\eta \gtrsim 1$.**

Unlike the type-A model, there is no continuous shift of the potential minimum during the cosmological evolution. Therefore, we only need to focus on the moment when the local minimum flips. Here, we mainly focus on the case in which ϕ's initial condition satisfies $\pi f/2 \lesssim \phi_{\rm rh} \lesssim 3\pi f/2$. In this case, because of the thermal effect when $T \gg T_*$, ϕ converges to the local minimum πf inside the wrong vacuum. When $T \lesssim T_*$, at the point $\phi = \pi f$, the second order derivative becomes nonpositive, i.e., $V''|_{\phi=\pi f} \lesssim 0$, thereafter ϕ begins the oscillation around zero. From Eq. (22), we have

$$T_{\rm osc} \simeq T_*, \quad |\phi|_{\rm osc} \simeq \pi f. \tag{34}$$

According to Eq. (22), we recall that $T_* \sim T|_{3H=m_0}/\eta^{1/2} \sim (m_0 m_{\rm pl}/\eta)^{1/2}$ when $m_0 \gtrsim \eta H_Q$, and $T_* \sim 0.1 m_e$ when $H_Q \lesssim m_0 \lesssim \eta H_Q$.

For the $\eta \gg 1$ case, one could look at the red line in the right panel of Fig. 4. Here, ϕ oscillates around the thermal minimum πf with the power law $|\phi - \pi f| \propto T^{1/2}$ when $T \gg T_*$. Afterward, when $T \simeq T_*$, alternatively speaking, $m_T \simeq m_0$, ϕ begins the oscillation following $|\phi| \propto T^{3/2}$. The plot shows the apparent postponement of the scalar oscillation for the red line compared with the other two lines. Because the CP-even scalar ϕ's oscillation is postponed, the evolution of ϕ can be classified as the trapped misalignment, which is formally investigated in axion models [140, 141]. In this case, ϕ's relic abundance is enhanced given the same $|\phi|_{\rm osc}$ or f. We can also think about such characteristics inversely: For ϕ to reach the same abundance quantified by $\mathcal{F}$, one only needs smaller $|\phi|_{\rm osc}$ or f. To be more quantitative, one can write the misalignment at the beginning of the oscillation as

$$|\phi|_{\rm osc} \simeq |\phi|_{\rm osc, std} \left(T_*/T|_{3H=m_0}\right)^{3/2}, \tag{35}$$

where $|\phi|_{\rm osc,std}$ denotes the starting amplitude for the standard misalignment as shown in Eq. (27). From Eq. (35), one can see that the necessary early misalignment $|\phi|_{\rm osc}$ is rescaled by a factor of $(T_*/T|_{3H=m_0})^{3/2}$, which shows that $|\phi|_{\rm osc}$ is much smaller compared with $|\phi|_{\rm osc,std}$ when $\mathcal{F}$ is determined.

For the $\eta \sim 1$ case, one could refer to the green line in the right panel of Fig. 4. In the early stage, i.e., $T \gtrsim T|_{3H=m_0}$, ϕ slowly moves to πf obeying $|\phi - \pi f| \propto T^{\frac{1-\sqrt{1-\eta^2}}{2}}$. When $T \simeq T|_{3H=m_0}$, ϕ begins the damped oscillation with the power law $|\phi| \propto T^{3/2}$. From the discussion above, we can find that the $\eta \sim 1$ case has the thermal determination of the initial condition but does not have the postponement of the oscillation. Therefore, ϕ is in the phase of the thermal misalignment but not in the phase of the trapped misalignment.

Finally, let us briefly discuss the case where $-\pi f/2 \lesssim \phi_{\rm rh} \lesssim \pi f/2$. Here we have that ϕ oscillates obeying $|\phi| \propto T^{1/2}$ when $T \gg T_*$, and then oscillates obeying $|\phi| \propto T^{3/2}$ when $T \lesssim T_*$. Because the late-time amplitude is suppressed by a factor of $(T_{\rm rh}/T_*)^{1/2}$, given the nonnegligible fraction of ϕ among the dark matter (For example, $\mathcal{F} \sim 10^{-3}$), f depends on $T_{\rm rh}$ and may be larger than $m_{\rm pl}$. Therefore, this paper focuses on the case where ϕ is initially localized inside the wrong vacuum.

IV.   DARK PHOTON DARK MATTER

In this section, we discuss the freeze-in of the $keV - MeV$ dark photon dark matter via varying kinetic mixing. As shown in [58–60], the dark photon freeze-in through the time-independent kinetic mixing ($\epsilon_{FI} \sim 10^{-12}$) is entirely ruled out since it causes the strong excess in stellar energy loss, the CMB energy injection, and the galactic photon spectrum. Alternative dark photon dark matter production mechanisms include misalignment [120, 142–144][2], gravitational production [145–150], the radiation of the cosmic string network [151, 152], and axion tachyonic instability [153–157]. Realizing that all the production mechanisms mentioned above do not rely on kinetic mixing, which is indispensable for dark photon detection, we provide a minimal extension of the dark photon dark matter freeze-in where the ultralight scalar's evolution sets the experimental benchmark of kinetic mixing dynamically. In addition, we want to stress the enormous significance of detecting the ultralight scalar in the whole mass range, i.e., $10^{-33}\text{eV} \lesssim m_0 \ll \text{eV}$: Even though it cannot be the main component of dark matter in the mass range $10^{-33}\text{eV} \lesssim m_0 \lesssim 10^{-17}\text{eV}$, which is excluded by the fuzzy dark matter constraints [121–126, 134] and the superradiance constraints from the supermassive black holes [158–161], such tiny amount of the ultralight scalar relic can still open the gate for the main component dark matter's production.

At the beginning of this section, let us give a brief introduction of the setup: In our model, the dark photon dark matter is produced through the operator $\mathcal{L} \supset \phi F_{\mu\nu} F'^{\mu\nu}/2\Lambda_{KM}$ whose effective kinetic mixing is supported by ϕ's VEV in the early universe. Thereafter, when $T \simeq T_{osc}$, ϕ begins the oscillation with its amplitude scaled as $|\phi| \propto (T/T_{osc})^{3/2}$. Because most of the existing constraints are imposed when $T \ll T_{osc}$, the dark photon's parameter space can be vastly extended, and the ratio T_0/T_{osc} determines today's local kinetic mixing for the future dark photon dark matter detections. In addition, since the ϕF^2 or $\phi^2 F^2$ operator is induced as the byproduct of the varying kinetic mixing from the UV theory discussed in Sec. II, testing the fine-structure constant variation and the equivalence principle violation through the ground-based experiments (torsion balance, clock comparison, resonant-mass detector, AION, MAGIS) [83, 84, 87–91, 162–166], satellite-based experiments (MICROSCOPE, Space-Q, AEDGE) [85, 167–169], astrophysics (PTA, SKA) [92, 170], and cosmology (CMB, BBN, Lyman-α forest) [93–96, 170] open another brand new window for the dark matter experimentalists.

A.   Dark Photon Production

Let us begin with the dark photon freeze-in through the varying kinetic mixing. To simplify the discussion, we focus on the case where the dark photon is produced before the ultralight scalar's oscillation. When $T \gtrsim T_{osc}$, ϕ is frozen with the nonzero displacement such that the dark photon is produced through $\gamma \to A'$ and $e^- e^+ \to A'$ channels. Our numerical calculation of the required kinetic mixing to reach today's dark matter relic abundance is shown as the yellow line labeled as "ϵ_{FI}" in Fig. 5. In the following text, let us briefly introduce how to estimate the dark photon abundance from the freeze-in process semianalytically.

In the case where $m_{A'} < 2m_e$, we solve the Boltzmann equation[3]

$$\dot{n}_{A'} + 3Hn_{A'} \simeq n_\gamma \langle \Gamma_{\gamma \to A'} \rangle, \quad \text{where} \quad \langle \Gamma_{\gamma \to A'} \rangle \sim \frac{\epsilon^2 m_{A'}^4}{T} \delta(m_\gamma^2 - m_{A'}^2). \tag{36}$$

In Eq. (36), n_γ and $n_{A'}$ are the number density of the photon and dark photon, respectively. $\langle \Gamma_{\gamma \to A'} \rangle$ is the thermal average of the photon to dark photon transition rate, from which we know that the resonant oscillation, i.e., $\gamma \to A'$, happens when $m_\gamma \simeq m_{A'}$. In the mass range $0.1\text{MeV} \lesssim m_{A'} \lesssim 1\text{MeV}$, when $\gamma \to A'$ happens, $e^\pm$ are relativistic. Therefore, the plasmon mass can be approximately written as $m_\gamma^2 \simeq 2\pi\alpha_{em}T^2/3$. Combining m_γ^2 and Eq. (36), we have

$$T_{\gamma \to A'} \sim 8m_{A'}, \quad \Omega_{A', \gamma \to A'} \sim \epsilon^2 \alpha_{em}^{3/2} \frac{m_{pl}}{T_{eq}}, \tag{37}$$

---

[2] The minimal vector field misalignment model [142] is not viable because the inflationary e-folds exponentially suppresses the vector field displacement. To avoid such washout, the non-minimum coupling with the gravity or the modified kinetic term is needed [120, 143, 144].

[3] Even though essential in the indirect detection discussed later, the decay channels such as $A' \to e^- e^+$ and $A' \to 3\gamma$ nearly do not affect A''s abundance. This is because, in the experimentally allowed region, the dark photon decay rate is much smaller than the universe's expansion rate, not to mention the suppressed late-time kinetic mixing compared with the mixing in the early universe.

Dark Photon Dark Matter: Constant Kinetic Mixing
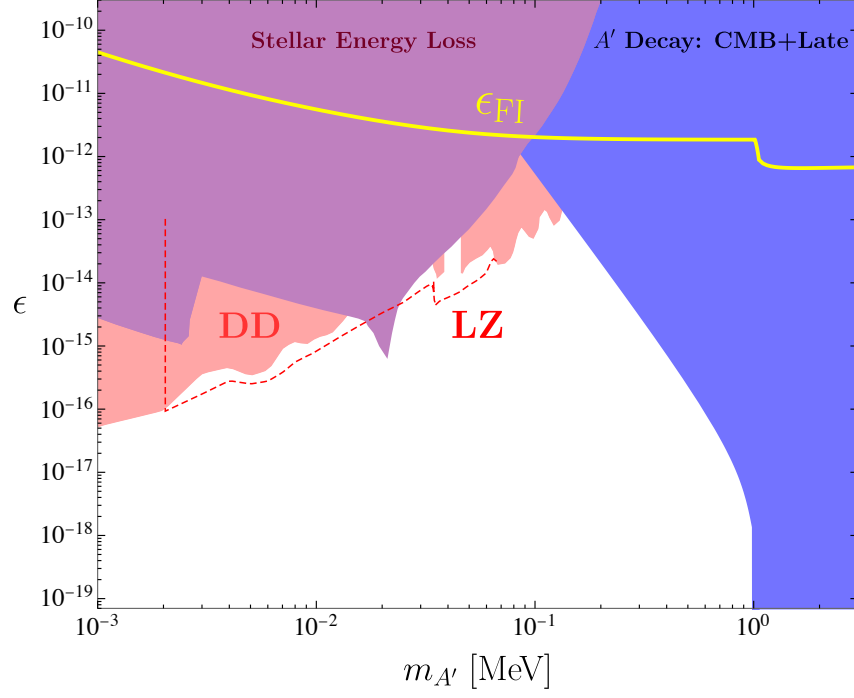

Figure 5. The parameter space of the dark photon dark matter ($\Omega_{A'}h^2 \simeq 0.12$) with the constant kinetic mixing. Here, $m_{A'}$ is the dark photon mass, and ϵ is the constant kinetic mixing. The yellow line labeled with "$\epsilon_{\rm FI}$" is the dark photon freeze-in line, i.e., the kinetic mixing necessary for the dark photon to reach today's dark matter relic abundance. In the mass range $m_{A'} < 2m_e$, the dominant dark photon production channel is photon to dark photon resonant conversion, i.e., $\gamma \to A'$. When $m_{A'} \geq 2m_e$, $A' \to e^- e^+$ dominates, which explains the slight decreasing of the freeze-in line. In the plot, the purple region represents the constraints from the stellar energy loss of red giants, horizontal branches, and sun [58–60, 71–74]. The shaded red region labeled by "DD" denotes the constraints from the dark matter direct detection experiments [60, 75–80]. Up to now, the most stringent constraint within keV − MeV range comes from the XENONnT experiment [80]. The dashed red line is the projection of the next-generation LUX-ZEPLIN (LZ) experiment [171]. The blue region denotes the constraints from the dark photon dark matter decay, whose dominant channel is $A' \to 3\gamma$ when $m_{A'} < 2m_e$, or $A' \to e^- e^+$ when $m_{A'} \geq 2m_e$. Since the dark photon decay affects CMB and the late-time photon spectrum, constraints can be imposed on the dark photon parameter space [58–60, 172]. From [60, 82, 173], we know that the constraints from CMB and the late-time processes are comparable for the constant kinetic mixing model. Therefore, we label the constraint from the dark photon decay with "CMB+Late". In the plot, one can find that the freeze-in line is covered by the imposed constraints, which means that the constant kinetic mixing model is completely ruled out. Such exclusion of the dark photon dark matter freeze-in is formally discussed in [58–60].

where $T_{\gamma \to A'}$ is the resonant temperature of $\gamma \to A'$, $T_{\rm eq} \sim$ eV is the temperature of the matter-radiation equality, and $\Omega_{A', \gamma \to A'}$ is the related dark photon relic abundance. In Eq. (37), $\Omega_{A'}$'s dependence on $m_{A'}$ is approximately canceled out. Therefore, the freeze-in line in the region where $m_{A'} < 2m_e$ is approximately a constant. Since $\Omega_{A'}h^2 \simeq 0.12$, from Eq. (37) we have

$$\epsilon_{\rm FI} \sim 10^{-12}, \tag{38}$$

which explains the behavior of the yellow line in Fig. 5 in the mass range $0.1{\rm MeV} \lesssim m_{A'} \lesssim 1{\rm MeV}$. In the mass range $m_{A'} \lesssim 0.1{\rm MeV}$, the resonant oscillation happens when $e^\pm$ are non-relativistic. To be more quantitative, $T_{\rm res} \sim 0.1m_e$, which is insensitive to $m_{A'}$. In this case, we have $\Omega_{A'} \propto \epsilon^2 m_{A'}^3$, which explains the slope of the freeze-in line in Fig. 5 in this mass range. In the discussion above, we focus on the transverse dark photon because the produced longitudinal dark photon is subdominant, which is checked by us numerically and consistent with [72].

In the case where $m_{A'} \gtrsim 2m_e$, the inverse decay channel, i.e., $e^- e^+ \to A'$, opens up and dominates over $\gamma \to A'$.

Now the Boltzmann equation can be written as

$$\dot{n}_{A'} + 3H n_{A'} \simeq n_{e^-} n_{e^+} \langle \sigma_{e^- e^+ \to A'} \rangle, \quad \text{where } n_{e^-} n_{e^+} \langle \sigma_{e^- e^+ \to A'} \rangle \sim \epsilon^2 \alpha_{\text{em}} m_{A'}^{5/2} T^{3/2} e^{-m_{A'}/T}. \tag{39}$$

Inside the collision term of Eq. (39), there is an exponential suppression factor $e^{-m_{A'}/T}$ cutting off the dark photon production when the universe cools down. From Eq. (39), we estimate the cut-off temperature of $e^- e^+ \to A'$ near which most of the dark photons are produced and the related dark photon relic abundance as

$$T_{e^- e^+ \to A'} \sim m_{A'}, \qquad \Omega_{A', e^- e^+ \to A'} \sim \epsilon^2 \alpha_{\text{em}} \frac{m_{\text{pl}}}{T_{\text{eq}}}, \tag{40}$$

respectively. In Eq. (40), one can find that $\Omega_{A', e^- e^+ \to A'}$ is also almost independent of the dark photon mass, which is similar to the result in Eq. (37) but different by an $\alpha_{\text{em}}^{1/2}$ factor. For this reason, in the mass range $m_{A'} \gtrsim 2 m_e$, the needed kinetic mixing to reach today's relic abundance is slightly smaller than the one in the range $m_{A'} < 2 m_e$ by an $\mathcal{O}(1)$ factor, which explains the slight lowering of the freeze-in lines in Fig. 5 and Fig. 6.

Being different from the model with the constant kinetic mixing, our model has extra dark photon production channels where ϕ is the particle rather than the VEV, such as $\gamma \to A'\phi$ and $e^- e^+ \to A'\phi$. Nevertheless, one can see that these channels are subdominant from the discussion below. By estimating the ratio of the A' abundance produced through these channels over the A' abundance produced through the varying kinetic mixing, we have

$$\frac{\Omega_{\gamma \to A'\phi}}{\Omega_{\gamma \to A'}} \sim \frac{m_{A'} T_{\text{rh}}}{|\phi|_{\text{osc}}^2} \ll 1, \tag{41}$$

where $\Omega_{\gamma \to A'}$ represents the dark photon abundance from the channels in which ϕ serves as the VEV, and $\Omega_{\gamma \to A'\phi}$ is for the dark photon abundance from the channels where ϕ is the particle. From Eq. (41), one can find that the majority of the dark photon comes from the channels with the ϕ as the VEV, because the channels with ϕ as the particle are highly suppressed by the large Λ_{KM}, while the channels with the ϕ as the VEV are compensated with large $|\phi|_{\text{osc}}$.

B. Signatures and Constraints

In our model, the experiments can be categorized into two classes: 1. The detections of the dark photon dark matter. These rely on the portal between the visible and dark sectors, i.e., the varying kinetic mixing through which the energy and momentum flow. Today's local kinetic mixing is set by the scalar mass m_0. 2. The detection of the ultralight scalar ϕ, i.e., the handle controlling the portal. Such detections are based upon the scalar-photon couplings, which vary the fine-structure constant or violate the equivalence principle. The targets for the experiments detecting the ultralight CP-even scalar are set by the dark photon dark matter freeze-in.

1. Detection of the Dark Photon Dark Matter

Let us first investigate the phenomenology of the dark photon dark matter established on the nonzero kinetic mixing. Before starting the discussion, one needs to recall that in our model, the kinetic mixing varies during the universe's evolution. Hence, the experimental detectability based on some specific process depends on the universe's epoch when this process happens. To understand this, we start by reviewing the ultralight scalar's evolution. As we know, when $T \gtrsim T_{\text{osc}}$, ϕ is at rest with the nonzero field displacement. Afterward, when $T \lesssim T_{\text{osc}}$, ϕ begins the damped oscillation scaled as $|\phi| \propto T^{3/2}$. Given that the dark photon is the main component of dark matter, we have $\epsilon_{\text{FI}} \sim 10^{-12}$, based on which today's local kinetic mixing, denoted as ϵ_0, is set by T_{osc}. From Sec. III, we write ϵ_0 as

$$\epsilon_0 \sim \epsilon_{\text{FI}} \left(\frac{T_0}{T_{\text{osc}}} \right)^{3/2} \times \begin{cases} 1 & (m_0 \ll 10^{-25}\text{eV}) \\ \mathcal{E} & (m_0 \gtrsim 10^{-25}\text{eV}) \end{cases}, \tag{42}$$
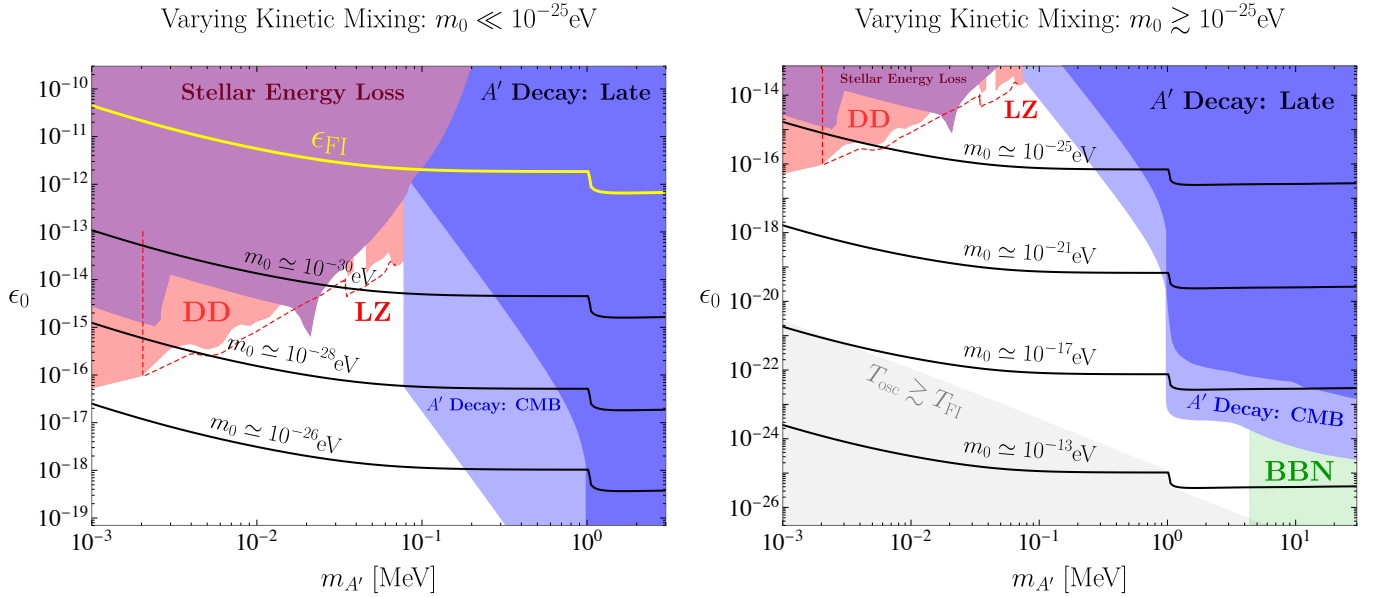
Figure 6. The parameter space of the dark photon dark matter ($\Omega_{A'}h^2 \simeq 0.12$) produced from the freeze-in mechanism through the varying kinetic mixing. Here, $m_{A'}$ is the dark photon mass, and ϵ_0 is today's local kinetic mixing near the earth. One should note that the CMB (light blue) and BBN (green) bounds are imposed on the early universe with larger kinetic mixing. Based on the evolution of ϕ, we recast these constraints to the $m_{A'} - \epsilon_0$ plane. **Left**: $m_0 \ll 10^{-25}$eV. In the plot, we choose $m_0 \simeq 10^{-30}, 10^{-28}, 10^{-26}$ eV as the benchmark values. Here, the strongest constraints come from the stellar energy loss (purple), A' decay during CMB (light blue) and the late time (dark blue), and the direct detection experiments (red). The dashed red line denotes the projection of LUX-ZEPLIN (LZ). The yellow line labeled by "$\epsilon_{\rm FI}$" is the kinetic mixing required to reach the dark matter relic abundance during the freeze-in. If $m_0 \lesssim 10^{-28}$eV, one has $T_{\rm osc} \lesssim T_{\rm CMB}$, so $\epsilon_{\rm CMB} \simeq \epsilon_{\rm FI}$. For this reason, the dark photon heavier than 0.1MeV is excluded, while the lighter one is not. **Right**: $m_0 \gtrsim 10^{-25}$eV. Here we choose $m_0 \simeq 10^{-25}, 10^{-21}, 10^{-17}, 10^{-13}$ eV as the benchmark values. The light gray region denotes the parameter space where our calculation breaks up when the oscillation begins before the freeze-in process, i.e., $T_{\rm osc} \gtrsim T_{\rm FI}$. Here, the most relevant constraints comes from the A' decay during CMB (light blue) and the late time (dark blue), where $A' \to 3\gamma$ dominates when $m_{A'} < 2m_e$, and $A' \to e^- e^+$ dominates when $m_{A'} \gtrsim 2m_e$. Since the kinetic mixing is large during the BBN, the dark photon decay is also constrained by BBN (green). One should notice that the BBN bound is cut off at $m_{A'} \simeq 5$ MeV, below which the A' decay cannot disintegrate the relevant light elements [174, 175]. Since the oscillation temperatures for the type-A and the type-B model have some slight quantitative differences in the mass range $m_0 \gtrsim 10^{-18}$eV, here we mainly use the type-A model as an example.

where the universe temperature today is $T_0 \sim 10^{-3}$eV, the enhancement factor from the structure formation is $\mathcal{E} \sim 600$, as shown in Eq. (28), and the kinetic mixing during the freeze-in is $\epsilon_{\rm FI} \sim 10^{-12}$, as shown in Eq. (38). Based upon Eq. (42), we divide the discussion into two parts separately, as shown in Fig. 6: The left panel denoting the case $m_0 \ll 10^{-25}$eV where $\rho_{\phi,\,\rm local} \simeq \mathcal{F}\rho_{\rm average}$, and the right panel representing the case $m_0 \gtrsim 10^{-25}$eV where $\rho_{\phi,\,\rm local} \simeq \mathcal{F}\rho_{\rm local}$.

Let us begin with the $m_0 \ll 10^{-25}$eV case with the dark photon parameter space shown in the left panel of Fig. 6. One can see that the most relevant constraints come from the dark matter direct detection (red), the stellar energy loss (purple), and the dark photon decay during the CMB (light blue) and the late time (blue). In the plot, the yellow line represents the required kinetic mixing during the dark photon freeze-in to reach the relic abundance $\Omega_{A'}h^2 \simeq 0.12$, from which one can easily find that the constant kinetic mixing scenario is thoroughly excluded. In contrast, the varying kinetic mixing model opens the parameter space and provides the benchmark values determined by m_0. Here, we choose $m_0 \simeq 10^{-30}, 10^{-28}, 10^{-26}$ eV to plot the freeze-in lines on the $m_{A'} - \epsilon_0$ plane. Since $T_{\rm osc} \sim (m_0 m_{\rm pl})^{1/2}$, larger m_0 leads to an earlier start of the oscillation, such that ϵ_0 is smaller. Let us briefly introduce the constraints appearing in the left panel of Fig. 6 in the following paragraphs.

In the mass range $m_{A'} \lesssim 0.1$MeV, the most relevant constraints come from the dark matter direction (red) and the stellar energy loss (purple). The direct detection experiments test scintillation photons from the electron recoil inside the noble liquids or semiconductors due to the absorption of the dark photon [60, 75–80]. Up to now, the most strict constraint within keV to MeV mass range comes from the XENONnT experiment [80]. The LUX-ZEPLIN (LZ)

experiment, represented by the dashed red line in the plot, can test smaller kinetic mixing by a half to one order of magnitude [171]. Furthermore, we can expect that future dark matter direct detection experiments, such as DarkSide-20k [176] and DARWIN [177], with more giant detectors and lower backgrounds, can have better detection capability. In this mass range, our model is also constrained by the stellar energy loss of the sun, horizontal branch, and red giant via the channel $\gamma \to A'$, which changes the stellar evolutions [58–60, 71–74]. The direct detection of the non-relativistic dark photons produced by the sun, known as the solar basin, can also impose comparable constraints [178].

In the mass range $m_{A'} \gtrsim 0.1\text{MeV}$, our model is constrained by the decay of the dark photon dark matter. When $m_{A'} < 2m_e$, since the two-photon channel is forbidden according to the Landau-Yang theorem [179, 180], the dark photon decays through $A' \to 3\gamma$ induced by the electron loop. When $m_{A'} \gtrsim 2m_e$, the dominant channel is $A' \to e^- e^+$. These two channels are constrained by the observations of the CMB and the late-time photon background, which give comparable constraints in the constant kinetic mixing scenario. From [59, 60, 81, 82], we know that $\Gamma_{A' \to 3\gamma} \lesssim 10^{-9} H_0$ and $\Gamma_{A' \to e^- e^+} \lesssim 10^{-7} H_0$ for $m_{A'} \sim \text{MeV}$. However, in our model, one should realize that these two physical processes happen in different stages of the universe. To be more specific, the stage of CMB is at $T_{\text{CMB}} \sim \text{eV}$ while the galactic photon is emitted in today's universe. From the discussion of ϕ's evolution in Sec. III, we know that the kinetic mixing during CMB is

$$\epsilon_{\text{CMB}} \sim \epsilon_0 \times \left[\frac{\min(T_{\text{CMB}}, T_{\text{osc}})}{T_0} \right]^{3/2}, \tag{43}$$

where $T_{\text{osc}} \sim (m_0 m_{\text{pl}})^{1/2}$. Based on Eq. (43), we can recast the constraint on the kinetic mixing from the dark photon dark matter decay during the CMB stage to the $m_{A'} - \epsilon_0$ diagram. When $m_0 \lesssim 10^{-28}\text{eV}$, one knows $T_{\text{osc}} \lesssim T_{\text{CMB}}$, so $\epsilon_{\text{CMB}} \simeq \epsilon_{\text{FI}}$. Given this, one can figure out that the dark photon mass region $m_{A'} \gtrsim 0.1\text{MeV}$ is excluded by CMB, while the smaller dark photon mass region is not. This explains CMB bound's cutting off at $m_{A'} \simeq 0.1\text{MeV}$ in the left panel of Fig. 6. When $m_0 \gtrsim 10^{-28}\text{eV}$, one has $T_{\text{osc}} \gtrsim T_{\text{CMB}}$, so the kinetic mixing during the stage of CMB is $\epsilon_{\text{CMB}} \sim \epsilon_0 (T_{\text{CMB}}/T_0)^{3/2}$, which explains the strengthening of the CMB bound at the range $m_{A'} \gtrsim 0.1\text{MeV}$ compared with the constraints from the late-time photon.

Now let us discuss the $m_0 \gtrsim 10^{-25}\text{eV}$ case appearing on the right panel of Fig. 6. Here, the most relevant constraints come from the decay of the dark photon dark matter during CMB (light blue) and BBN (green). To recast the constraints in the early universe to the $m_{A'} - \epsilon_0$ plane, we use the formula

$$\epsilon_{\text{CMB}} \sim \epsilon_0 \times \left[\frac{T_{\text{CMB}}}{T_0} \right]^{3/2} \frac{1}{\mathcal{E}}, \qquad \epsilon_{\text{BBN}} \sim \epsilon_0 \times \left[\frac{\min(T_{\text{BBN}}, T_{\text{osc}})}{T_0} \right]^{3/2} \frac{1}{\mathcal{E}}. \tag{44}$$

From the discussion in Subsec. III B, we know that thermal effect may change T_{osc} for the type-B model when the scalar is heavier than $10^{-16}/\log^2 \eta \, \text{eV}$. Even though the type-B model does not cause the qualitative differences, to simplify the discussion, we only discuss the type-A model as an example such that the oscillation temperature still satisfies $T_{\text{osc}} \sim (m_0 m_{\text{pl}})^{1/2}$ in the experimentally allowed region. Similar to the discussion above, we recast the CMB bound to the $m_{A'} - \epsilon_0$ plot. During the BBN, ϵ_{BBN} ranges from 10^{-12} to 10^{-14}, which depends on the concrete value of m_0. In this range, the dark photon decay through $A' \to e^- e^+$ leads to the light elements' disintegration, based on which the BBN constraint is imposed [174, 175]. However, as long as $m_{A'} \lesssim 5\text{MeV}$, the dark photon decay cannot change the light element abundance since the injected energy is smaller than the deuterium binding energy, which is the smallest among all the relevant light elements (except ^7Be whose abundance does not affect the main BBN observables). In the right panel of Fig. 6, there is a gray region in the lower left corner, which represents the parameter space where the calculations of freeze-in lines break because the freeze-in happens after the start of the oscillation. At the end of this paragraph, we point out one nontrivial character: Through the varying kinetic mixing, the dark photon heavier than 1MeV can be produced and avoid the constraints of the decay $A' \to e^- e^+$ because the kinetic mixing portal fastly closes right after the dark photon production.

Before ending this subsection, we want to point out that since the dark photon is produced through $\gamma \to A'$ with the initial momentum $p_{A'} \sim T$, it washes out the dark matter substructure in the late universe, which is the character of the warm dark matter [181–184]. To avoid this, we need $m_{A'} \gtrsim \text{few} \times 10\,\text{keV}$. Since imposing such constraints needs detailed analyses based on the dark matter phase space distribution, which deviates from the main point of this paper, we leave this to future work.
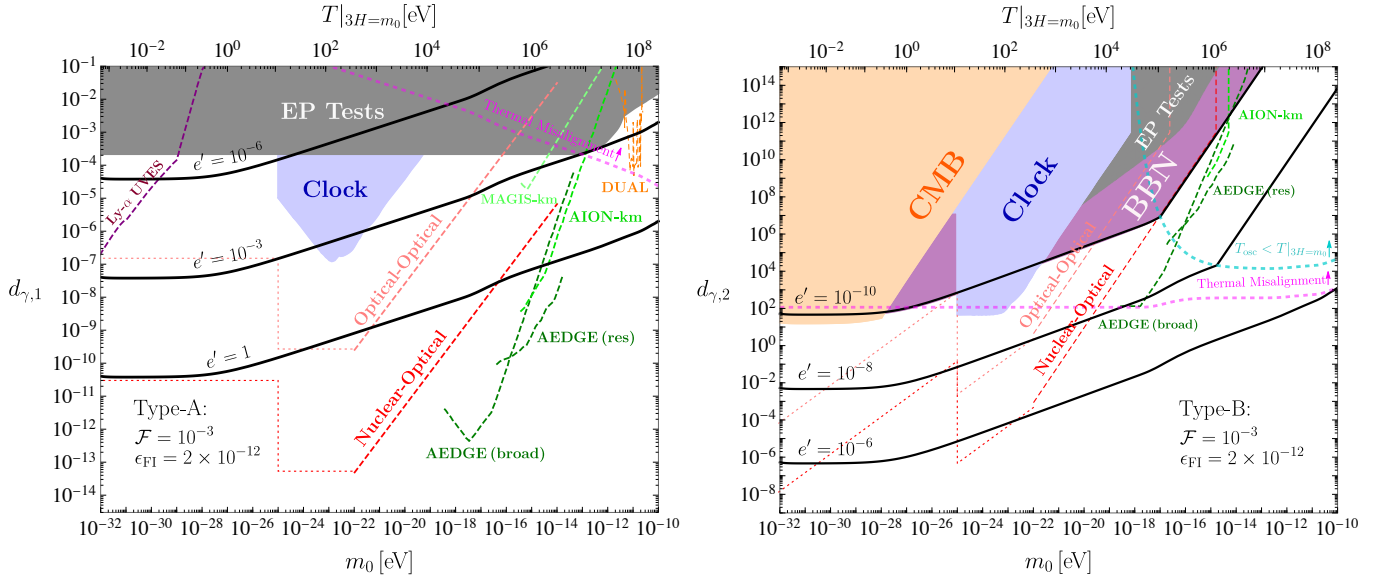
Figure 7. The parameter space of the scalar-photon couplings. The nonrelativistic scalar relic's fraction among the dark matter is $\mathcal{F} \simeq 10^{-3}$. The kinetic mixing before the oscillation is $\epsilon_{\mathrm{FI}} \simeq 2 \times 10^{-12}$, which is the benchmark value for the freeze-in production of the dark photon dark matter satisfying $\Omega_{A'} h^2 \simeq 0.12$. **Left**: The type-A model ($y' = 0$). We choose $e' = 1, 10^{-3}, 10^{-6}$ to demonstrate the experimental targets for the dark photon freeze-in through the varying kinetic mixing, which appear as the black lines. The thick dashed magenta line is the $\eta \simeq 1$ contour, upon which the scalar's early displacement is set to be $\pi f/2$ by the thermal misalignment. The gray region denotes the constraints from the equivalence principle tests (gray: EP tests) from the MICROSCOPE satellite [85] and the torsion balance experiments [83, 84]. The blue region represents current constraints from the clock comparisons [86–88, 90, 185]. We can see, for the type-A model, most of the model's parameter space ($e' \lesssim 1$) is inside the projections of the proposed experiments, such as Lyman-α UVES (dashed purple) [170], the clock comparison (dashed pink: optical-optical, dashed red: optical-nuclear) [86], the cold-atom interferometer (dashed dark green: AEDGE, dashed green: AION-km, dashed light green: MAGIS-km) [165, 166, 168, 186], and the resonant-mass oscillator (dashed orange: DUAL) [91]. **Right**: The type-B model ($y' = -y$) beginning with the wrong vacuum ($\pi f/2 \lesssim \phi_{\mathrm{rh}} \lesssim 3\pi f/2$). We choose $e' = 10^{-6}, 10^{-8}, 10^{-10}$ as the benchmark values to plot the black lines. The thick magenta line is the $\eta \simeq 1$ contour. In the region beyond such a magenta line, the scalar acquires the field displacement πf via the thermal misalignment. The thick dashed cyan line, i.e., the contour of $m_T|_{3H=m_0} \simeq m_0$, envelopes the region where the thermal effect postpones the oscillation starting, i.e., $T_{\mathrm{osc}} < T|_{3H=m_0}$. This is the region where the ultralight scalar does the trapped misalignment, which is previously investigated in [140, 141] for the axion models. Given the scalar abundance, since the trapped misalignment needs smaller oscillation amplitude, as discussed in Eq. (35), the power law of the black lines is changed within the upper right corner enveloped by the thick dashed cyan line. In the plot, one can find that the constraints from the cosmology (light orange: CMB, purple: BBN) are comparable with the current constraints from clock comparison experiments (blue) [86–88, 90, 162, 185] and the equivalence principle tests (gray: EP tests) [83–85]. For the type-B model, one needs $e' \lesssim 10^{-6}$ for the dark photon dark matter freeze-in to be detected by future experiments.

2. Detection of the Ultralight Scalar

From the former discussion in Sec. II, we know that the scalar-photon coupling appears along with the varying kinetic mixing from the UV physics, so our model can be tested from another entirely different perspective, i.e., the phenomenology of the ultralight CP-even scalar. Depending on whether the $\mathbb{Z}_2$ symmetry is exactly preserved or not, the scalar-photon coupling is ϕF^2 (Type-A), or $\phi^2 F^2$ (Type-B). From Eq. (16), we know that the dimensionless coefficients $d_{\gamma,i}$ ($i = 1, 2$) contain the production of the e' and Λ_{KM}, and Λ_{KM} can be written as $\Lambda_{\mathrm{KM}} \simeq |\phi|_{\mathrm{osc}}/\epsilon_{\mathrm{FI}}$. We also know that in the freeze-in model of the dark photon dark matter, there is $\epsilon_{\mathrm{FI}} \sim 10^{-12}$. Therefore, the targets of the scalar experiments are set by the freeze-in of the dark photon dark matter. To be more quantitative, we have

$$d_{\gamma,i} \sim \left(\frac{m_{\mathrm{pl}}\, \epsilon_{\mathrm{FI}}}{e'\, |\phi|_{\mathrm{osc}}} \right)^i \propto \left(\frac{m_0\, \epsilon_{\mathrm{FI}}}{e'\, \mathcal{F}^{1/2}\, T_{\mathrm{osc}}^{3/2}} \right)^i \qquad (i = 1, 2), \tag{45}$$

where "$i = 1$" and "$i = 2$" denote the type-A and type-B models, respectively. From Eq. (45), we know that with $\epsilon_{\rm FI}$ determined, the smaller e' is, the larger $d_{\gamma,i}$ ($i = 1, 2$) are, so our model can be more easily to be detected. The reason is that from the UV model in Sec. II, to maintain a determined kinetic mixing, $y^{(\prime)}$ should be turned up when e' is turned down. Therefore, the coefficients in front of the scalar-photon couplings are turned up. Since the phenomenologies for the linear (type-A) and quadratic (type-B) scalar-photon couplings are quite different, we discuss these two models individually in the rest of this subsection.

    a. **Type-A Model**   Let us first discuss the type-A model shown in the left panel of Fig. 7. To illustrate how the experimental signals vary with the dark gauge coupling, we plot the $d_{\gamma,1}$ lines (black) choosing $e' = 1, 10^{-3}, 10^{-6}$ as the benchmark values. From Eq. (25) we know that $T_{\rm osc} \propto m_0^{2/3}$ when $m_0 \lesssim 10^{-28}$eV, and $T_{\rm osc} \propto m_0^{1/2}$ when $m_0 \gtrsim 10^{-28}$eV. This explains the shapes of the black lines, which are represented as

$$d_{\gamma,1} \propto \frac{1}{e'\mathcal{F}^{1/2}} \times \begin{cases} m_0^{1/4} & (m_0 \gtrsim 10^{-28}\text{eV}) \\ \text{const} & (10^{-33}\text{eV} \lesssim m_0 \lesssim 10^{-28}\text{eV}) \end{cases} \tag{46}$$

In Fig. 7, the thick dashed magenta line is the contour of $\eta \simeq 1$. In the upper right corner beyond this contour, η is larger but still of the order of one to ten, so the "arctan" suppression in the type-A $\eta \gg 1$ case mentioned in Sec. III B does not appear. According to our former discussion in Sec. III B, for the type-A model with $\eta \sim 1$, the ultralight scalar's early field displacement is set to be $\pi f/2$ by the thermal misalignment. Since $|\phi|_{\rm osc}/f \sim \mathcal{O}(1)$, from Eq. (21) one can know the power law of the thick dashed magenta line satisfies $d_{\gamma,1} \propto m_0^{-1/4}$. In the region below this thick dashed magenta line, we have $\eta \ll 1$, so the ultralight scalar does the standard misalignment.

    One of the strongest constraints for the type-A model comes from the equivalence principle experiments testing the acceleration difference of two objects made by different materials attracted by the same heavy object. In the left panel of Fig. 7, such a constraint is shown as the shaded gray region. Until now, the most stringent constraint is imposed by the space mission named MICROSCOPE [85] and the torsion balance experiments named Eöt-Wash [83, 84], which gives $d_{\gamma,1} \lesssim 10^{-4}$. Since such acceleration difference is caused by the Yukawa interaction mediated by the ultralight scalar, these constraints are independent of the nonrelativistic scalar relic's fraction among the dark matter, i.e., $\mathcal{F}$. The clock comparisons of Dy/Dy [87], Rb/Cs [88], and Al$^+$/Hg$^+$ [90] also give stringent constraints based on testing the time-varying $\alpha_{\rm em}$. These constraints are shown as the shaded blue region.

    To go beyond the current constraints, there are several experiments proposed. For the future proposed clock comparison experiments [86], the projection of the improved optical-optical clock comparison is shown as the pink line, and the projection of the optical-nuclear clock comparison is shown as the red line. For these projections, the dashed parts denote the projection of the $\alpha_{\rm em}$ oscillation testing, and the dotted parts denote the projection of the $\alpha_{\rm em}$ drift testing. According to [86], the projection has the optimistic assumption that the measurement takes place when the scalar is swiping through the zero such that $\dot{\alpha}_{\rm em}$ is independent of m_0. Following this, we extrapolate the projections of the optical-optical and optical-nuclear experiments to 10^{-32}eV considering the homogeneity of the ultralight scalar when the scalar's de Broglie wavelength is much larger than the size of the Milky Way halo. The cold-atom interferometer experiments such as AEDGE [168], AION [165], and MAGIS [166] have strong detection capability in the mass range 10^{-19}eV $\lesssim m_0 \lesssim 10^{-12}$eV. In the plot, the projections of AEDGE (broadband, resonant mode), AION-km, and MAGIS-km are shown in the dashed dark green, dashed green, and dashed light green lines, respectively. The region of the thermal misalignment located in the upper right corner of the left panel of Fig. 7 can be tested by the proposed resonant-mass detectors, such as DUAL shown in the dashed orange line [91]. The CP-even scalar in the mass range 10^{-32}eV $\lesssim m_0 \lesssim 10^{-28}$eV can be tested via the proposed Lyman-α UVES observation [170] shown in the dashed purple line.

    Since all the constraints and projections except the EP tests rely on the $\alpha_{\rm em}$ variation, and $\Delta\alpha_{\rm em} \propto d_{\gamma,1}|\phi|$, they are all scaled by $\mathcal{F}^{-1/2}$ for different ultralight scalar fractions among the dark matter. We know from Eq. (46) that, as $\mathcal{F}$ varies, the relative position between the experimental targets (black lines) and the constraints/projections from the non-EP experiments keeps the same. Knowing that e' cannot be much larger than $\mathcal{O}(1)$ (Otherwise, the Landau pole is shifted to the low energy and the theory's perturbativity is broken), one can find from the left panel of Fig. 7 that most of the theory space is within the detection capabilities of the proposed experiments.

    b. **Type-B Model**   Now let us discuss the type-B model whose parameter space is shown in the right panel of Fig. 7. Here, we make ϕ to have the initial wrong vacuum ($\pi f/2 \lesssim \phi_{\rm rh} \lesssim 3\pi f/2$). In the plot, the thick dashed

magenta line is the contour obeying $\eta \simeq 1$. In the region upon (below) this line, the ultralight scalar does the thermal (standard) misalignment. From Eq. (21) we know that $\eta \sim (\alpha_{\rm em} d_{\gamma,2})^{1/2}$. Thus, the thick dashed magenta line approximately obeys $d_{\gamma,2} \sim 10^2$. As discussed in Subsec. III B, the thermal effect makes ϕ converge to πf in the early universe in the parameter space upon the thick dashed magenta line. The thick dashed cyan line denotes the contour satisfying $T_{\rm osc} \simeq T|_{3H=m_0}$, or equivalently speaking, $m_T|_{3H=m_0} \simeq m_0$. In the region enveloped by the thick dashed cyan line, we have $T_{\rm osc} < T|_{3H=m_0}$ meaning that the thermal effect postpones ϕ's oscillation, which represents the phase of trapped misalignment. From the plot, one can find that the thick dashed cyan line is approximately flat when $m_0 \gtrsim 10^{-16}$eV. Such flatness appears because $m_T \simeq m_0$ happens when $e^\pm$ are relativistic, which makes $m_T/H \sim \eta$. As long as $\eta \gg 1$, the starting of the oscillation is postponed by the thermal effect[4]. One can also find that the left side of the thick dashed cyan line becomes vertical, because $m_T \simeq m_0$ happens when $e^\pm$ are non-relativistic. In this case, the condition for $T_{\rm osc} < T|_{3H=m_0}$ becomes $m_0 \gtrsim m_e^2/m_{\rm pl}$.

The experimental benchmarks are shown as the black lines in $m_0 - d_{\gamma,2}$ plane. In the region of the standard misalignment ($\eta \ll 1$), the black lines obey

$$d_{\gamma,2} \propto \frac{1}{e'^2 \mathcal{F}} \times \begin{cases} m_0^{1/2} & (10^{-28}{\rm eV} \lesssim m_0 \lesssim m_*) \\ {\rm const} & (10^{-33}{\rm eV} \lesssim m_0 \lesssim 10^{-28}{\rm eV}) \end{cases}, \tag{47}$$

where m_* denotes the abscissa of the cross point of the black line and the thick dashed cyan line. To understand the power law of $d_{\gamma,2}$ in Eq. (47), one can refer to Eq. (25) which tells that $T_{\rm osc} \propto m_0^{2/3}$ when $m_0 \lesssim 10^{-28}$eV, and $T_{\rm osc} \propto m_0^{1/2}$ when $m_0 \gtrsim 10^{-28}$eV. After plugging $T_{\rm osc}$ into Eq. (45), one can have Eq. (47).

Now let us discuss the behaviors of the black lines in the scalar mass range $m_0 \gtrsim m_*$. If the black line intersects with the thick dashed cyan line on its vertical side, i.e., $m_* \lesssim 10^{-16}$eV, one can have $T_{\rm osc} \sim m_e$. If the black line crosses with the thick dashed cyan line on its horizontal side, i.e., $m_* \gtrsim 10^{-16}$eV, we have $T_{\rm osc} \sim T|_{3H=m_0}/\eta^{1/2} \propto m_0^{1/2}/d_{\gamma,2}^{1/4}$. Substituting the equations of $T_{\rm osc}$ into Eq. (45), we have

$$d_{\gamma,2} \propto \frac{1}{e'^2 \mathcal{F}} \times m_0^2 \quad {\rm if}\ m_* \lesssim 10^{-16}{\rm eV}, \qquad d_{\gamma,2} \propto \frac{1}{e'^8 \mathcal{F}^4} \times m_0^2 \quad {\rm if}\ m_* \gtrsim 10^{-16}{\rm eV} \quad (m_0 \gtrsim m_*), \tag{48}$$

which explains the black lines' tilting up when entering the region of the trapped misalignment, i.e., the area enclosed by the thick dashed cyan line. Such enhancement of the signal comes from the postponement of the oscillation which is the major feature of the trapped misalignment.

Similar to the type-A model, the type-B model can be tested through terrestrial experiments. In the plot, the current constraints based on clock comparison [87, 88, 90, 162, 163] are shown as the shaded blue region, and the constraints from the equivalence principle tests [85, 162, 163] are shown as the shaded gray region. The projections of the proposed optical-optical and optical-nuclear clock comparisons are shown in orange and red, respectively [86, 163]. Here, the dashed and dotted parts of the projections denote the detection capabilities of the $\alpha_{\rm em}$ oscillation and the $\alpha_{\rm em}$ drift, respectively. In addition, our model can also be tested by the cold-atom interferometers. The projection of AEDGE [168] and AION-km [165] are shown in the dashed dark green and dashed green lines, respectively. One may find that the constraints and projections from the ground-based and low-altitude experiments get weakened or cut off in the strong coupling region. This is caused by the scalar's matter effect sourced by the earth, one of the characteristics of the quadratic scalar-SM coupling. Following [162, 163], we have

$$d_{\gamma,2,{\rm crit}} = \frac{m_{\rm pl}^2 R_\oplus}{3 M_\oplus Q_{\gamma,\oplus}} \sim {\rm few} \times 10^{11}, \tag{49}$$

where $d_{\gamma,2,{\rm crit}}$ is the scalar's critical value for the matter effect to appear, $R_\oplus \sim 6 \times 10^3$km is the earth's radius, $M_\oplus \sim 6 \times 10^{24}$kg is the earth's mass, and $Q_{\gamma,\oplus} \sim 10^{-3}$ is the earth's dilaton charge. When $d_{\gamma,2} \gtrsim d_{\gamma,2,{\rm crit}}$, the scalar's Compton wavelength is smaller than the earth's radius. In this situation, the scalar easily overcomes the spatial gradient and is pulled toward the origin, so its near-ground and underground oscillation amplitudes are highly

---

[4] Here, one may be curious about the nonoverlapping between the thick dashed cyan and thick dashed magenta lines when $m_0 \gtrsim 10^{-16}$eV. To understand such splitting, one needs to review the exact definition of η in Eq. (20), which is $\eta := 2m_T/H$ (Here $\mathcal{S} \simeq 1$). When $3H = m_0$, to make $m_T > m_0$, one needs $\eta > 6$. Since $\eta \propto d_{\gamma,2}^{1/2}$, the values of $d_{\gamma,2}$ for the thick dashed cyan line ($m_T|_{3H=m_0} = m_0$) and the thick dashed magenta line ($\eta = 1$) have a factor "36" difference.

suppressed. Even so, if the experiments are carried on in space with altitudes comparable with the earth's radius (for example, AEDGE), the screen effect sourced by the earth can be largely alleviated.

Unlike the type-A model, the type-B model has strong constraints from the early universe processes, such as CMB and BBN, which are comparable with the terrestrial constraints. The reason for this character is that when tracing back to the early universe with the ϕ's abundance determined, $\Delta\alpha_{\rm em}$ increases much more for the type-B model than the type-A model. For the former analysis of the CMB and BBN bounds on the quadratic scalar-photon coupling, one can refer to [93, 95, 96][5]. Considering the thermal effect in Subsec. III B, we impose the constraints on the type-B scalar's parameter space using the current cosmological constraints on $\Delta\alpha_{\rm em}/\alpha_{\rm em}$, which are [93, 94][6]

$$(\Delta\alpha_{\rm em}/\alpha_{\rm em})_{\rm CMB} \lesssim 2 \times 10^{-3}, \qquad (\Delta\alpha_{\rm em}/\alpha_{\rm em})_{\rm BBN} \lesssim 6 \times 10^{-3} \,. \tag{50}$$

In the right panel of Fig. 7, the CMB constraint is shown as the shaded orange region, and the BBN constraint is shown as the shaded purple region.

Based on the left panel of Fig. 7, let us discuss the detectability of the dark photon dark matter freeze-in via the varying kinetic mixing. Given the scalar fraction $\mathcal{F} \simeq 10^{-3}$, for the model to be tested by the proposed experiments but not excluded by CMB/BBN, the dark gauge coupling needs to be within the range $10^{-10} \lesssim e' \lesssim 10^{-6}$. When $\mathcal{F}$ varies, the relative position between the black lines and the non-EP experiments does not change qualitatively because all these constraints essentially come from $\Delta\alpha_{\rm em} \propto d_{\gamma,2}|\phi|^2$. In this case, their positions are rescaled by $\mathcal{F}^{-1}$ in the weak coupling region. Differently, what the equivalence principle experiments are testing is the acceleration difference of the objects A and B, which obeys $|a_A - a_B|/|a_A + a_B| \propto d_{\gamma,2}^2 \phi|\nabla\phi|$ according to [162, 163]. From this, we know that the constraints on $d_{\gamma,2}$ from the equivalence principle test should be rescaled by $\mathcal{F}^{-1/2}$ in the weak coupling region. When $\mathcal{F} \lesssim 10^{-8}$, the equivalence principle constraints are stronger than the current CMB, BBN, and clock constraints. We leave detailed discussions on the $\mathcal{F}$-dependence of the constraints and theoretical benchmarks to our future work.

At the end of this section, we want to comment on the constraints imposed by the black hole superradiance. For the $\mathcal{F} \simeq 1$ case, the current constraints from the supermassive black holes exclude the region $10^{-21}{\rm eV} \lesssim m_0 \lesssim 10^{-17}{\rm eV}$ [158–161, 187], and the constraints from the solar mass black holes exclude the region $10^{-13}{\rm eV} \lesssim m_0 \lesssim 10^{-11}{\rm eV}$ [188]. However, since ϕ's self-interaction is $\lambda_\phi \sim m_0^2/f^2$, smaller $\mathcal{F}$ leads to smaller f, which increases λ_ϕ. From [161, 188] we know that, for the scalar as the subfraction of the dark matter, the superradiance constraints are alleviated by the scalar's large attractive self-interaction.

V. $\mathbb{Z}_N$-PROTECTED SCALAR NATURALNESS

Since the Yukawa interaction in Eq. (4) breaks Φ's global $U(1)$ symmetry, the ultralight CP-even scalar ϕ suffers from large quantum correction, which is a common problem in many ultralight scalar models. Taking the type-B model in Sec. II as an example, we have the mass correction $\Delta m_\phi \sim yM$, and its benchmark value

$$\Delta m_\phi \sim 10^{-11}{\rm eV} \left(\frac{\epsilon_{\rm FI}}{10^{-12}}\right) \left(\frac{M}{10{\rm TeV}}\right)^2 \left(\frac{10^{17}{\rm GeV}}{|\phi|_{\rm osc}}\right) \left(\frac{1}{e'}\right), \tag{51}$$

which is much larger than the scalar's bare mass. For the type-A model, the Coleman-Weinberg potential is $V_{\rm cw} \sim yM^3 f \sin(\phi/f)$. Given that $r \ll 1$, the type-A model's mass quantum correction $\Delta m_\phi \sim yM/r^{1/2}$ is even much larger. Because $V_{\rm cw}$'s minimum of the type-A model is not at zero, one need to introduce additional tadpole counterterm to forbid ϕ to have the late-time nonzero displacement.

Although such a naturalness problem exists in the minimal model, by imposing an extra $\mathbb{Z}_N$ symmetry [97, 98], the global $U(1)$ symmetry can be approximately restored, so the quantum correction is exponentially suppressed. In such setup, for the type-A and type-B models, the mass fine-tuning is exponentially solved. In addition, for the type-A

---

[5] The results in [95, 96] cannot be recast to our model directly because these works constrain the coupling $\phi^2 F^2$ which can be classified into the case where ϕ starts in the range $-\pi f/2 \lesssim \phi_{\rm rh} \lesssim \pi f/2$. We are discussing the initial wrong vacuum case where $\pi f/2 \lesssim \phi_{\rm rh} \lesssim 3\pi f/2$.

[6] To double-check our results, we reproduce the CMB and BBN constraints in [93] by using the former CMB bound $\Delta\alpha_{\rm em}/\alpha_{\rm em} \lesssim 10^{-2}$ used in [93] and by only including the bare potential effect during BBN, respectively.
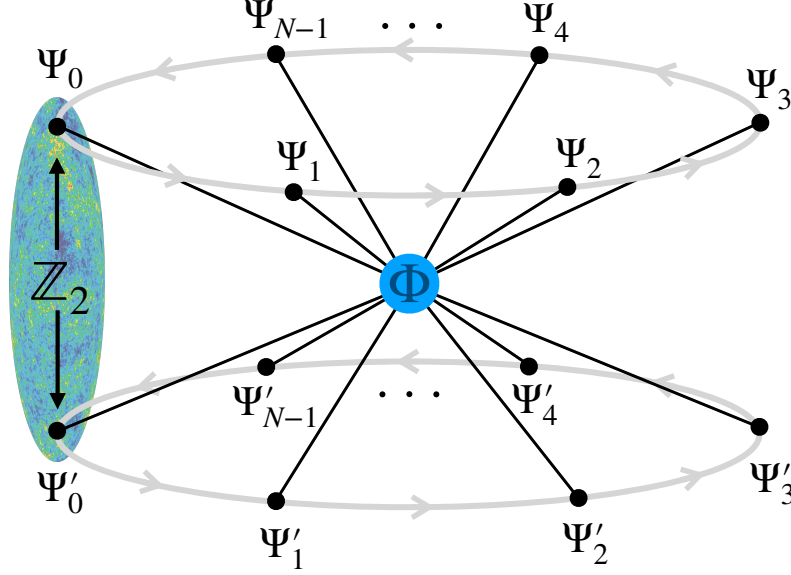
Figure 8. The schematic diagram of the $\mathbb{Z}_N$ invariant UV model. The messenger particles $\Psi_k^{(\prime)}$ $(k = 0, 1, \cdots, N-1)$ are all coupled with the complex scalar Φ, where "k" labels the kth world and $k = 0$ is our world which experienced the reheating. Because of the suppression from $y^{(\prime)}$, kth and jth universes $(k \neq j)$ do not talk with each other. Here, the $\mathbb{Z}_N$ rotation $\Phi \to \Phi \exp(i\, 2\pi/N)$, $\Psi_k^{(\prime)} \to \Psi_{k+1}^{(\prime)}$ is labeled by the gray arrowed circles. The $\mathbb{Z}_2$ symmetry between Ψ_k and Ψ'_k, which is exact for the type-B model $(y' = -y)$ and approximate for the type-A model $(y \neq 0, y' = 0)$, eliminates the time-independent part of the kinetic mixing.

model, the one-loop tadpole is also negligible. To realize this, we introduce N copies of the worlds containing the standard model sector (SM_k), the dark sector (DS_k), and the portal $(\mathcal{O}_{Pk})$ where $k = 0, 1, \ldots, N-1$. Because of the $\mathbb{Z}_N$ symmetry, the system is invariant under the transformation

$$\Phi \to \Phi \exp\left(i\frac{2\pi}{N}\right) \ , \ (\text{SM} + \mathcal{O}_P + \text{DS})_k \to (\text{SM} + \mathcal{O}_P + \text{DS})_{k+1} \ , \tag{52}$$

so the lowest order effective operator is

$$\mathcal{L}_{U(1)} = \text{const} \times \frac{\Phi^N}{\Lambda_1^{N-4}} + \text{h.c.} \tag{53}$$

which is invariant under the $\mathbb{Z}_N$ transformation but not invariant under the $U(1)$ transformation. Such dimension-N operator shows that even though the global $U(1)$ symmetry is broken, as long as the symmetry under the discrete subgroup $\mathbb{Z}_N$ still exists, the quantum correction $\Delta m_\phi^2 \propto f^{N-2}/\Lambda_1^{N-4}$ is exponentially suppressed by N. If N is an odd number and the exact $\mathbb{Z}_2$ symmetry under $\mathcal{C}_d$ $(\Phi \to -\Phi^\dagger)$ is imposed, the lowest order effective operator is $\Phi^{2N}/\Lambda_2^{2N-4}$, so the mass quantum correction is $f^{2N-2}/\Lambda_2^{2N-4}$[7]. As long as $\Delta m_\phi^2 \lesssim m_0^2$, the scalar's bare mass m_0 softly breaking the $\mathbb{Z}_N$ symmetry can be naturally small.

---

[7] Here we put the subscript "l" for the effective energy scale Λ_l in the $\mathbb{Z}_N$ invariant operator $\mathcal{L} \supset \text{const} \times \Phi^{lN}/\Lambda_l^{lN-4} + \text{h.c.}$, because these scales are hierarchically different for different "l"s when the Yukawas are small, which reveals the necessity of more detailed calculation to go beyond the purely qualitative level of understanding how the $\mathbb{Z}_N$ symmetry protects the CP-even scalar's naturalness. From Eq. (64) in the later context, we will find that $\Lambda_l \sim M/y^{lN/(lN-4)} \sim \Lambda_{\gamma,i}/y^{4/(lN-4)}$.

A. $\mathbb{Z}_N$-Protected Model

To build a concrete varying kinetic mixing model without the naturalness problem, we embed the simple model described by Eq. (4) into the Lagrangian

$$\mathcal{L}_{\mathrm{UV}} \supset \sum_{k=0}^{N-1} \left(y e^{i\frac{2\pi k}{N}} \Phi \bar{\Psi}_k \Psi_k + y' e^{i\frac{2\pi k}{N}} \Phi \bar{\Psi}'_k \Psi'_k + \mathrm{h.c.} \right) - M \sum_{k=0}^{N-1} (\bar{\Psi}_k \Psi_k + \bar{\Psi}'_k \Psi'_k) - \lambda \left(|\Phi|^2 - \frac{f^2}{2} \right)^2 \tag{54}$$

being invariant under the $\mathbb{Z}_N$ transformation $\Phi \to \Phi \exp\left(i\frac{2\pi}{N}\right)$, $\Psi_k^{(\prime)} \to \Psi_{k+1}^{(\prime)}$, $A_k^{(\prime)} \to A_{k+1}^{(\prime)}$. Here, Ψ_k and Ψ'_k, two doubly charged fermions in the k-th universe, carry the same kth-hypercharge but the opposite kth-dark hypercharge. Following the phase choice in Sec. II, we choose $c = \pi/2$, $\Phi = \frac{if}{\sqrt{2}} e^{i\phi/f}$ and introduce the $\mathbb{Z}_2$-invariant bare potential in Eq. (10) to ensure the late-time closing of the kinetic mixing portal. When the ultralight scalar ϕ is nonzero, $\Psi_k^{(\prime)}$'s effective masses become[8]

$$M_k^{(\prime)}(\phi) = M \left[1 + r^{(\prime)} \sin\left(\frac{\phi}{f} + \frac{2\pi k}{N}\right) \right], \quad \text{where } r^{(\prime)} = \frac{\sqrt{2}\, y^{(\prime)} f}{M}. \tag{55}$$

To gain more intuition of the setup of the $\mathbb{Z}_N$-invariant model, our readers can refer to Fig. 8, the schematic diagram of the $\mathbb{Z}_N$ UV Lagrangian described by Eq. (54). In this figure, Φ is the axle attached to all N copies of the universes, and "$\mathbb{Z}_2$" refers to $\Psi_k^{(\prime)}$'s mass degeneracy which is exact when $y' = -y$ (Type-B) or approximate when $y' \neq y$ (Type-A).

In the low energy limit, the heavy fermions $\Psi_k^{(\prime)}$ are integrated out, so the IR Lagrangian becomes

$$\mathcal{L}_{\mathrm{IR}} \supset \sum_{k=0}^{N-1} \left[\frac{1}{2} \epsilon_k F_{k\,\mu\nu} F_k^{\prime\,\mu\nu} + \frac{1}{4} \left(\frac{\Delta\alpha_{\mathrm{em}}}{\alpha_{\mathrm{em}}} \right)_k F_{k\,\mu\nu} F_k^{\mu\nu} \right], \tag{56}$$

where

$$\epsilon_k = \frac{\sqrt{2} e e' (y - y') f}{6\pi^2 M} \sin\left(\frac{\phi}{f} + \frac{2\pi k}{N}\right) \tag{57}$$

and

$$\left(\frac{\Delta\alpha_{\mathrm{em}}}{\alpha_{\mathrm{em}}} \right)_k = \frac{e^2}{6\pi^2} \left[-\frac{\sqrt{2}(y + y') f}{M} \sin\left(\frac{\phi}{f} + \frac{2\pi k}{N}\right) + \frac{(y^2 + y'^2) f^2}{M^2} \sin^2\left(\frac{\phi}{f} + \frac{2\pi k}{N}\right) \right]. \tag{58}$$

From Eq. (56), Eq. (57) and Eq. (58), one can easily find that the IR Lagrangian is invariant under the $\mathbb{Z}_N$ transformation $\phi \to \phi + \frac{2\pi}{N}$, $A_k^{(\prime)} \to A_{k+1}^{(\prime)}$. Here, $(\mathrm{SM} + \mathcal{O}_P + \mathrm{DS})_0$ is our universe which experiences the reheating, but the other universes are not reheated at all. When $m_0 \lesssim H$, ϕ begins the damped oscillation, so the kinetic mixing ϵ_0 between SM_0 and DS_0 gradually decreases towards zero as described in Sec. II and Sec. III.

B. Quantum Correction of ϕ

For the ultralight scalar ϕ in Eq. (54), the leading order quantum correction can be described by the one-loop Coleman-Weinberg potential

$$V_{\mathrm{cw}}(\phi) = -\frac{1}{16\pi^2} \sum_{k=0}^{N-1} M_k^4(\phi) \left[\log\left(\frac{M_k^2(\phi)}{\mu^2} \right) - \frac{3}{2} \right] + (M_k \to M'_k). \tag{59}$$

---

[8] r and r' representing the Yukawa couplings in Eq. (55) are already defined in Eq. (6). However, we still list them here as a reminder because r and r' appear in the suppression factors of the quantum correction in the $\mathbb{Z}_N$-naturalness.

As discussed in [103], the Fourier series of any scalar potential respecting the $\mathbb{Z}_N$ symmetry only receives contributions on lNth modes (l is a positive integer number) so that the Coleman-Weinberg potential can be written as

$$V_{\text{cw}}(\theta) = N \sum_{\ell=1}^{\infty} \widetilde{V}_{\text{cw}}(\ell N) \cos(\ell N \theta), \quad \text{where } \theta = \frac{\phi}{f} + \frac{\pi}{2}. \tag{60}$$

In Eq. (60), $\widetilde{V}_{\text{cw}}(\ell N)$ denotes the Fourier coefficient of the single-world Coleman-Weinberg potential, the prefactor N comes from the contribution from N worlds which have the equal contribution to the Fourier coefficient, and $\cos(lN\theta)$ comes from the effective operator $\mathcal{L} \supset \text{const} \times (\Phi^{lN} + \Phi^{\dagger lN})/\Lambda_l^{lN-4}$.

Now, let us calculate the Fourier coefficient in (60) through the equation

$$\widetilde{V}_{\text{cw}}(lN) = -\frac{M^4}{4\pi^3} \int_0^{\pi} \cos(lN\theta)(1 - r\cos\theta)^4 \log(1 - r\cos\theta)d\theta + (r \to r'). \tag{61}$$

Expanding the polynomial $(1 - r\cos\theta)^4$ and carrying the integration over θ, the Fourier coefficient when $N > 4$ can be exactly written as[9]

$$\widetilde{V}_{\text{cw}}(lN) = \frac{M^4}{4\pi^2} \sum_{j=0}^{4} \sum_{m=0}^{j} \binom{4}{4-j, j-m, m} \frac{(-1)^j}{lN-j+2m} \left(\frac{r}{2}\right)^{lN+2m} \left(\frac{1-\sqrt{1-r^2}}{r^2/2}\right)^{lN-j+2m} + (r \to r'). \tag{63}$$

In the Appendix. C, we list two ways to derive a compact formula for the $\mathbb{Z}_N$ Coleman-Weinberg potential precisely expanded to all orders of r, which is obtained for the first time as far as we have known. After omitting r's higher order terms in the exact Fourier coefficient (63), we express the Coleman-Weinberg potential as

$$V_{\text{cw}}(\phi) \simeq \frac{M^4 N}{8\pi^2} \left\{ \left(r^N + r'^N + \cdots\right) G(N) \cos\left[N\left(\frac{\phi}{f} + \frac{\pi}{2}\right)\right] \right. \\ \left. + \left(r^{2N} + r'^{2N} + \cdots\right) G(2N) \cos\left[2N\left(\frac{\phi}{f} + \frac{\pi}{2}\right)\right] + \cdots \right\}, \tag{64}$$

where "$\cdots$"s in the brackets of (64) denote $r^{(\prime)}$'s higher order terms with the same parity as the lowest order terms. In (64), the function $G(n)$ is

$$G(n) := \frac{1}{2^{n-1}} \sum_{j=0}^{4} \binom{4}{j} \frac{(-1)^j}{n-j} = \frac{3(n-5)!}{2^{n-4} n(n-1)!}. \tag{65}$$

Alternatively, Eq. (64) can be derived from Eq. (59) by applying the cosine function sum rules

$$\sum_{k=1}^{N} \cos^m\left(\theta + \frac{2\pi k}{N}\right) = \sum_{l=0}^{[m/N]} \mathcal{C}_{lmN} \cos(lN\theta) + \mathcal{D}_m, \quad \text{where } \mathcal{C}_{lmN}\big|_{m=lN} = \frac{1}{2^{lN-1}}. \tag{66}$$

According to Eq. (55), M_k is a cosine function of θ, so we can expand the Coleman-Weinberg potential in Eq. (59) as a polynomial function of $\cos(\theta + 2\pi k/N)$. Afterward, by employing these cosine sum rules, we can also write the Coleman-Weinberg potential in the form as shown in Eq. (64). The concrete formulas of the constants $\mathcal{C}_{lmN}$ and $\mathcal{D}_m$ can be found in Appendix. C, Eq. (C5). Eq. (66) shows that only when the cosine function's power in the effective potential is greater than N, the non-constant terms emerge. Since the cosine function appearing in the potential is always accompanied by r, based on the cosine sum rules, one can find that the lowest order $\mathbb{Z}_N$ potential is proportional to r^N if there is no further cancellation coming from the exact $\mathbb{Z}_2$ symmetry.

---

[9] In [189] we find the integral

$$\int_0^{\pi} \log[1 - r\cos(\theta)]\cos(n\theta)d\theta = -\frac{\pi}{n}[X(r)]^n, \quad \text{where } X(r) = \frac{1-\sqrt{1-r^2}}{r}. \tag{62}$$

Given that $r \ll 1$, the factor $r^N G(N)$ in Eq. (64) indicates that the quantum correction of m_ϕ^2 is suppressed by the $(r/2)^{N-5/2}$ factor in the type-A model, and $(r/2)^{N-2}$ factor in the type-B model. For the freeze-in of dark photon dark matter, r's benchmark value is

$$r \sim 10^{-10} \left(\frac{\epsilon_{\rm FI}}{10^{-12}} \right) \left(\frac{1}{e'} \right) \left(\frac{f}{|\phi|_{\rm osc}} \right). \tag{67}$$

In such a case, for $e' \sim \mathcal{O}(1)$, as long as $N \gtrsim 7$, ϕ's naturalness problem can be solved entirely. For smaller e', r is larger, so N needs to be larger to solve the naturalness. However, as long as $e' \gg 10^{-10}$ which is in the permitted region of the current constraints, $r \ll 1$, the $\mathbb{Z}_N$ scenario protecting the pseudo Goldstone boson ϕ's naturalness always works.

Since $V_{\rm cw}$ receives contribution from both r and r', N's parity matters. For even N, the first term in Eq. (64) shows that both r and r' provide a positive contribution, so the leading order correction starts from r^N. In contrast, if N is odd, r and r' have opposite signs, so the quantum correction from $r^N + r'^N$ is reduced. When $r = -r'$ (Type-B model), the $(r^N + r'^N)\cos[N(\phi/f + \pi/2)]$ term has the exact cancellation, so the leading order correction starts from the $(r^{2N} + r'^{2N})\cos[2N(\phi/f + \pi/2)]$ term. We want to remind our readers that such cancellation happens in all orders because the front factor of the higher order terms $\cos[N(\phi/f + \pi/2)]$ in Eq. (63) or Eq. (C1) are $r^{(\prime)N+2j}$ which has the same parity as $r^{(\prime)N}$. This is consistent with the EFT analysis at the beginning of this section.

Before closing the discussion in this section, we want to make some extra comments besides solving the ultra-light CP-even scalar's naturalness problem in our concrete situation: Our model, i.e., $\mathbb{Z}_N$-protected varying kinetic mixing, provides a systematic approach to solve the scalar's naturalness problem for both the linear (Type-A) and quadratic (Type-B) scalar-photon couplings. This is the extension and unification of [102] and [163], which focus on the linear and quadratic scalar-photon coupling, respectively. Furthermore, armed with two different methods, i.e., the Fourier transformation and the cosine sum rules discussed in this section and in Appendix. C, for the first time, one can completely and precisely calculate the pseudo-Goldstone boson's $\mathbb{Z}_N$-invariant Coleman-Weinberg potential previously appearing in [97, 98, 102] to arbitrary orders. We wish such calculations could shed light on the formalism of the $\mathbb{Z}_N$-naturalness itself.

VI. VARYING KINETIC MIXING FROM DIRAC GAUGINO

Motivated by stabilizing the hierarchy between the light scalars and the heavy fermions, we discuss one of the possible supersymmetric extensions of the varying kinetic mixing in the Dirac gaugino model [190, 191] with the superpotential

$$\mathcal{W} = \frac{\sqrt{2}\, W'_\alpha W_j^\alpha A_j}{\Lambda_{{\rm D},j}}. \tag{68}$$

In Eq. (68), W_j is the gauge field strength of the SM gauge group $G_{{\rm SM},j}$ where the label $j = 1, 2, 3$ denotes the SM gauge groups $U(1)_Y$, $SU(2)_L$ and $SU(3)_c$, respectively, W' is the gauge field strength of $U(1)_d$, and A_j is the chiral multiplet. The operator in Eq. (68) in hidden sector models was firstly introduced by [192] and further understood by [190] afterward as the *supersoft* operator such that it provides the Dirac gaugino masses and does not give logarithmic divergent radiative contributions to other soft parameters. Writing A_j, W_j and W' in terms of the Taylor expansion of the Grassmann variable θ, we have $A_j \supset (S_j + iP_j)/\sqrt{2} + \sqrt{2}\theta \tilde{a}_j$, $W_j^\alpha \supset \lambda_j^\alpha + F_j^{\mu\nu}(\sigma_{\mu\nu}\theta)^\alpha + D\,\theta^\alpha$, and $W'_\alpha \supset F'_{\mu\nu}(\sigma^{\mu\nu}\theta)_\alpha + \langle D' \rangle \theta_\alpha$. Plugging these expanded fields into Eq. (68), and doing the integration over θ^2 firstly and then the auxiliary fields, we have the effective Lagrangian

$$\mathcal{L} \supset -\frac{1}{\Lambda_{{\rm D},j}} {\rm tr}\left(S_j F_j^{\mu\nu} \right) F'_{\mu\nu} - \frac{1}{\Lambda_{{\rm D},j}} {\rm tr}\left(P_j F_j^{\mu\nu} \right) \widetilde{F}'_{\mu\nu} - m_{{\rm D},j} \tilde{a}_j \lambda_j - 2 m_{{\rm D},j}^2 S_j^2 + \cdots , \tag{69}$$

where $S_j(P_j)$ is the CP-even (CP-odd) scalar, λ_j is the gaugino, and $m_{{\rm D},j} = \langle D' \rangle / \Lambda_{{\rm D},j}$ is the gaugino's Dirac mass given by the scale of SUSY breaking. One should note that in Eq. (69), S_j's mass term $\mathcal{L} \supset -2m_{{\rm D},j}^2 S_j^2$ comes from integrating out the D-term (On the contrary, P_j has no extra mass contribution). It is because the supersymmetry

is protected that the mass of S_j is correlated with the mass of the gaugino λ_j. Consequently, S_j is pushed to the heavier mass range given that the gaugino mass is highly constrained: According to [193–196], the LHC has already excluded the electroweakinos and the gluinos masses below $\mathcal{O}(100\text{GeV})$ and $\mathcal{O}(\text{TeV})$ respectively. Unlike the previous discussion, in the Dirac gaugino model, S_j cannot be the ultralight scalar where the misalignment mechanism provides a natural way to open the portal in the early time but gradually close it in the late time. Even so, it is still possible to realize the temporary period of $\langle S_j \rangle \neq 0$ in the early universe through the two-step phase transition, also referred to as the VEV Flip-Flop in some specific dark matter models [39–41]. The concrete model building and the phenomenology are beyond the scope of this paper.

In the $j = 1$ case, the first term in Eq. (69) containing the CP-even scalar S_1 corresponds to the kinetic mixing portal between $U(1)_Y$ and $U(1)_d$ which is determined by S_1's VEV. The second term in Eq. (69) containing P_1 (axion) leads to the dark axion portal which is investigated in [197–207]. There are several major differences between the kinetic mixing portal $\mathcal{L} \supset -S_1 F^{\mu\nu} F'_{\mu\nu}/\Lambda_{\text{D},1}$ and the dark axion portal $\mathcal{L} \supset -P_1 F^{\mu\nu} \widetilde{F}'_{\mu\nu}/\Lambda_{\text{D},1}$: 1. In the Dirac gaugino model, S_1's mass is correlated with the λ_1^α mass which is pushed to $\mathcal{O}(100\text{GeV})$ scale by LHC, while P_1's shift symmetry protests its arbitrarily small bare mass. 2. The VEV of P_1 does not play a direct physical role because it only contributes to the total derivative term in the Lagrangian (P_1's time or spatial derivative still has nontrivial physical effects nonetheless).

In the $j = 2, 3$ cases, if $\langle S_j^a \rangle \neq 0$, the first term in Eq. (69) would mix the non-Abelian gauge field with the dark photon such that the non-Abelian gauge symmetry is broken. Being referred to as the non-Abelian kinetic mixing[21, 208–213], the constant mixing models are highly constrained by the collider experiments. However, in the high-temperature environment of the early Universe, the large non-Abelian kinetic mixing can possibly be realized for the non-Abelian vector dark matter production and other intriguing phenomena. We leave the detailed discussion in future work.

VII.   OTHER COSMOLOGICALLY VARYING PORTALS

Let us begin with the general form of the cosmologically varying portals through which the dark and the visible sectors are connected. To be more generic, we write them as

$$\mathcal{L} \supset \frac{\phi}{\Lambda^{d-4}} \, \mathcal{O}_{\text{DS}} \mathcal{O}_{\text{SM}}, \text{ where } d = d_{\text{SM}} + d_{\text{DS}} + 1. \tag{70}$$

In Eq. (70), $\mathcal{O}_{\text{SM}}$ and $\mathcal{O}_{\text{DS}}$ are the operators of the visible sector and the dark sector, respectively, d_{SM} and d_{DS} denote the dimensions of these two operators, and d is the dimension of the time-varying portal. To simplify the notation of Eq. (70), we drop the (spacetime, spin, flavor, …) indices of $\mathcal{O}_{\text{SM}}$ and $\mathcal{O}_{\text{DS}}$ whose contraction makes the varying portal to be a singlet. For simplicity, we only keep the linear form of the CP-even scalar ϕ, even though in the UV theory, the non-linearity may appear, as we have seen in Eq. (7). Based on the EFT, we know that when the effective operator Eq. (70) is introduced, the operators merely containing ϕ and $\mathcal{O}_{\text{SM}}$ also appear because the symmetry does not forbid them. The co-appearance of the effective operator shown in Eq. (70) and the scalar-SM coupling provides an excellent chance to test these kinds of models from the experiments detecting the portal itself and the ones measuring the scalar-SM coupling. In the rest of this section, we will give some specific examples of the varying portals and show how these minimal extensions illuminate the dark matter model building.

Let us briefly review the varying kinetic mixing portal in the EFT language. After choosing

$$\mathcal{O}_{\text{SM},\mu\nu} = F_{\mu\nu} \quad \text{and} \quad \mathcal{O}_{\text{DS},\mu\nu} = F'_{\mu\nu}, \tag{71}$$

Eq. (70) goes back to the operator $\mathcal{L} \supset \phi F_{\mu\nu} F'^{\mu\nu}/\Lambda$ discussed before. Through this operator, the dark photon dark matter can be produced without violating the stringent constraints as shown in Sec. IV. Since the spacetime indices of $F_{\mu\nu}$ need to be contracted, the lowest order operator of the scalar-SM coupling is $\phi F_{\mu\nu} F^{\mu\nu}$. If there is an exact $\mathbb{Z}_2$ symmetry invariant under the dark charge conjugation $\phi \to -\phi$, $F'_{\mu\nu} \to -F'_{\mu\nu}$, $\phi F_{\mu\nu} F^{\mu\nu}$ is forbidden, so the lowest order operator of the scalar-SM coupling becomes $\phi^2 F_{\mu\nu} F^{\mu\nu}$. The table-top experiments testing the α_{em} variation and the equivalence principle violation can be used to test this model because of the existence of $\phi F_{\mu\nu} F^{\mu\nu}$

or $\phi^2 F_{\mu\nu}F^{\mu\nu}$.

In other situations where $\mathcal{O}_{\rm SM}$ is invariant under arbitrary global and gauge transformations, there are no more indices to contract, so the lowest order operator of the scalar-SM coupling is $\phi\,\mathcal{O}_{\rm SM}$ or $\phi^2\,\mathcal{O}_{\rm SM}$ depending on whether the exact $\mathbb{Z}_2$ symmetry, i.e., the invariance under $\phi \to -\phi$, $\mathcal{O}_{\rm DS} \to -\mathcal{O}_{\rm DS}$ transformation, exists or not. One typical example is that

$$\mathcal{O}_{\rm SM} = |H|^2 \quad \text{and} \quad \mathcal{O}_{\rm DS} = s^2, \tag{72}$$

where s is a scalar singlet in the dark sector. Here, $\mathcal{L} \supset \lambda_s \mathcal{O}_{\rm DS}\mathcal{O}_{\rm SM} = \lambda_s s^2|H|^2$ is well-known as the singlet-scalar Higgs portal (SHP) through which the dark matter s reaches today's relic abundance (The dominant channels are $ss \to f^- f^+, W^- W^+, ZZ, hh, \cdots$. Here, f refers to the SM fermions.) [10–12]. Besides, because this Lagrangian is invariant under the $\mathbb{Z}_2$ transformation $s \to -s$, s is stable. Although SHP provides such a simple and effective way to generate the scalar dark matter in accordance with the CMB measurement ($\Omega_s h^2 \simeq 0.12$), in the mass range $m_s \lesssim 1\,{\rm TeV}$, most of its parameter space except the narrow window of the resonance ($m_s \simeq m_h/2$) is excluded by the Higgs invisible decay $h \to ss$ [214, 215], the dark matter direct detection experiments (LUX, XENON1T, PandaX-II) and the indirect detections (AMS, Fermi) [63, 216–218]. By introducing the time-varying SHP

$$\mathcal{L} \supset \frac{\phi}{\Lambda} s^2 |H|^2 \tag{73}$$

as the minimum extension, the parameter space is widely extended. There, ϕ's misalignment supports s's freezeout at the early universe and then starts the damped oscillation such that $\langle \sigma v \rangle_{ss} \propto (T/T_{\rm osc})^3$ when $T \lesssim T_{\rm osc}$. For this model, there are two types of experiments: 1. The future direct detection experiments (XENONnT, LUX-ZEPLIN, DarkSide-20k, DARWIN) which rely on partially opened SHP today. 2. The table-top experiments and the astrophysical observations testing the $\phi|H|^2$ or $\phi^2|H|^2$ operator (See [136, 186, 219, 220] for the detections of the $\phi|H|^2$ operator).

Another example of the singlet $\mathcal{O}_{\rm SM}$ is that

$$\mathcal{O}_{\rm SM} = \bar{Q}Hq_R \text{ or } \bar{L}He_R \quad \text{and} \quad \mathcal{O}_{\rm DS} = \tilde{s}. \tag{74}$$

In this model, $\tilde{s}$ is the scalar mediator which interacts with the dark matter particle χ via the CP-odd coupling $\mathcal{L} \supset iy_\chi \tilde{s}\, \overline{\chi}\gamma^5\chi$ (Here we denote the scalar mediator by "$\sim$" to distinguish it from the scalar dark matter discussed in the previous paragraph). Given the constant portal $\mathcal{L} \supset \mathcal{O}_{\rm DS}\mathcal{O}_{\rm SM}/\Lambda = y_f \tilde{s}\bar{f}f$ where $y_f = v_h/\sqrt{2}\Lambda$, χ reaches today's relic abundance through the freezeout channel $\chi^-\chi^+ \to f^-f^+$ whose cross section is $\langle \sigma v \rangle_{\tilde{s}\tilde{s}} \sim y_f^2 y_\chi^2 m_\chi^2/m_{\tilde{s}}^4$. Here, v_h is the Higgs VEV, and Λ is the effective scale of the constant portal. Since $\chi^-\chi^+ \to f^-f^+$ is s-wave (The leading order of $\langle \sigma v \rangle_{\chi^-\chi^+}$ is independent of dark matter relative velocity), the region $m_\chi \lesssim 10\,{\rm GeV}$ is excluded by the measurement of CMB anisotropy [3]. To produce lighter but CMB-friendly dark matter, we introduce the operator

$$\mathcal{L} \supset \frac{\phi}{\Lambda^2} \tilde{s}\bar{L}He_R \text{ or } \frac{\phi}{\Lambda^2} \tilde{s}\bar{Q}Hq_R \tag{75}$$

as the minimal extension. Through the ϕ-dependent Yukawa coupling $\mathcal{L} \supset y_f(\phi)\tilde{s}\bar{f}f$ where $y_f(\phi) = \phi v/\sqrt{2}\Lambda^2$ and the aforementioned CP-odd Yukawa coupling $\mathcal{L} \supset iy_\chi \tilde{s}\, \overline{\chi}\gamma^5\chi$, the dark matter lighter than $10\,{\rm GeV}$ can reach today's relic abundance without violating CMB annihilation bound as long as ϕ's damped oscillation begins earlier than the CMB stage ($T_{\rm CMB} \sim {\rm eV}$). For this model, there are two kinds of experiments: 1. The next-generation CMB experiments (such as the CMB-S4 [221–225]) and the future direct and indirect detection experiments. 2. The table-top experiments and astrophysical observations testing the variation of the SM fermion masses ($\phi\bar{f}f$ or $\phi^2\bar{f}f$ operator) [86, 88, 91, 92, 162, 163, 185, 186].

VIII.   CONCLUSION

In this work, we study the scalar-controlled kinetic mixing varying with the ultralight CP-even scalar's evolution during the cosmological evolution. Via such a dynamical portal, $\mathrm{keV} - \mathrm{MeV}$ dark photon dark matter is frozen-in, free from the late-universe exclusions, and has the kinetic mixing set by the scalar mass. More generally, this model can serve as the minimal solution for the tension between the portal dark matter's early-time production and late-time constraints. Furthermore, the scalar-photon coupling inevitably emerges from UV physics, modifying the universe's thermal history, varying the fine-structure constant, and violating the equivalence principle. These phenomenons provide excellent targets to test our model via the ultralight scalar experiments in the mass range $10^{-33}\mathrm{eV} \lesssim m_0 \ll \mathrm{eV}$. In the meantime, the scalar mass also determines the target values of the kinetic mixing for $\mathrm{keV} - \mathrm{MeV}$ dark photon dark matter experiments. In the rest of the paper, we study the $\mathbb{Z}_N$-protected naturalness of the ultralight CP-even scalar, the varying kinetic mixing from the Dirac gaugino model, and the dark matter via other cosmologically varying portals.

We begin our study by constructing the minimal model of the scalar-controlled kinetic mixing arising from the heavy doubly charged messengers. In our model, the $\mathbb{Z}_2$ symmetry under the dark charge conjugation is imposed to elimite the constant kinetic mixing but preserve the varying kinetic mixing. From the perspective of symmetry, the early-time openning and the late-time closing of the kinetc mixing portal results from the system's inverse $\mathbb{Z}_2$-breaking. Importantly, in such a setup, the scalar-photon coupling also occurs from the top-down theory. To classify the model, we name the theory with the approximate $\mathbb{Z}_2$ symmetry as the type-A model and the theory with the exact $\mathbb{Z}_2$ symmetry as the type-B model. Given this, the type-A model has linear scalar-photon coupling, and the type-B model has quadratic scalar-photon coupling. Then we systematically categorize the scalar's evolution under the combined effects of the thermal correction, bare potential, and the universe expansion. For the type-A and type-B models, there exist the experimentally allowed regions for the thermal misalignment, where the scalar acquires the nonzero displacement insensitive to the initial condition. We also find the thermal postponement of the oscillation starting in the type-B model initially staying in the wrong vacuum, which is the major feature of the trapped misalignment. Such delaying of the oscillation enhances the experimental signals. Afterward, we study $\mathrm{keV} - \mathrm{MeV}$ dark photon dark matter production via the varying kinetic mixing, where the kinetic mixing is $\epsilon_{\mathrm{FI}} \sim 10^{-12}$ for the dark photon freeze-in when $T \sim m_{A'}$ and decreases obeying the power law $T^{3/2}$ when the scalar does the late-universe damped oscillation. Therefore, the late-time kinetic mixing set by the scalar mass is free from constraints from stellar energy loss, dark matter direct detection, and the dark photon dark matter decay. In addition, the kinetic mixing during freeze-in provides the perfect experimental benchmarks in the ultralight scalar experiments in the mass range $10^{-33}\mathrm{eV} \lesssim m_0 \ll \mathrm{eV}$, including the test of the fine-structure constant variation and the equivalence principle violation. Since smaller dark gauge coupling leads to stronger signals, most of the e' space in the type-A model and the region $e' \lesssim 10^{-6}$ in the type-B model can be tested by proposed experiments such as clock comparison and cold-atom interferometry. For the smaller scalar relic fraction among dark matter, the constraints from the fine-structure constant variation keep the same, while the constraints from the equivalence principle experiments become more stringent.

We also detailedly study the $\mathbb{Z}_N$-protection of the ultralight CP-even scalar's naturalness in the varying kinetic mixing model. There, we embed the aforementioned minimal model into the model containing N worlds, such that the broken $U(1)$ shift symmetry is approximately restored. Generally, the lowest order potential in this setup comes from the Φ^N/Λ^{N-4} operator, which exponentially suppresses the scalar's quantum correction from heavy messengers. As long as $N \sim 10$, the quantum correction of the scalar mass can be much lighter than $10^{-33}\mathrm{eV}$. For the type-B model with odd N, the lowest order operator is Φ^{2N}/Λ^{2N-4} because of the cancellation from the exact $\mathbb{Z}_2$. Moreover, we expand the $\mathbb{Z}_N$ Coleman-Weinberg potential to all orders utilizing the Fourier transformation and the cosine sum rules. In the paper's final part, we discuss the Dirac gaugino model simultaneously inducing the varying kinetic mixing and dark axion portal. We also briefly discuss the dark matter models via other cosmologically varying portals. More specifically, we discuss the freeze-out of the dark Higgs dark matter lighter than $1\mathrm{TeV}$ via the varying Higgs portal and the CMB-friendly fermionic dark matter lighter than $10\mathrm{GeV}$ via the varying fermion portal.

Appendix A: Scalar's Analytical EOM Solutions: High-T

In this section, we solve ϕ's movement analytically in the high-temperature universe where the bare potential's effect is inferior. Taking the joint effects of the thermal mass and the universe's expansion into consideration, we write the equation of motion as

$$\delta\ddot{\phi} + 3H\delta\dot{\phi} \simeq -m_T^2\delta\phi, \quad \text{where } \delta\phi = \phi - \phi_{\min}. \tag{A1}$$

In Eq. (A1), $\phi_{\min}$ is the minimum of the thermal potential, i.e., V_T in Eq. (18), and $\delta\phi$ is the field displacement from such a thermal minimum. As we know in Eq. (19), within the $2\pi f$ periodicity, $\phi_{\min} = \pi f/2$ for the type-A model, and $\phi_{\min} = 0, \pm\pi f$ for the type-B model. In Eq. (A1), we use the linear approximation, because as long as ϕ is initially away from the hilltop of the thermal potential, the effect of the nonlinearity is negligible. Applying the equation $\frac{d}{dt} \simeq HT\frac{d}{dT}$, Eq. (A1) can be rewritten as

$$T^2 \frac{d^2\delta\phi}{dT^2} \simeq -\frac{\eta^2}{4}\delta\phi, \tag{A2}$$

which is well-known as the homogeneous linear equation. Utilizing the power-law ansatz, we obtain two independent solutions of Eq. (A2), which are

$$\delta\phi \propto T^{\frac{1\pm\sqrt{1-\eta^2}}{2}} \quad (\eta < 1), \quad \delta\phi \propto T^{\frac{1}{2}}, T^{\frac{1}{2}}\log\left(T/T_{\rm rh}\right) \quad (\eta = 1), \quad \delta\phi \propto T^{\frac{1\pm i\sqrt{\eta^2-1}}{2}} \quad (\eta > 1) \tag{A3}$$

for each case separately. Given the initial condition $\dot{\phi}_{\rm rh} = 0$, one can determine the unknown coefficients and write the solution as

$$\delta\phi \propto T^{\frac{1-\sqrt{1-\eta^2}}{2}} \times \left[1 - \left(\frac{\sqrt{1-\eta^2}-1}{\eta}\right)^2 \left(\frac{T}{T_{\rm rh}}\right)^{\sqrt{1-\eta^2}}\right] \quad (\eta < 1), \tag{A4}$$

$$\delta\phi \propto T^{\frac{1}{2}} \times \left[1 - \frac{1}{2}\log\left(\frac{T}{T_{\rm rh}}\right)\right] \quad (\eta = 1), \tag{A5}$$

and

$$\delta\phi \propto T^{\frac{1}{2}}\cos\left(\frac{\sqrt{\eta^2-1}\log\frac{T}{T_{\rm rh}}}{2}\right) \times \left[1 - \frac{1}{\sqrt{\eta^2-1}}\tan\left(\frac{\sqrt{\eta^2-1}\log\frac{T}{T_{\rm rh}}}{2}\right)\right] \quad (\eta > 1). \tag{A6}$$

Let us briefly explain the solution for each case individually. In the $\eta < 1$ case, whose solution is Eq. (A4), ϕ begins with the initial staticity after the reheating and then slowly slides to the thermal minimum, whose sliding velocity is suppressed by the small η. In the limit $\eta \ll 1$, one can have $\delta\phi \propto T^{\frac{\eta^2}{4}}$, meaning that ϕ is approximately static. The reason for ϕ's motionlessness is that the thermal effect is too weak to drive ϕ to move under the large Hubble friction. From Eq. (A4), we can also find the front coefficient of $T^{\frac{1-\sqrt{1-\eta^2}}{2}}$ dominates over the one of $T^{\frac{1+\sqrt{1-\eta^2}}{2}}$, because for
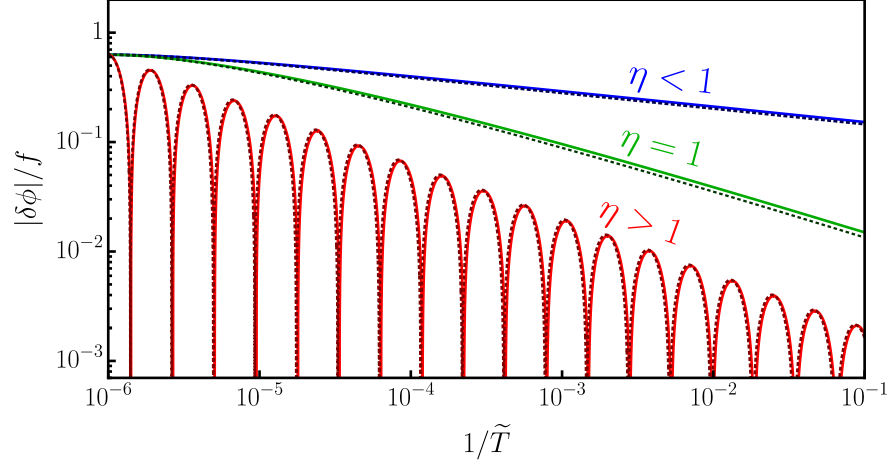
Scalar's High-T Evolution: Numerical vs Analytical

Figure 9. This plot describes the ultralight scalar's evolution in the high-temperature environment and compares the numerical (solid lines) and analytical (dotted dark lines) results listed in Eq. (A4), Eq. (A5), and Eq. (A6). In the plot, similar to Fig. 4, $\widetilde{T}$ is defined as $\widetilde{T} := T/T|_{3H=m_0}$. $|\delta\phi|$ represents the absolute value of the deviation from the thermal potential's minimum. Without loss of generality, we choose the type-A model as an example in this plot, and the discussion of the type-B model is quite similar. Here, the red, green, and blue colors represent the $\eta > 1$, $\eta = 1$, and $\eta < 1$ cases, respectively, and one can find that the numerical and analytical results for each case match magnificently well. We find that the red and green lines have approximately the same power law, i.e., $|\delta\phi| \propto \widetilde{T}^{1/2}$, whose slight deviation can be explained by the log term in Eq. (A5). We can also find that the red line's oscillation period appears the same in the plot with the log-scaled $1/\widetilde{T}$ axis. This is because the only temperature-dependence in Eq. (A6) comes from $\log \widetilde{T}$, or, more intuitively, is caused by the same temperature power law of m_T and H.

small η, the latter solution contributes to the nonzero initial velocity, while the former one does not. The $\eta = 1$ case is the critical point in the parameter space which separates the sliding and oscillating phases. In this case, the scalar moves toward the thermal minimum obeying the relation $\delta\phi \propto T^{1/2}$ approximately. When η goes beyond the critical value, i.e., in the case where $\eta > 1$, the scalar's evolution is in the oscillating phase whose amplitude dwindles like $|\delta\phi| \propto T^{1/2}$ as the universe expands. From Eq. (A6), we can find that the front coefficient of the cosine function dominates over the sine function as the result of the initial condition $\dot\phi_{\rm rh} = 0$. Another feature of the oscillating solution for the $\eta > 1$ case worthwhile to be discussed is that the T-dependent part is the log function. Such a log term comes from the imaginary part of T's power, or, in other words, is the feature of the homogeneous linear equation, which takes its form because m_T and H have the same temperature power law.

Those who are curious about comparing the analytical and numerical solutions can refer to Fig. 9, where the solid lines represent the numerical solutions, and the dotted dark lines denote the analytical solutions, as shown in Eq. (A4), Eq. (A5), and Eq. (A6), in the linear approximation. The red, green, and blue colors are related to the $\eta > 1$, $\eta = 1$, and $\eta < 1$ cases, respectively. Since the type-A and the type-B models have similar behaviors when moving toward the thermal minimum in the high-temperature universe, we take the type-A model as an example to draw the plot, and the numerical-analytical comparison for the type-B model can be identically transplanted. In Fig. 9, one can easily see that the analytical solutions listed in Eq. (A4), Eq. (A5), and Eq. (A6) are perfectly consistent with the numerical results.

Appendix B: Dark Photon Freeze-in

As long as the kinetic mixing is nonzero and the amount of the initial dark photon is negligible, the dark photons are always produced in the late universe through the energy transfer from the visible sector, well-known as the freeze-in production. Following the first calculation of the dark photon freeze-in [58, 59], we give a pedagogical introduction in this appendix, which is divided into two parts: $m_{A'} < 2m_e$ and $m_{A'} \gtrsim 2m_e$. When $m_{A'} < 2m_e$, the dark photon
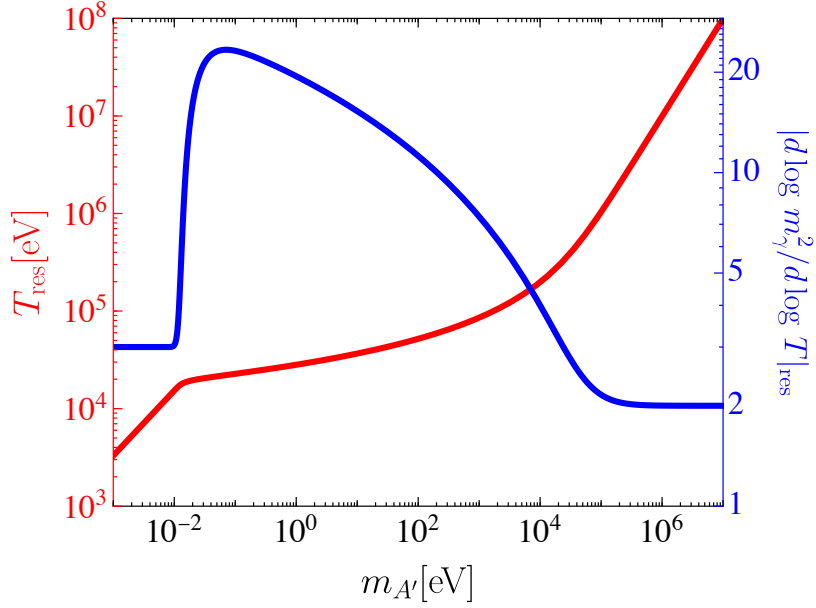
Figure 10. The plot showing how T_{res} and $\left|d\log m_\gamma^2/d\log T\right|_{\mathrm{res}}$ change in terms of $m_{A'}$. Here, T_{res} represented by the red line is the temperature in which the resonant transition $\gamma \to A'$ happens. Its numerical value can be read from the red vertical axis on the left-hand side of the plot. The dimensionless quantity $\left|d\log m_\gamma^2/d\log T\right|_{\mathrm{res}}$ represents how fast the plasmon mass changes in terms of the temperature at which the resonant transition happens. Readers can refer to the blue axis on the right-hand side for its numerical value. In the mass range $m_{A'} \gtrsim 10^5\mathrm{eV}$, $T_{\mathrm{res}} \propto m_{A'}$ and $\left|d\log m_\gamma^2/d\log T\right|_{\mathrm{res}} \simeq 2$ because $m_\gamma^2 \propto T^2$ when electrons are relativistic. When $m_{A'} \lesssim 10^{-2}\mathrm{eV}$, $T_{\mathrm{res}} \propto m_{A'}^{2/3}$ and $\left|d\log m_\gamma^2/d\log T\right|_{\mathrm{res}} \simeq 3$, as a result of the plasmon mass power law $m_\gamma^2 \propto n_{e^-} \propto T^3$ when the symmetric e^-e^+ annihilate away but the asymmetric e^- remains. In the middle mass range where $10^{-2}\mathrm{eV} \lesssim m_{A'} \lesssim 10^5\mathrm{eV}$, the $\gamma \to A'$ resonance happens when the plasmon mass is experiencing the exponential drop as the universe temperature goes below the electron mass. In this case, T_{res} is in the range $10^{-2}m_e - m_e$ and insensitive to the value of $m_{A'}$. The semi-analytical estimations of T_{res} and $\left|d\log m_\gamma^2/d\log T\right|_{\mathrm{res}}$ in such a case can be found in Eq. (B5).

production is dominated by the resonant transition $\gamma \to A'$. When $m_{A'} \gtrsim 2m_e$, the dark photon mainly comes from the inverse decay $e^-e^+ \to A'$.

1. $m_{A'} < 2m_e$

Knowing that the dominant contribution comes from the resonant transition of the transverse photon when $m_{A'} < 2m_e$, we write down the Boltzmann equation

$$\dot{n}_{A'} + 3Hn_{A'} \simeq n_\gamma \langle\Gamma_{\gamma\to A'}\rangle, \quad \text{where} \quad \langle\Gamma_{\gamma\to A'}\rangle \simeq \frac{\pi^3}{12\zeta(3)} \frac{\epsilon^2 m_{A'}^4}{T} \delta(m_\gamma^2 - m_{A'}^2) \tag{B1}$$

is the thermal average of $\gamma \to A'$ transition probability and $n_\gamma = 2\zeta(3)T^3/\pi^2$ is the transverse photon number density. The delta function in $\langle\Gamma_{\gamma\to A'}\rangle$ reveals the feature of the resonant production: Most of the dark photons below the electron mass are produced when $m_{A'}^2 \simeq m_\gamma^2$. Doing the time integration of the Boltzmann equation, we get today's dark photon relic abundance

$$\Omega_{A'} \simeq \left(\frac{3^2 \cdot 5^{3/2}}{2^3 \cdot \pi^{5/2} \cdot g_{*,S}g_*^{1/2}} \frac{\epsilon^2 m_{A'}^3 m_{\mathrm{pl}}s_0}{T^3 \left|d\log m_\gamma^2/d\log T\right|\rho_c}\right)_{\mathrm{res}}, \tag{B2}$$

where "res" means all the temperature-dependent quantities in Eq. (B2) are chosen to be the ones when the plasmon mass and the dark photon mass match with each other. In Eq. (B2), s_0 is today's universe entropy, ρ_c is the critical density, and $\left|d\log m_\gamma^2/d\log T\right|_{\mathrm{res}}$, an order $1-10$ factor, represents how fast m_γ^2 passes through the vicinity of $m_{A'}^2$. The numerical values of T_{res} and $\left|d\log m_\gamma^2/d\log T\right|_{\mathrm{res}}$ are shown in Fig. 10.

For $m_{A'} \gtrsim 10^5$eV, the resonant transition happens when electrons are relativistic. In this time, the plasmon mass is $m_\gamma^2 \simeq e^2 T^2/6$, based on which we have [10]

$$T_{\text{res}} \simeq 8 m_{A'} \quad \text{and} \quad \left| \frac{d \log m_\gamma^2}{d \log T} \right|_{\text{res}} \simeq 2. \tag{B3}$$

In Eq. (B2), $m_{A'}^3$ and T_{res}^3 cancel with each other, so for fixed dark photon relic abundance, ϵ is the constant of $m_{A'}$. If all the dark matter is comprised of the dark photon, the needed kinetic mixing is

$$\epsilon_{\text{FI}} \sim 10^{-12} \left(\frac{\Omega_{A'} h^2}{0.12} \right)^{1/2}. \tag{B4}$$

For 10^{-2}eV $\lesssim m_{A'} \lesssim 10^5$eV, the resonant transition happens when 10keV $\lesssim T \lesssim m_e$. In this epoch, the plasmon mass is $m_\gamma^2 \simeq e^2 n_e / m_e$, where $n_e \simeq g_e (m_e T/2\pi)^{3/2} e^{-m_e/T}$. By solving the resonant condition, we have

$$T_{\text{res}} \sim m_e \left[\log \left(\frac{2^{1/2}}{\pi^{3/2}} \frac{e^2 m_e}{m_{A'}} \right) \right]^{-1} \quad \text{and} \quad \left| \frac{d \log m_\gamma^2}{d \log T} \right|_{\text{res}} \simeq \frac{3}{2} + \frac{m_e}{T_{\text{res}}}. \tag{B5}$$

Since T_{res} is insensitive to $m_{A'}$'s changing, given the dark photon relic abundance, $\epsilon \propto m_{A'}^{-3/2}$. More quantitative representation for the $\epsilon - m_{A'}$ relation is given as

$$\epsilon_{\text{FI}} \sim 10^{-11} \left(\frac{m_{A'}}{1\text{keV}} \right)^{-3/2} \left(\frac{\Omega_{A'} h^2}{0.12} \right)^{1/2}. \tag{B6}$$

For $m_{A'} \lesssim 10^{-2}$eV, $\gamma \to A'$ takes place at the temperature $T \lesssim 10$keV. Since the symmetric $e^- e^+$ annihilates away, the plasmon mass comes from the asymmetric e^- whose number density is conserved. In this case, the plasmon mass is scaled as $m_\gamma \propto n_e \propto T^{3/2}$, and the resonant temperature is scaled as $T_{\text{res}} \propto m_{A'}^{2/3}$. The concrete formulas for T_{res} and $\left| d \log m_\gamma^2 / d \log T \right|_{\text{res}}$ are

$$T_{\text{res}} \simeq 15\text{keV} \times \left(\frac{m_{A'}}{10^{-2}\text{eV}} \right)^{2/3} \quad \text{and} \quad \left| \frac{d \log m_\gamma^2}{d \log T} \right|_{\text{res}} \simeq 3. \tag{B7}$$

Given the dark photon relic abundance, the kinetic mixing is[11]

$$\epsilon_{\text{FI}} \sim 10^{-4} \left(\frac{m_{A'}}{10^{-2}\text{eV}} \right)^{-1/2} \left(\frac{\Omega_{A'} h^2}{0.12} \right)^{1/2}. \tag{B8}$$

2. $m_{A'} \geq 2m_e$

For the heavy dark photon which satisfies $m_{A'} \geq 2m_e$, the inverse decay channel $e^- e^+ \to A'$ opens up and dominates over the $\gamma \to A'$ channel. In such a case, the Boltzmann equation is

$$\dot{n}_{A'} + 3H n_{A'} \simeq n_{e^-} n_{e^+} \langle \sigma_{e^- e^+ \to A'} v \rangle, \tag{B9}$$

where the collision term is

$$n_{e^-} n_{e^+} \langle \sigma_{e^- e^+ \to A'} v \rangle \simeq g_{e^-} g_{e^+} \int \frac{d^3 p_{e^-}}{(2\pi)^3} \frac{d^3 p_{e^+}}{(2\pi)^3} f_{e^-} f_{e^+} \sigma_{e^- e^+ \to A'} v_{\text{Møl}}. \tag{B10}$$

---

[10] Here T_{res} is $T_{\gamma \to A'}$ in Eq. (37). We use the lower index "res" to emphasize the character of the resonance transition for $\gamma \to A'$.

[11] Even though the warm dark matter bounds exclude the 100% dark photon dark matter via freeze-in when $m_{A'} \gtrsim$ few $\times$ 10keV, the subcomponent dark photon dark matter can still be produced. In this case, one can rescale the value of ϵ_{FI} by $\Omega_{A'}^{1/2}$.

Then, after calculating the $e^-e^+ \to A'$ cross section[12]

$$\sigma_{e^-e^+ \to A'} = \pi(\epsilon e)^2 \frac{1 + 2m_e^2/m_{A'}^2}{\sqrt{1 - 4m_e^2/m_{A'}^2}} \delta(s - m_{A'}^2), \tag{B11}$$

substituting it into Eq. (B10), using the Maxwell-Boltzmann distribution to approximate the electron/positron phase space, and doing the phase space integration as shown in [226], we have

$$n_{e^-} n_{e^+} \langle \sigma_{e^-e^+ \to A'} v \rangle \simeq \frac{(\epsilon e)^2}{8\pi^3} m_{A'}^3 T \left(1 + \frac{2m_e^2}{m_{A'}^2}\right) \sqrt{1 - \frac{4m_e^2}{m_{A'}^2}} K_1 \left(\frac{m_{A'}}{T}\right). \tag{B12}$$

Finally, after using the approximation $K_1(m_{A'}/T) \simeq (\pi T/2m_{A'})^{1/2} e^{-m_{A'}/T}$ in the low temperature limit $T \ll m_{A'}$ and solving the Boltzmann equation Eq. (B9), we get the dark photon relic abundance

$$\Omega_{A'} \simeq \frac{3^4 \cdot 5^{5/2}}{2^{17/2} \cdot \pi^{11/2}} \frac{(\epsilon e)^2}{g_{*S} g_*^{1/2}} \frac{m_{\rm pl} s_0}{\rho_c} \left(1 + \frac{2m_e^2}{m_{A'}^2}\right) \sqrt{1 - \frac{4m_e^2}{m_{A'}^2}}. \tag{B13}$$

From Eq. (B13), we know that the ϵ to reach dark matter's relic abundance when $m_{A'} \gtrsim 2m_e$ is nearly the constant of $m_{A'}$, which is similar as Eq. (B4) but a bit smaller.

Appendix C: $\mathbb{Z}_N$-Invariant Coleman-Weinberg Potential

In [102], the authors calculated the 1-loop Coleman-Weinberg potential under the $\mathbb{Z}_N$ symmetry to the leading order, showing that when such symmetry is imposed, there will be an exponential suppression factor r^N in the potential from the quantum correction. To investigate the extra cancellation from the exact $\mathbb{Z}_2$ symmetry, we precisely expand Eq. (59) to all orders. Here, we list the complete form of the 1-loop $\mathbb{Z}_N$ Coleman-Weinberg potential (Here $N > 4$, $\theta := \phi/f + \pi/2$)

$$V_{\rm cw}(\theta) = \frac{M^4 N}{8\pi^2} \sum_{l=1}^{+\infty} \left[\sum_{j=0}^{+\infty} r^{lN+2j} G(lN + 2j) \binom{lN + 2j}{j} + (r \to r') \right] \cos(lN\theta) + {\rm const}, \tag{C1}$$

which is equivalent to Eq. (63). The definition of $G(n)$ can be found in Eq. (65). In this equation, we find that for the term containing $\cos(lN\theta)$, the Fourier coefficient is proportional to r^{lN}, which reveals the exponential suppression in the effective operator $\mathcal{L} \supset {\rm const} \times (\Phi^{lN} + \Phi^{\dagger lN})/\Lambda_l^{lN-4}$. For the type-B model, $r = -r'$, such that the Lagrangian in Eq. (54) is invariant under the dark charge conjugation $\mathcal{C}_d$, i.e., $(A, A', \phi, \Psi) \leftrightarrow (A, -A', -\phi, \Psi')$. If N is an odd number, the $\cos(N\theta)$ terms exactly cancel with each other, but the $\cos(2N\theta)$ terms still exist, so the lowest order effective operators are $\mathcal{L} \supset {\rm const} \times (\Phi^{2N} + \Phi^{\dagger 2N})/\Lambda_2^{2N-4}$. In the rest of this appendix, we derive the equation Eq. (C1) in two different methods: 1. The Fourier transformation. 2. The cosine sum rules.

1. Fourier Transformation

Because the potential Eq. (59) is invariant under the transformations $\theta \to \theta + \frac{2\pi}{N}$ and $\theta \to -\theta$, it can be expanded in terms of the complete basis $\cos(lN\theta)$ ($l = 1, 2, \cdots$) as shown in Eq. (60). After $V_{\rm cw}(\theta)$ are expanded in terms of the r powers, the single-world Fourier coefficient can be written as

$$\widetilde{V}_{\rm cw}(lN) = \frac{M^4}{4\pi^3} \sum_{m=1}^{+\infty} r^m 2^{m-1} G(m) \int_0^\pi d\theta \ \cos(lN\theta) \cos^m \theta + (r \to r'). \tag{C2}$$

---

[12] We correct $\sigma_{e^-e^+ \to A'}$ in [59].

Applying the trigonometric identity

$$\cos(n\theta)\cos^m\theta = \frac{1}{2^m}\sum_{j=0}^{m}\binom{m}{j}\cos\left[(n-m+2j)\theta\right],$$ (C3)

we find that only the terms satisfying $lN = m - 2j$ are picked out. After writing the summation in the Fourier coefficient $\widetilde{V}_{\rm cw}(lN)$ as

$$\sum_{m=1}^{+\infty}\sum_{j=0}^{m}\delta_{m,\,lN+2j} = \sum_{\substack{m=lN+2j \\ j=0,1,\cdots}}$$ (C4)

and plugging $\widetilde{V}_{\rm cw}(lN)$ into Eq. (60), we get the equation Eq. (C1).

2. Cosine Sum Rules

To calculate the Coleman-Weinberg potential in the θ-space directly, we use the cosine sum rules

$$\frac{1}{N}\sum_{k=0}^{N-1}\cos^m\left(\theta+\frac{2\pi k}{N}\right) = \sum_{l=1}^{[m/N]}\mathcal{C}_{lmN}\cos(\theta lN) + \mathcal{D}_m,$$ (C5)

where

$$\begin{cases}\mathcal{C}_{lmN} = \dfrac{1}{2^{m-1}}\dbinom{m}{\frac{m+lN}{2}}\left(\delta_{l\bmod 2,\,0}\,\delta_{m\bmod 2,\,0} + \delta_{l\bmod 2,\,1}\,\delta_{(m+N)\bmod 2,\,0}\right) \\[3mm] \mathcal{D}_m = \dfrac{1}{2^m}\dbinom{m}{m/2}\delta_{m\bmod 2,\,0}\end{cases}.$$ (C6)

The cosine sum rules metioned above can be derived by expanding the cosine functions in terms of the exponential functions and applying the formula $\frac{1}{N}\sum_{k=0}^{N-1}\exp\left(i\frac{2\pi nk}{N}\right) = \delta_{n\bmod N,\,0}$. After plugging Eq. (C5) into

$$V_{\rm cw}(\theta) = \frac{M^4}{8\pi^2}\sum_{m=1}^{+\infty}r^m 2^{m-1}G(m)\sum_{k=0}^{N-1}\cos^m\left(\theta+\frac{2\pi k}{N}\right) + (r\to r'),$$ (C7)

and reshuffling the summation as

$$\begin{cases}\displaystyle\sum_{\substack{m=2j \\ j=0,1,\cdots}}\sum_{l=1}^{[m/N]} = \sum_{l=1}^{+\infty}\sum_{\substack{m=lN+2j, \\ j=0,1,\cdots}} & \text{(Even } N) \\[6mm] \displaystyle\sum_{\substack{m=2j+1 \\ j=0,1,\cdots}}\sum_{\substack{l=1 \\ \text{odd } l}}^{[m/N]} + \sum_{\substack{m=2j \\ j=0,1,\cdots}}\sum_{\substack{l=1 \\ \text{even } l}}^{[m/N]} = \sum_{l=1}^{+\infty}\sum_{\substack{m=lN+2j, \\ j=0,1,\cdots}} & \text{(Odd } N)\end{cases},$$ (C8)

we can also derive the equation Eq. (C1).

[1] L. J. Hall, K. Jedamzik, J. March-Russell, and S. M. West, JHEP **03**, 080 (2010), arXiv:0911.1120 [hep-ph].

[2] B. Holdom, Phys. Lett. B **166**, 196 (1986).

[3] N. Aghanim *et al.* (Planck), Astron. Astrophys. **641**, A6 (2020), [Erratum: Astron.Astrophys. 652, C4 (2021)], arXiv:1807.06209 [astro-ph.CO].

[4] A. Falkowski, J. Juknevich, and J. Shelton, (2009), arXiv:0908.1790 [hep-ph].

[5] M. Lindner, A. Merle, and V. Niro, Phys. Rev. D **82**, 123529 (2010), arXiv:1005.3116 [hep-ph].

[6] V. Gonzalez Macias and J. Wudka, JHEP **07**, 161 (2015), arXiv:1506.03825 [hep-ph].

[7] B. Batell, T. Han, D. McKeen, and B. Shams Es Haghi, Phys. Rev. D **97**, 075016 (2018), arXiv:1709.07001 [hep-ph].

[8] B. Batell, T. Han, and B. Shams Es Haghi, Phys. Rev. D **97**, 095020 (2018), arXiv:1704.08708 [hep-ph].

[9] A. Berlin and N. Blinov, Phys. Rev. D **99**, 095030 (2019), arXiv:1807.04282 [hep-ph].

[10] V. Silveira and A. Zee, Phys. Lett. B **161**, 136 (1985).

[11] J. McDonald, Phys. Rev. D **50**, 3637 (1994), arXiv:hep-ph/0702143.

[12] C. P. Burgess, M. Pospelov, and T. ter Veldhuis, Nucl. Phys. B **619**, 709 (2001), arXiv:hep-ph/0011335.

[13] B. Patt and F. Wilczek, (2006), arXiv:hep-ph/0605188.

[14] M. Fabbrichesi, E. Gabrielli, and G. Lanfranchi, (2020), 10.1007/978-3-030-62519-1, arXiv:2005.01515 [hep-ph].

[15] A. Caputo, A. J. Millar, C. A. J. O'Hare, and E. Vitagliano, Phys. Rev. D **104**, 095029 (2021), arXiv:2105.04565 [hep-ph].

[16] K. R. Dienes, C. F. Kolda, and J. March-Russell, Nucl. Phys. B **492**, 104 (1997), arXiv:hep-ph/9610479.

[17] S. A. Abel and B. W. Schofield, Nucl. Phys. B **685**, 150 (2004), arXiv:hep-th/0311051.

[18] M. Goodsell, J. Jaeckel, J. Redondo, and A. Ringwald, JHEP **11**, 027 (2009), arXiv:0909.0515 [hep-ph].

[19] M. Goodsell, S. Ramos-Sanchez, and A. Ringwald, JHEP **01**, 021 (2012), arXiv:1110.6901 [hep-th].

[20] M. Del Zotto, J. J. Heckman, P. Kumar, A. Malekian, and B. Wecht, Phys. Rev. D **95**, 016007 (2017), arXiv:1608.06635 [hep-ph].

[21] T. Gherghetta, J. Kersten, K. Olive, and M. Pospelov, Phys. Rev. D **100**, 095001 (2019), arXiv:1909.00696 [hep-ph].

[22] K. Benakli, C. Branchina, and G. Lafforgue-Marmet, Eur. Phys. J. C **80**, 1118 (2020), arXiv:2007.02655 [hep-ph].

[23] G. Obied and A. Parikh, (2021), arXiv:2109.07913 [hep-ph].

[24] T. G. Rizzo, JHEP **07**, 118 (2018), arXiv:1801.08525 [hep-ph].

[25] G. N. Wojcik, (2022), arXiv:2205.11545 [hep-ph].

[26] W. H. Chiu, S. Hong, and L.-T. Wang, (2022), arXiv:2209.10563 [hep-ph].

[27] A. Banerjee, G. Bhattacharyya, D. Chowdhury, and Y. Mambrini, JCAP **12**, 009 (2019), arXiv:1905.11407 [hep-ph].

[28] I. Baldes, D. Chowdhury, and M. H. Tytgat, Phys. Rev. D **100**, 095009 (2019), arXiv:1907.06663 [hep-ph].

[29] S. Chakraborty, T. H. Jung, V. Loladze, T. Okui, and K. Tobioka, Phys. Rev. D **102**, 095029 (2020), arXiv:2008.10610 [hep-ph].

[30] H. Davoudiasl and J. Gehrlein, (2022), arXiv:2208.04964 [hep-ph].

[31] J. D. Bekenstein, Phys. Rev. D **25**, 1527 (1982).

[32] K. A. Olive and M. Pospelov, Phys. Rev. D **65**, 085044 (2002), arXiv:hep-ph/0110377.

[33] G. R. Dvali and M. Zaldarriaga, Phys. Rev. Lett. **88**, 091303 (2002), arXiv:hep-ph/0108217.

[34] Z. Chacko, C. Grojean, and M. Perelstein, Phys. Lett. B **565**, 169 (2003), arXiv:hep-ph/0204142.

[35] R. Fardon, A. E. Nelson, and N. Weiner, JCAP **10**, 005 (2004), arXiv:astro-ph/0309800.

[36] R. Fardon, A. E. Nelson, and N. Weiner, JHEP **03**, 042 (2006), arXiv:hep-ph/0507235.

[37] N. Weiner and K. M. Zurek, Phys. Rev. D **74**, 023517 (2006), arXiv:hep-ph/0509201.

[38] A. Ghalsasi, D. McKeen, and A. E. Nelson, Phys. Rev. D **95**, 115039 (2017), arXiv:1609.06326 [hep-ph].

[39] M. J. Baker and J. Kopp, Phys. Rev. Lett. **119**, 061801 (2017), arXiv:1608.07578 [hep-ph].

[40] M. J. Baker, M. Breitbach, J. Kopp, and L. Mittnacht, JHEP **03**, 114 (2018), arXiv:1712.03962 [hep-ph].

[41] M. J. Baker and L. Mittnacht, JHEP **05**, 070 (2019), arXiv:1811.03101 [hep-ph].

[42] L. Bian and Y.-L. Tang, JHEP **12**, 006 (2018), arXiv:1810.03172 [hep-ph].

[43] L. Bian and X. Liu, Phys. Rev. D **99**, 055003 (2019), arXiv:1811.03279 [hep-ph].

[44] D. Croon, G. Elor, R. Houtz, H. Murayama, and G. White, (2020), arXiv:2012.15284 [hep-ph].

[45] K. Hashino, J. Liu, X.-P. Wang, and K.-P. Xie, (2021), arXiv:2109.07479 [hep-ph].

[46] J. Guo, Y. He, J. Liu, X.-P. Wang, and K.-P. Xie, (2022), arXiv:2206.14221 [hep-ph].

[47] I. Baldes, T. Konstandin, and G. Servant, JHEP **12**, 073 (2016), arXiv:1608.03254 [hep-ph].

[48] S. Bruggisser, T. Konstandin, and G. Servant, JCAP **11**, 034 (2017), arXiv:1706.08534 [hep-ph].

[49] S. A. R. Ellis, S. Ipek, and G. White, JHEP **08**, 002 (2019), arXiv:1905.11994 [hep-ph].

[50] J. Berger, A. J. Long, and J. Turner, Phys. Rev. D **100**, 055005 (2019), arXiv:1906.05157 [hep-ph].

[51] S. Ipek and T. M. P. Tait, Phys. Rev. Lett. **122**, 112001 (2019), arXiv:1811.00559 [hep-ph].

[52] D. Croon, J. N. Howard, S. Ipek, and T. M. P. Tait, Phys. Rev. D **101**, 055042 (2020), arXiv:1911.01432 [hep-ph].

[53] D. Berger, S. Ipek, T. M. P. Tait, and M. Waterbury, JHEP **07**, 192 (2020), arXiv:2004.06727 [hep-ph].

[54] J. N. Howard, S. Ipek, T. M. P. Tait, and J. Turner, JHEP **02**, 047 (2022), arXiv:2112.09152 [hep-ph].

[55] L. W. H. Fung, L. Li, T. Liu, H. N. Luu, Y.-C. Qiu, and S. H. H. Tye, JCAP **08**, 057 (2021), arXiv:2102.11257 [hep-ph].

[56] L. W. Fung, L. Li, T. Liu, H. N. Luu, Y.-C. Qiu, and S. H. H. Tye, (2021), arXiv:2105.01631 [astro-ph.CO].

[57] I. J. Allali, M. P. Hertzberg, and Y. Lyu, Phys. Rev. D **105**, 123517 (2022), arXiv:2203.15817 [hep-ph].

[58] M. Pospelov, A. Ritz, and M. B. Voloshin, Phys. Rev. D **78**, 115012 (2008), arXiv:0807.3279 [hep-ph].

[59] J. Redondo and M. Postma, JCAP **02**, 005 (2009), arXiv:0811.0326 [hep-ph].

[60] H. An, M. Pospelov, J. Pradler, and A. Ritz, Phys. Lett. B **747**, 331 (2015), arXiv:1412.8378 [hep-ph].

[61] S. Dodelson and L. M. Widrow, Phys. Rev. Lett. **72**, 17 (1994), arXiv:hep-ph/9303287.

[62] K. N. Abazajian, Phys. Rept. **711-712**, 1 (2017), arXiv:1705.01837 [hep-ph].

[63] M. Escudero, A. Berlin, D. Hooper, and M.-X. Lin, JCAP **12**, 029 (2016), arXiv:1609.09079 [hep-ph].

[64] Y.-S. Wu and Z. Wang, Phys. Rev. Lett. **57**, 1978 (1986).

[65] K.-i. Maeda, Mod. Phys. Lett. A **3**, 243 (1988).

[66] T. Damour, G. W. Gibbons, and C. Gundlach, Phys. Rev. Lett. **64**, 123 (1990).

[67] T. Damour and A. M. Polyakov, Nucl. Phys. B **423**, 532 (1994), arXiv:hep-th/9401069.

[68] T. Damour and A. M. Polyakov, Gen. Rel. Grav. **26**, 1171 (1994), arXiv:gr-qc/9411069.

[69] T. Damour, F. Piazza, and G. Veneziano, Phys. Rev. Lett. **89**, 081601 (2002), arXiv:gr-qc/0204094.

[70] T. Damour, F. Piazza, and G. Veneziano, Phys. Rev. D **66**, 046007 (2002), arXiv:hep-th/0205111.

[71] J. Redondo, JCAP **07**, 008 (2008), arXiv:0801.1527 [hep-ph].

[72] J. Redondo and G. Raffelt, JCAP **08**, 034 (2013), arXiv:1305.2920 [hep-ph].

[73] H. An, M. Pospelov, and J. Pradler, Phys. Lett. B **725**, 190 (2013), arXiv:1302.3884 [hep-ph].

[74] E. Hardy and R. Lasenby, JHEP **02**, 033 (2017), arXiv:1611.05852 [hep-ph].

[75] I. M. Bloch, R. Essig, K. Tobioka, T. Volansky, and T.-T. Yu, JHEP **06**, 087 (2017), arXiv:1608.02123 [hep-ph].

[76] E. Aprile *et al.* (XENON), Phys. Rev. Lett. **121**, 111302 (2018), arXiv:1805.12562 [astro-ph.CO].

[77] K. Abe *et al.* (XMASS), Phys. Lett. B **787**, 153 (2018), arXiv:1807.08516 [astro-ph.CO].

[78] E. Aprile *et al.* (XENON), Phys. Rev. Lett. **123**, 251801 (2019), arXiv:1907.11485 [hep-ex].

[79] E. Aprile *et al.* (XENON), Phys. Rev. D **102**, 072004 (2020), arXiv:2006.09721 [hep-ex].

[80] E. Aprile *et al.* ((XENON Collaboration)††, XENON), Phys. Rev. Lett. **129**, 161805 (2022), arXiv:2207.11330 [hep-ex].

[81] R. Essig, E. Kuflik, S. D. McDermott, T. Volansky, and K. M. Zurek, JHEP **11**, 193 (2013), arXiv:1309.4091 [hep-ph].

[82] T. R. Slatyer and C.-L. Wu, Phys. Rev. D **95**, 023010 (2017), arXiv:1610.06933 [astro-ph.CO].

[83] G. L. Smith, C. D. Hoyle, J. H. Gundlach, E. G. Adelberger, B. R. Heckel, and H. E. Swanson, Phys. Rev. D **61**, 022001 (2000).

[84] S. Schlamminger, K. Y. Choi, T. A. Wagner, J. H. Gundlach, and E. G. Adelberger, Phys. Rev. Lett. **100**, 041101 (2008), arXiv:0712.0607 [gr-qc].

[85] J. Bergé, P. Brax, G. Métris, M. Pernot-Borràs, P. Touboul, and J.-P. Uzan, Phys. Rev. Lett. **120**, 141101 (2018), arXiv:1712.00483 [gr-qc].

[86] A. Arvanitaki, J. Huang, and K. Van Tilburg, Phys. Rev. D **91**, 015015 (2015), arXiv:1405.2925 [hep-ph].

[87] K. Van Tilburg, N. Leefer, L. Bougas, and D. Budker, Phys. Rev. Lett. **115**, 011802 (2015), arXiv:1503.06886 [physics.atom-ph].

[88] A. Hees, J. Guéna, M. Abgrall, S. Bize, and P. Wolf, Phys. Rev. Lett. **117**, 061301 (2016), arXiv:1604.08514 [gr-qc].

[89] G. Barontini *et al.*, (2021), arXiv:2112.10618 [hep-ph].

[90] B. A. C. O. N. B. Collaboration, Nature **591**, 564 (2021).

[91] A. Arvanitaki, S. Dimopoulos, and K. Van Tilburg, Phys. Rev. Lett. **116**, 031102 (2016), arXiv:1508.01798 [hep-ph].

[92] D. E. Kaplan, A. Mitridate, and T. Trickle, (2022), arXiv:2205.06817 [hep-ph].

[93] Y. V. Stadnik and V. V. Flambaum, Phys. Rev. Lett. **115**, 201301 (2015), arXiv:1503.08540 [astro-ph.CO].

[94] L. Hart and J. Chluba, Mon. Not. Roy. Astron. Soc. **493**, 3255 (2020), arXiv:1912.03986 [astro-ph.CO].

[95] S. Sibiryakov, P. Sørensen, and T.-T. Yu, JHEP **12**, 075 (2020), arXiv:2006.04820 [hep-ph].

[96] T. Bouley, P. Sørensen, and T.-T. Yu, (2022), arXiv:2211.09826 [hep-ph].

[97] J. A. Frieman, C. T. Hill, A. Stebbins, and I. Waga, Phys. Rev. Lett. **75**, 2077 (1995), arXiv:astro-ph/9505060.

[98] A. Hook, Phys. Rev. Lett. **120**, 261802 (2018), arXiv:1802.10093 [hep-ph].

[99] A. Hook, JHEP **04**, 048 (2021), arXiv:1902.06758 [hep-ph].

[100] S. Das and A. Hook, JHEP **10**, 071 (2020), arXiv:2006.10767 [hep-ph].

[101] J. A. Dror and J. M. Leedom, Phys. Rev. D **102**, 115030 (2020), arXiv:2008.02279 [hep-ph].

[102] D. Brzeminski, Z. Chacko, A. Dev, and A. Hook, Phys. Rev. D **104**, 075019 (2021), arXiv:2012.02787 [hep-ph].

[103] L. Di Luzio, B. Gavela, P. Quilez, and A. Ringwald, JHEP **05**, 184 (2021), arXiv:2102.00012 [hep-ph].

[104] A. Banerjee, J. Eby, and G. Perez, (2022), arXiv:2210.05690 [hep-ph].

[105] S. Weinberg, Phys. Rev. D **9**, 3357 (1974).

[106] S. Ramazanov, E. Babichev, D. Gorbunov, and A. Vikman, Phys. Rev. D **105**, 063530 (2022), arXiv:2104.13722 [hep-ph].

[107] J. H. Chang, M. O. Olea-Romacho, and E. H. Tanin, Phys. Rev. D **106**, 113003 (2022), arXiv:2210.05680 [hep-ph].

[108] A. Ireland and S. Koren, (2022), arXiv:2211.13212 [hep-ph].

[109] C. P. Burgess, J. P. Conlon, L.-Y. Hung, C. H. Kom, A. Maharana, and F. Quevedo, JHEP **07**, 073 (2008), arXiv:0805.4037 [hep-th].

[110] M. Cicoli, M. Goodsell, J. Jaeckel, and A. Ringwald, JHEP **07**, 114 (2011), arXiv:1103.3705 [hep-th].

[111] J. I. Kapusta and C. Gale, *Finite-temperature field theory: Principles and applications*, Cambridge Monographs on Mathematical Physics (Cambridge University Press, 2011).

[112] S. R. Coleman, Phys. Rev. D **15**, 2929 (1977), [Erratum: Phys.Rev.D 16, 1248 (1977)].

[113] C. G. Callan, Jr. and S. R. Coleman, Phys. Rev. D **16**, 1762 (1977).

[114] A. D. Linde, Nucl. Phys. B **216**, 421 (1983), [Erratum: Nucl.Phys.B 223, 544 (1983)].

[115] K.-M. Lee and E. J. Weinberg, Nucl. Phys. B **267**, 181 (1986).

[116] M. J. Duncan and L. G. Jensen, Phys. Lett. B **291**, 109 (1992).

[117] K. A. Intriligator, N. Seiberg, and D. Shih, JHEP **04**, 021 (2006), arXiv:hep-th/0602239.

[118] G. Pastras, JHEP **08**, 075 (2013), arXiv:1102.4567 [hep-th].

[119] J. Preskill, M. B. Wise, and F. Wilczek, Phys. Lett. B **120**, 127 (1983).

[120] P. Arias, D. Cadamuro, M. Goodsell, J. Jaeckel, J. Redondo, and A. Ringwald, JCAP **06**, 013 (2012), arXiv:1201.5902 [hep-ph].

[121] V. Iršič, M. Viel, M. G. Haehnelt, J. S. Bolton, and G. D. Becker, Phys. Rev. Lett. **119**, 031302 (2017), arXiv:1703.04683 [astro-ph.CO].

[122] T. Kobayashi, R. Murgia, A. De Simone, V. Iršič, and M. Viel, Phys. Rev. D **96**, 123514 (2017), arXiv:1708.00015 [astro-ph.CO].

[123] E. Armengaud, N. Palanque-Delabrouille, C. Yèche, D. J. E. Marsh, and J. Baur, Mon. Not. Roy. Astron. Soc. **471**, 4606 (2017), arXiv:1703.09126 [astro-ph.CO].

[124] J. Zhang, J.-L. Kuo, H. Liu, Y.-L. S. Tsai, K. Cheung, and M.-C. Chu, Astrophys. J. **863**, 73 (2018), arXiv:1708.04389 [astro-ph.CO].

[125] M. Nori, R. Murgia, V. Iršič, M. Baldi, and M. Viel, Mon. Not. Roy. Astron. Soc. **482**, 3227 (2019), arXiv:1809.09619 [astro-ph.CO].

[126] K. K. Rogers and H. V. Peiris, Phys. Rev. Lett. **126**, 071302 (2021), arXiv:2007.12705 [astro-ph.CO].

[127] R. Hlozek, D. Grin, D. J. E. Marsh, and P. G. Ferreira, Phys. Rev. D **91**, 103512 (2015), arXiv:1410.2896 [astro-ph.CO].

[128] A. Laguë, J. R. Bond, R. Hložek, K. K. Rogers, D. J. E. Marsh, and D. Grin, JCAP **01**, 049 (2022), arXiv:2104.07802 [astro-ph.CO].

[129] T. Bernal, L. M. Fernández-Hernández, T. Matos, and M. A. Rodríguez-Meza, Mon. Not. Roy. Astron. Soc. **475**, 1447 (2018), arXiv:1701.00912 [astro-ph.GA].

[130] V. H. Robles, J. S. Bullock, and M. Boylan-Kolchin, Mon. Not. Roy. Astron. Soc. **483**, 289 (2019), arXiv:1807.06018 [astro-ph.CO].

[131] N. Bar, D. Blas, K. Blum, and S. Sibiryakov, Phys. Rev. D **98**, 083027 (2018), arXiv:1805.00122 [astro-ph.CO].

[132] N. Bar, K. Blum, J. Eby, and R. Sato, Phys. Rev. D **99**, 103020 (2019), arXiv:1903.03402 [astro-ph.CO].

[133] N. Bar, K. Blum, and C. Sun, (2021), arXiv:2111.03070 [hep-ph].

[134] N. Dalal and A. Kravtsov, Phys. Rev. D **106**, 063517 (2022), arXiv:2203.05750 [astro-ph.CO].

[135] B. Batell and A. Ghalsasi, (2021), arXiv:2109.04476 [hep-ph].

[136] B. Batell, A. Ghalsasi, and M. Rai, (2022), arXiv:2211.09132 [hep-ph].

[137] R. T. Co, E. Gonzalez, and K. Harigaya, JHEP **05**, 163 (2019), arXiv:1812.11192 [hep-ph].

[138] F. Takahashi and W. Yin, JHEP **10**, 120 (2019), arXiv:1908.06071 [hep-ph].

[139] J. Huang, A. Madden, D. Racco, and M. Reig, JHEP **10**, 143 (2020), arXiv:2006.07379 [hep-ph].

[140] S. Nakagawa, F. Takahashi, and M. Yamada, JCAP **05**, 062 (2021), arXiv:2012.13592 [hep-ph].

[141] L. Di Luzio, B. Gavela, P. Quilez, and A. Ringwald, JCAP **10**, 001 (2021), arXiv:2102.01082 [hep-ph].

[142] A. E. Nelson and J. Scholtz, Phys. Rev. D **84**, 103501 (2011), arXiv:1105.2812 [hep-ph].

[143] G. Alonso-Álvarez, T. Hugle, and J. Jaeckel, JCAP **02**, 014 (2020), arXiv:1905.09836 [hep-ph].

[144] K. Nakayama, JCAP **10**, 019 (2019), arXiv:1907.06243 [hep-ph].

[145] P. W. Graham, J. Mardon, and S. Rajendran, Phys. Rev. D **93**, 103520 (2016), arXiv:1504.02102 [hep-ph].

[146] Y. Ema, K. Nakayama, and Y. Tang, JHEP **07**, 060 (2019), arXiv:1903.10973 [hep-ph].

[147] A. Ahmed, B. Grzadkowski, and A. Socha, JHEP **08**, 059 (2020), arXiv:2005.01766 [hep-ph].

[148] E. W. Kolb and A. J. Long, JHEP **03**, 283 (2021), arXiv:2009.03828 [astro-ph.CO].

[149] Q.-Y. Wang, Y. Tang, and Y.-L. Wu, Phys. Rev. D **106**, 023502 (2022), arXiv:2203.15452 [hep-ph].

[150] M. Redi and A. Tesi, JHEP **10**, 167 (2022), arXiv:2204.14274 [hep-ph].

[151] A. J. Long and L.-T. Wang, Phys. Rev. D **99**, 063529 (2019), arXiv:1901.03312 [hep-ph].

[152] N. Kitajima and K. Nakayama, (2022), arXiv:2212.13573 [hep-ph].

[153] P. Agrawal, N. Kitajima, M. Reece, T. Sekiguchi, and F. Takahashi, Phys. Lett. B **801**, 135136 (2020), arXiv:1810.07188 [hep-ph].

[154] J. A. Dror, K. Harigaya, and V. Narayan, Phys. Rev. D **99**, 035036 (2019), arXiv:1810.07195 [hep-ph].

[155] R. T. Co, A. Pierce, Z. Zhang, and Y. Zhao, Phys. Rev. D **99**, 075002 (2019), arXiv:1810.07196 [hep-ph].

[156] M. Bastero-Gil, J. Santiago, L. Ubaldi, and R. Vega-Morales, JCAP **04**, 015 (2019), arXiv:1810.07208 [hep-ph].

[157] R. T. Co, K. Harigaya, and A. Pierce, JHEP **12**, 099 (2021), arXiv:2104.02077 [hep-ph].

[158] A. Arvanitaki, M. Baryakhtar, and X. Huang, Phys. Rev. D **91**, 084011 (2015), arXiv:1411.2263 [hep-ph].

[159] M. J. Stott and D. J. E. Marsh, Phys. Rev. D **98**, 083006 (2018), arXiv:1805.02016 [hep-ph].

[160] H. Davoudiasl and P. B. Denton, Phys. Rev. Lett. **123**, 021102 (2019), arXiv:1904.09242 [astro-ph.CO].

[161] C. Ünal, F. Pacucci, and A. Loeb, JCAP **05**, 007 (2021), arXiv:2012.12790 [hep-ph].

[162] A. Hees, O. Minazzoli, E. Savalle, Y. V. Stadnik, and P. Wolf, Phys. Rev. D **98**, 064051 (2018), arXiv:1807.04512 [gr-qc].

[163] A. Banerjee, G. Perez, M. Safronova, I. Savoray, and A. Shalit, (2022), arXiv:2211.05174 [hep-ph].

[164] L. Baggio et al., Phys. Rev. Lett. **94**, 241101 (2005), arXiv:gr-qc/0502101.

[165] L. Badurina et al., JCAP **05**, 011 (2020), arXiv:1911.11755 [astro-ph.CO].

[166] M. Abe et al. (MAGIS-100), Quantum Sci. Technol. **6**, 044003 (2021), arXiv:2104.02835 [physics.atom-ph].

[167] Y.-D. Tsai, J. Eby, and M. S. Safronova, (2021), arXiv:2112.07674 [hep-ph].

[168] Y. A. El-Neaj et al. (AEDGE), EPJ Quant. Technol. **7**, 6 (2020), arXiv:1908.00802 [gr-qc].

[169] D. Brzeminski, Z. Chacko, A. Dev, I. Flood, and A. Hook, Phys. Rev. D **106**, 095031 (2022), arXiv:2207.14310 [hep-ph].

[170] L. Hamaide, H. Müller, and D. J. E. Marsh, Phys. Rev. D **106**, 123509 (2022), arXiv:2210.03705 [astro-ph.CO].

[171] D. S. Akerib et al. (LZ), Phys. Rev. D **104**, 092009 (2021), arXiv:2102.11740 [hep-ex].

[172] S. D. McDermott, H. H. Patel, and H. Ramani, Phys. Rev. D **97**, 073005 (2018), arXiv:1705.00619 [hep-ph].

[173] H. Liu, W. Qin, G. W. Ridgway, and T. R. Slatyer, Phys. Rev. D **104**, 043514 (2021), arXiv:2008.01084 [astro-ph.CO].

[174] L. Forestell, D. E. Morrissey, and G. White, JHEP **01**, 074 (2019), arXiv:1809.01179 [hep-ph].

[175] C. S. Fong, M. H. Rahat, and S. Saad, JHEP **11**, 067 (2022), arXiv:2206.02802 [hep-ph].

[176] C. E. Aalseth et al. (DarkSide-20k), Eur. Phys. J. Plus **133**, 131 (2018), arXiv:1707.08145 [physics.ins-det].

[177] J. Aalbers et al. (DARWIN), JCAP **11**, 017 (2016), arXiv:1606.07001 [astro-ph.IM].

[178] R. Lasenby and K. Van Tilburg, Phys. Rev. D **104**, 023020 (2021), arXiv:2008.08594 [hep-ph].

[179] L. D. Landau, Dokl. Akad. Nauk SSSR **60**, 207 (1948).

[180] C.-N. Yang, Phys. Rev. **77**, 242 (1950).

[181] V. Iršič et al., Phys. Rev. D **96**, 023522 (2017), arXiv:1702.01764 [astro-ph.CO].

[182] C. Dvorkin, T. Lin, and K. Schutz, Phys. Rev. Lett. **127**, 111301 (2021), arXiv:2011.08186 [astro-ph.CO].

[183] F. D'Eramo and A. Lenoci, JCAP **10**, 045 (2021), arXiv:2012.01446 [hep-ph].

[184] I. A. Zelko, T. Treu, K. N. Abazajian, D. Gilman, A. J. Benson, S. Birrer, A. M. Nierenberg, and A. Kusenko, (2022), arXiv:2205.09777 [hep-ph].

[185] T. Kalaydzhyan and N. Yu, Phys. Rev. D **96**, 075007 (2017), arXiv:1705.05833 [hep-ph].

[186] A. Arvanitaki, P. W. Graham, J. M. Hogan, S. Rajendran, and K. Van Tilburg, Phys. Rev. D **97**, 075020 (2018), arXiv:1606.04541 [hep-ph].

[187] P. Du, D. Egana-Ugrinovic, R. Essig, G. Fragione, and R. Perna, Nature Commun. **13**, 4626 (2022), arXiv:2202.01215 [hep-ph].

[188] M. Baryakhtar, M. Galanis, R. Lasenby, and O. Simon, Phys. Rev. D **103**, 095019 (2021), arXiv:2011.11646 [hep-ph].

[189] I. S. Gradshteyn and I. M. Ryzhik, Table of integrals, series, and products (Academic press, 2014).

[190] P. J. Fox, A. E. Nelson, and N. Weiner, JHEP **08**, 035 (2002), arXiv:hep-ph/0206096.

[191] D. S. M. Alves, J. Galloway, M. McCullough, and N. Weiner, Phys. Rev. Lett. **115**, 161801 (2015), arXiv:1502.03819 [hep-ph].

[192] J. Polchinski and L. Susskind, Phys. Rev. D **26**, 3661 (1982).

[193] J. Abdallah et al. (DELPHI), Eur. Phys. J. C **31**, 421 (2003), arXiv:hep-ex/0311019.

[194] G. Aad et al. (ATLAS), Phys. Rev. D **104**, 112010 (2021), arXiv:2108.07586 [hep-ex].

[195] A. M. Sirunyan et al. (CMS), JHEP **04**, 123 (2021), arXiv:2012.08600 [hep-ex].

[196] G. Aad et al. (ATLAS), JHEP **02**, 143 (2021), arXiv:2010.14293 [hep-ex].

[197] K. Kaneta, H.-S. Lee, and S. Yun, Phys. Rev. Lett. **118**, 101802 (2017), arXiv:1611.01466 [hep-ph].

[198] K. Kaneta, H.-S. Lee, and S. Yun, Phys. Rev. D **95**, 115032 (2017), arXiv:1704.07542 [hep-ph].

[199] K. Choi, S. Lee, H. Seong, and S. Yun, Phys. Rev. D **101**, 043007 (2020), arXiv:1806.09508 [hep-ph].

[200] K. Choi, H. Seong, and S. Yun, Phys. Rev. D **102**, 075024 (2020), arXiv:1911.00532 [hep-ph].

[201] A. Hook, G. Marques-Tavares, and Y. Tsai, Phys. Rev. Lett. **124**, 211801 (2020), arXiv:1912.08817 [hep-ph].

[202] A. Hook, G. Marques-Tavares, and C. Ristow, JHEP **06**, 167 (2021), arXiv:2105.06476 [hep-ph].

[203] P. Arias, A. Arza, J. Jaeckel, and D. Vargas-Arancibia, JCAP **05**, 070 (2021), arXiv:2007.12585 [hep-ph].

[204] P. Deniverville, H.-S. Lee, and Y.-M. Lee, Phys. Rev. D **103**, 075006 (2021), arXiv:2011.03276 [hep-ph].

[205] S.-F. Ge, X.-D. Ma, and P. Pasquini, Eur. Phys. J. C **81**, 787 (2021), arXiv:2104.03276 [hep-ph].

[206] V. Domcke, K. Schmitz, and T. You, JHEP **07**, 126 (2022), arXiv:2108.11295 [hep-ph].

[207] J. C. Gutiérrez, B. J. Kavanagh, N. Castelló-Mor, F. J. Casas, J. M. Diego, E. Martínez-González, and R. V. Cortabitarte, (2021), arXiv:2112.11387 [hep-ph].

[208] N. Arkani-Hamed, D. P. Finkbeiner, T. R. Slatyer, and N. Weiner, Phys. Rev. D **79**, 015014 (2009), arXiv:0810.0713 [hep-ph].

[209] N. Arkani-Hamed and N. Weiner, JHEP **12**, 104 (2008), arXiv:0810.0714 [hep-ph].

[210] F. Chen, J. M. Cline, and A. R. Frey, Phys. Rev. D **80**, 083516 (2009), arXiv:0907.4746 [hep-ph].

[211] G. Barello, S. Chang, and C. A. Newby, Phys. Rev. D **94**, 055018 (2016), arXiv:1511.02865 [hep-ph].

[212] C. A. Argüelles, X.-G. He, G. Ovanesyan, T. Peng, and M. J. Ramsey-Musolf, Phys. Lett. B **770**, 101 (2017), arXiv:1604.00044 [hep-ph].

[213] K. Fuyuto, X.-G. He, G. Li, and M. Ramsey-Musolf, Phys. Rev. D **101**, 075016 (2020), arXiv:1902.10340 [hep-ph].

[214] G. Aad *et al.* (ATLAS), JHEP **01**, 172 (2016), arXiv:1508.07869 [hep-ex].

[215] V. Khachatryan *et al.* (CMS), JHEP **02**, 135 (2017), arXiv:1610.09218 [hep-ex].

[216] J. A. Casas, D. G. Cerdeño, J. M. Moreno, and J. Quilis, JHEP **05**, 036 (2017), arXiv:1701.08134 [hep-ph].

[217] E. Hardy, JHEP **06**, 043 (2018), arXiv:1804.06783 [hep-ph].

[218] D. Curtin and S. Gryba, JHEP **08**, 009 (2021), arXiv:2101.11019 [hep-ph].

[219] F. Piazza and M. Pospelov, Phys. Rev. D **82**, 043533 (2010), arXiv:1003.2313 [hep-ph].

[220] P. W. Graham, D. E. Kaplan, J. Mardon, S. Rajendran, and W. A. Terrano, Phys. Rev. D **93**, 075029 (2016), arXiv:1512.06165 [hep-ph].

[221] M. S. Madhavacheril, N. Sehgal, and T. R. Slatyer, Phys. Rev. D **89**, 103508 (2014), arXiv:1310.3815 [astro-ph.CO].

[222] W. L. K. Wu, J. Errard, C. Dvorkin, C. L. Kuo, A. T. Lee, P. McDonald, A. Slosar, and O. Zahn, Astrophys. J. **788**, 138 (2014), arXiv:1402.4108 [astro-ph.CO].

[223] D. Green, P. D. Meerburg, and J. Meyers, JCAP **04**, 025 (2019), arXiv:1804.01055 [astro-ph.CO].

[224] K. Abazajian *et al.*, (2019), arXiv:1907.04473 [astro-ph.IM].

[225] C. Dvorkin *et al.*, in *2022 Snowmass Summer Study* (2022) arXiv:2203.07064 [hep-ph].

[226] P. Gondolo and G. Gelmini, Nucl. Phys. B **360**, 145 (1991).